NANYANG
TECHNOLOGICAL
UNIVERSITY
SINGAPORE

SINGLE CRYSTALS OF ORGANOMETAL TRIHALIDE PEROVSKITE: SYNTHESIS AND OPTOELECTRONIC PROPERTIES

NGUYEN HUY TIEP

INTERDISCIPLINARY GRADUATE SCHOOL
ENERGY RESEARCH INSTITUTE @ NTU (ERI@N)

2018

To my father!

SINGLE CRYSTALS OF ORGANOMETAL TRIHALIDE PEROVSKITE: SYNTHESIS AND OPTOELECTRONIC PROPERTIES

NGUYEN HUY TIEP

Interdisciplinary Graduate School
Energy Research Institute @ NTU (ERI@N)

A thesis submitted to the Nanyang Technological University in
partial fulfilment of the requirement for the degree of
Doctor of Philosophy

2018

Statement of Originality

I hereby certify that the work embodied in this thesis is the result of original research and has not been submitted for a higher degree to any other University or Institution.

. . . .

Date   Student Name

Abstract

Over the last ten years, organic lead trihalide perovskites ($CH_3NH_3PbX_3$, X=Cl, Br, I) have demonstrated to be the most potential material in electronic and photonic applications due to its unique properties including high absorption coefficient,[1] *low intrinsic recombination rates,*[2] *ambipolar transportation,*[3] *and long carrier diffusion lengths.*[4] *Perovskite materials have been intensively studied for numerous applications such as solar cells,*[5-13] *photodetectors.*[14-16] *light-emitting diodes,*[17,18] *and lasing,*[19,20] *In the photovoltaic cell viewpoint, since the first perovskite solar cell (PSC) report in 2009 with a power conversion efficiency (PCE) of 3.8% only,*[21] *the best PSC has recently achieved a surprisingly efficiency up to 23%,*[13] *which fulfilled the commercial standard for the outside solar cell. However, the major drawback of perovskite materials is the moisture instability which limited them for being launched to the commercial market. In that critical situation, the single crystal has promised to enable the perovskite solar cells to break through their limitations. More and more reports have shown that the perovskite single crystal helped to suppress the charge recombination and prevent the bulk defect density, leading to higher PCE and longer stability.*[22-25] *The changing of alkylammonium chains from the CH_3NH_3 to hydrophobic longer chains such as $C_6H_5C_2H_4NH_3$ has been demonstrated to enhance the stability of perovskites.*[26] *Beside the instability issue, the environmental concern about the lead content has been a consideration. However, unlike traditional PSCs based on spin coating or dip coating polycrystal thin films, the single crystal one has been difficult to synthesize due to the lack of the* *sufficient growth crystallization methods. This thesis shows the results for single crystals growth of large centimeter scaled 3D* $CH_3NH_3PbX_3$*, and 2D layered* $(C_6H_5C_2H_4NH_3)_2MX_3$ *(X = I, Br, Cl; M = Pb, Cu) perovskite single crystals by solution crystallization methods. Their crystalline, electronic, optical, phase transition and magnetic properties have been also introduced. The results should be useful for investigation of novel applications based on the stable and high-performance perovskite single crystals.*

Acknowledgements

First and foremost, I would like to thank my supervisor, Professor Fan Hongjin, for his patient guidance and encouragement during my PhD at NTU.

I also would like to give thanks to Professor Lydia Helena Wong and Professor Liu Bin, who have also given me valuable comments and advices in this project.

I also extend my thanks to my group colleagues from the FAN lab SPMS and ERIAN lab mates for their great collaborations and useful critics.

I wish to thank Ms Huang Minying, an ERIAN officer, and Ms Ellen Heng Yuxuan, an IGS officer, for their kindly helps and assistances.

I also would like to thank the Energy Research Institute at NTU (ERI@N), the Singapore-Berkeley Research Initiative for Sustainable Energy (SinBeRISE), and the Interdisciplinary Graduate School (IGS) for the support on finance and facilities of my PhD project.

Last but definitely not least, I would like to thank my family, Ms Dam Thanh Thuong and my friends, who have encouraged me to pursue my PhD program in NTU. Especially, I would like to give my heartfelt thanks to my father, “in my dreams, you are still alive”.

Table of Contents

Chapter 1

Chapter 2

Chapter 3

Chapter 4

Chapter 5

Chapter 6

Chapter 7

Chapter X

Table Captions

Figure Captions

Abbreviations

2D	Two Dimensional
3D	Three Dimensional
CAN	Acetonitrile
AFM	Atomic Force Microscope
ALD	Atomic Layer Deposition
AVC	Antisolvent-vapor assisted crystallization
CB	Conduction Band
$CH_3NH_3PbX_3$ (X = I, Cl, Br)	Lead Halide Perovskite
DI water	Deionized water
DMF	Dimethylformamide
DMSO	Dimethyl sulfoxide
DSSC	Dye-sensitized solar cell
FTO	Fluorine-doped tin oxide
GBL	Gamma Butyrolactone
HTM	Hole Transport Material
ITO	Indium-doped Tin Oxide
LED	Light Emitting Diode
LiTFSI	Lithium bis(trifluoroethane sulfonyl) imide salt
MA	Methylammonium
PCE	Photon to Current Conversion Efficiency
PEA	Phenethyl Ammonium
PEC	Photoelectrochemical
PECC	Phenethyl Ammonium Copper Chloride
PEPC	Phenethyl Ammonium Lead Chloride
PFM	Piezo Force Microscope
PL	Photoluminescence
PMMA	Poly(methyl methacrylate)

PSC	Perovskite Solar Cell
PTAA	Poly(triarylamine)
SEM	Scanning Electron Microscopy
Spiro-OMeTAD	2,2′,7,7′-tetrakis(N,N-p-dimethoxy-phenylamino)-9,9′-spirobi-fluorene
SWNTs	Single Wall carbon Nanotubes
TPB	N,N,N’,N’-tetraphenyl-benzidine
UV	Ultra Violet
ν	Photon frequency (in Hz)
VB	Valence Band
XRD	X-Ray Diffraction

List of Publications

Journals:

1. **Nguyen Huy Tiep**, Zhiliang Ku, Hong Jin Fan*, Recent Advances in improving the stability of perovskite solar cells, Adv. Energy Mater. 6, 1501420 (2016).
2. Zhiliang Ku, **Nguyen Huy Tiep**, Bo Wu, Tze Chien Sum, Denis Fichou, and Hong Jin Fan*, Solvent engineering for fast growth of centimetric high-quality CH3NH3PbI3 perovskite single crystal, New J. Chem. 40, 7261-7264 (2016).
3. Bo Wu, **Huy Tiep Nguyen**, Zhiliang Ku, Guifang Han, David Giovanni, Nripan Mathews, Hong Jin Fan, and Tze Chien Sum*, Discerning the Surface and Bulk Recombination Kinetics of Organic-Inorganic Halide Perovskite Single Crystals, Adv. Energy Mater. 6, 1600551 (2016).
4. Zhiliang Ku, Xinhui Xia, He Shen, **Nguyen Huy Tiep**, Hong Jin Fan*, Mesoporous nickel counter electrode for printable and reusable perovskite solar cells, Nanoscale 7, 13363-13368 (2015).
5. Dongliang Chao, Changrong Zhu, Ming Song, Pei Liang*, Xiao Zhang, **Nguyen Huy Tiep**, Haofei Zhao, John Wang, Rongming Wang, Hua Zhang and Hong Jin Fan*, High-Rate and Stable Quasi-Solid-State Zinc-Ion Battery with Novel 2D Layered Zinc Orthovanadate Array, Adv. Mater. 30, 1803181 (2018).
6. Guichong Jia, Dongliang Chao*, **Nguyen Huy Tiep**, Zheng Zhang, and Hong Jin Fan*, Intercalation Na-Ion Storage in Two-Dimensional $MoS_{2-x}Se_x$ and Capacity Enhancement by Selenium Substitution, Energy Storage Mater. 14,136-142 (2018).
7. Changrong Zhu, An-Liang Wang, Wen Xiao, Dongliang Chao, Xiao Zhang, **Nguyen Huy Tiep**, Shi Chen, Jiani Kang, Xin Wang, Jun Ding, John Wang, Hua Zhang*, and Hong Jin Fan*, In-situ Grown Epitaxial Heterojunction

Exhibits High-Performance Electro-catalytic Water Splitting, Adv. Mater. 30, 1705516 (2018).

8. Guichong Jia, Huanwen Wang, Dongliang Chao, Haiyong He, **Nguyen Huy Tiep**, Yongqi Zhang, Zheng Zhang, Hong Jin Fan*, Ultrathin MoSe2 @N-doped Carbon Composite Nanospheres for Stable Na-Ion Storage , Nanotechnology 28, 42LT01 (2017).
9. Yongqi Zhang, Xinhui Xia, Xun Cao, Bowei Zhang, **Nguyen Huy Tiep**, Haiyong He, Shi Chen, Yizhong Huang, and Hong Jin Fan*, Ultrafine Metal Nanoparticles/N-doped Porous Carbon Hybrids Coated on Carbon Fibers as Flexible and Binder-Free Water Splitting Catalysts, Adv. Energy Mater. 7, 1700220 (2017).
10. Nguyen Thi Minh Hong, Nguyen Ba Doan**, Nguyen Huy Tiep**, Le Viet Cuong, Bui Nguyen Quoc Trinh, Pham Duc Thang, Dong-Hyun Kim, Switchable voltage control of the magnetic anisotropy in heterostructured nanocomposites of CoFe/NiFe/PZT, Journal of the Korean Physical Society 63, 3 (2013).
11. Nguyen Thi Minh Hong, Pham Duc Thang, **Nguyen Huy Tiep**, Le Viet Cuong and Nguyen Huu Duc, *Voltage-controllable magnetic behavior in PZT/NiFe/CoFe nanocomposites*, Adv. Nat. Sci.: Nanosci. Nanotechnol. 2, 015015 (2011).

Conference Proceedings:

1. The 9th International Conference on Materials for Advanced Technologies, 18 – 23 June 2017, Suntec Singapore.

2. The 9th Singapore International Chemistry Conference, 11 – 14 December 2016, NUS U-Town Singapore, **won a Best Poster Award**.

Chapter 1

Introduction

The ultrafast rise of perovskite solar cells has been inspired from the advancement of Park which was published in 2012. In this work, Park introduced a new mesoporous solar cell using lead halide perovskite ($CH_3NH_3PbI_3$) deposited onto a 600 nm thick mesoporous anatase TiO_2 layer.[27] Particularly, a material, namely spiro-OMeTAD, was employed as a hole-transport-material (HTM) to infiltrate the TiO_2/perovskite pores. Under AM 1.5 light exposure, the cell obtained a power conversion efficiency (PCE) of 9.7% with an open circuit voltage, V_{OC}, of about 0.9V. According to the paper, the charge collection from absorbed photons happened in the excited perovskite nanoparticles. Then, the holes injected from perovskite to the HTM spiro-OMeTAD, following by the electron transfer to the mesoporous TiO_2 layer. The HTM usage also helped to enhance the stability of the cell in comparing with $CH_3NH_3PbI_3$-sensitized liquid junction cells.

The above structure has been considered as a traditional design counter of a perovskite solar cell. Over last ten years, organic lead trihalide perovskites ($CH_3NH_3PbX_3$, X=Cl, Br, I) have demonstrated to be the most potential material in electronic and photonic applications with nonstop rising efficiencies. The PCE improvements have been the results of replacing the elements of the traditional perovskite cell. Figure 1.1 shows the up-to-date progress in Research Cell Efficiency Records of hybrid lead halide perovskite solar cells.

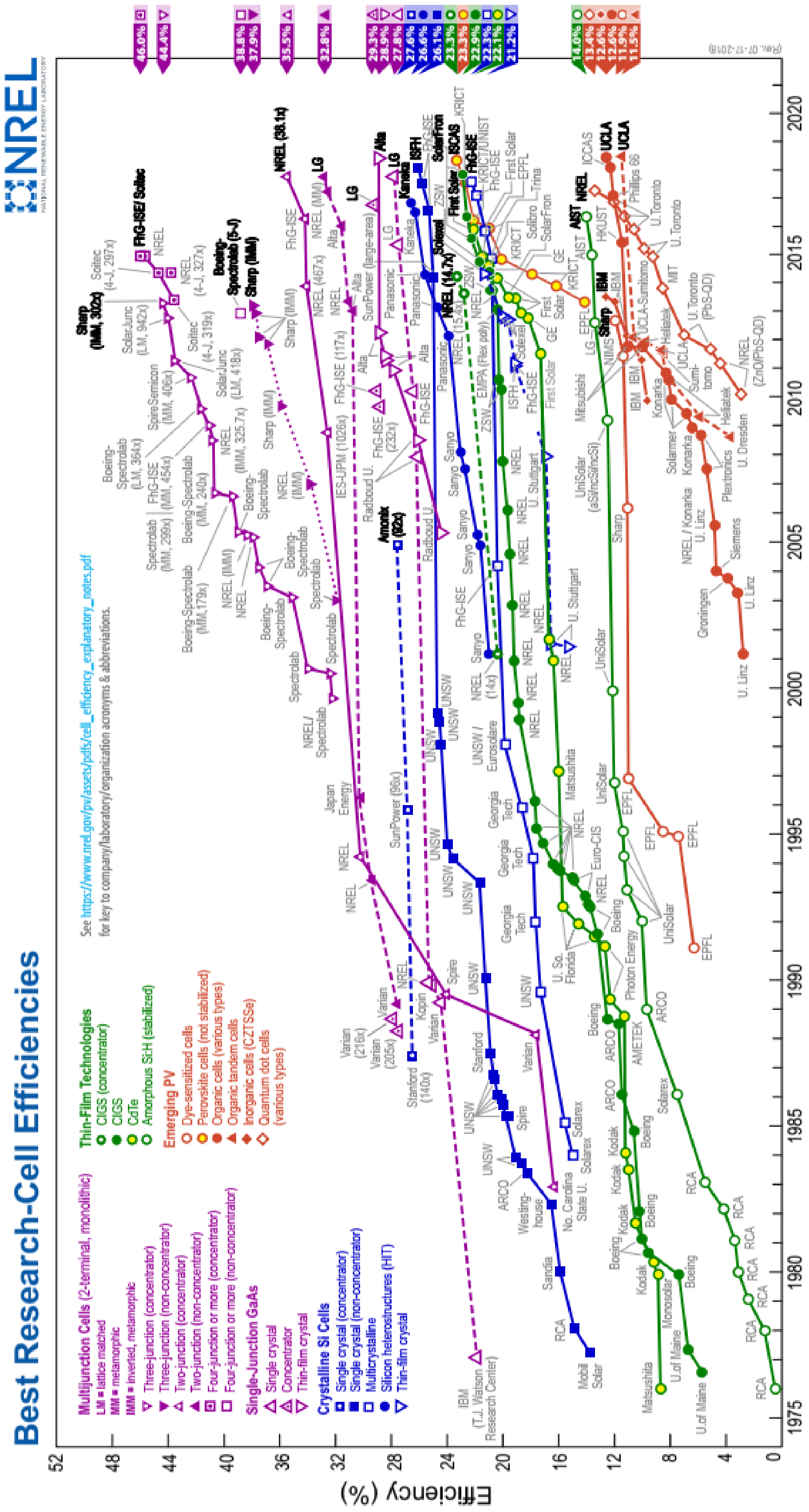

Figure 1.1 Research Cell Efficiency Records adopted from National Renewable Energy Laboratory (NREL) on August 2018.

1.1 Background and Motivation

Beyond the outstanding light-harvesting as well as conversion abilities, perovskite such as $CH_3NH_3PbI_2Cl$ is likely to play the roles in both hole and electron transportations. A related charge separation was found out for the Al_2O_3/perovskite/spiro-OMeTAD device developed by Henry Snaith[28] and his group in 2013. In Snaith's work, the mesoscopic TiO_2 layer was replaced by an insulating layer of Al_2O_3, which acted as a scaffold layer or supporting material for the perovskite $CH_3NH_3PbI_2Cl$. The cell achieved the efficiency of 10.9%. The electrons could not be injected into the insulating Al_2O_3 layer. Consequently, the perovskite $CH_3NH_3PbI_2Cl$ played the roles of a light-harvester as well as an electron-transporter. In the case of perovskite cells without using the hole transport layer spiro-OMeTAD, $CH_3NH_3PbI_3$ is likely to act as the HTM material.

In 2013, Sang Il Seok and his co-workers at Korean Research Institute of Chemical Technology (KRICT) found that the cell's open-circuit voltage can be optimized by swapping the HTM from using spiro-OMeTAD to a polytriarylamine (PTAA)[29]. The perovskite was also adjusted the halide ratio in mixed $CH_3NH_3Pb(I_{1-x}Br_x)_3$ perovskite nanocrystals. In doing so, they delivered 12.3% efficiency, a record for perovskite cells at that time.

Just one month later, Michael Gratzel and his collaborators set an impressive new record of perovskite solar cell. In Gratzel 's paper, the TiO_2 mesoporous layer was filled with a pure perovskite by the sequential deposition. By increasing the loading of the absorber on the TiO_2 structure, they achieved a PCE of 15%.[30]

However, the highest certified efficiency for perovskite solar cell achievements is still popping up. In 2014, the team of Sang Il Seok raised the efficiency of perovskite solar cells to 16.2%, and then 17.9%[31,32]. These impressive advancements were possible thanks to the use of a planar thin-film layer into the mesoscopic devices. In this paper, polytriarylamine was employed as the hole transport material replacing the spiro-OMeTAD. The critical point should be the use of a highly uniform perovskite active upper layer with the thickness of about 100-300 nm which played a dominant role in generating charges in the solar cell devices.

Even though the perovskite has attracted a wide investigations due to their unique light absorber for solar cells with the record PCE of 25.2%, in a monolithic perovskite/silicon tandem configuration,[33] its Achilles heel is the moisture instability. The limitation prevents them to satisfy the strict international standards for outdoor photovoltaic applications. Various studies have been conducted to improve the stability of perovskites including encapsulation, single-crystal growth, and 2D layered material replacements.

Another concern for the lead halide perovskite applications should be the toxicity of lead content. The heavy metal toxicity has been a main threat which relates to numerous health problems of human being. Various public health studies have been undertaken to investigate the harmful impacts of the heavy metals and found out that they remain in food chain and the human body due to our disability in self elimination of these kinds of metals.[34] Therefore, it is an important issue to replace the lead content of traditional perovskite materials.

1.2 Research Objectives

This thesis aims to synthesize and investigate the 3D and 2D layered hybrid perovskite single crystals by:

- Growing the 3D lead trihalide perovskite single crystals, 2D layered metal halide perovskite single crystals using solution crystallization methods (e.g. inverse temperature crystallization, anti-solvent, and supersaturation methods).
- Exploring the novel methods to reduce the time-consumption and enhance the high quality of the single crystals.
- Characterizing the structure, optical, photonic, electric, and phase-transfer properties of as-prepared single crystals.

1.3 Dissertation Overview

Chapter 1 is shown with a brief introduction about the background, motivation and research objectives of the thesis. More detailed information relating to the perovskite structure, the strategies to enhance the perovskite stability of the cells, and growth methods for single crystals will be reviewed in the Literature Review of Chapter 2. In chapter 3, the synthesis method and characterization for as-prepared single crystal is introduced. Chapter 4 reports the synthesis and characterizations of 2D layered $(C_6H_5C_2H_4NH_3)_2PbCl_4$ single crystals using solution process. In the attempt to replace the lead content of perovskite system, Chapter 6 will present the synthesis of 2D layered lead-free $(C_6H_5C_2H_4NH_3)_2CuCl_4$ single crystals using DI water solvent and low temperature. A device using the 2D lead-free single crystal is also undertaken to investigate for piezoelectric. Chapter 7 will present the growth process of 3D $CH_3NH_3PbI_3$ single crystals and their fully characterization. The $CH_3NH_3Br_3$ and $CH_3NH_3Cl_3$ single crystal crystallization processes are shown in chapter 8, the electric property using AFM is also introduced. Finally, Chapter 9 will conclude the project and provide some further recommendations.

1.4 Findings and Outcomes/Originality

The novel solvent crystallization method reporting in the thesis can help to synthesize single crystals faster at a lower temperature than previous reports but remain the high quality of the single crystals. The 2D layered perovskites which are exfoliable to thin flake samples show the phase transition behaviour. The results help to overcome clamping effect in piezoelectric thin film devices.

1.5 References

1 Im, J. H., Lee, C. R., Lee, J. W., Park, S. W. & Park, N. G. 6.5% efficient perovskite quantum-dot-sensitized solar cell. *Nanoscale* **3**, 4088-4093, doi:10.1039/c1nr10867k (2011).

2 Wehrenfennig, C., Eperon, G. E., Johnston, M. B., Snaith, H. J. & Herz, L. M. High Charge Carrier Mobilities and Lifetimes in Organolead Trihalide Perovskites. *Advanced Materials* **26**, 1584-1589, doi:10.1002/adma.201305172 (2014).

3 Edri, E. *et al.* Why lead methylammonium tri-iodide perovskite-based solar cells require a mesoporous electron transporting scaffold (but not necessarily a hole conductor). *Nano Lett* **14**, 1000-1004, doi:10.1021/nl404454h (2014).

4 Xing, G. *et al.* Long-range balanced electron- and hole-transport lengths in organic-inorganic CH3NH3PbI3. *Science* **342**, 344-347, doi:10.1126/science.1243167 (2013).

5 Kim, H. S. *et al.* Lead iodide perovskite sensitized all-solid-state submicron thin film mesoscopic solar cell with efficiency exceeding 9%. *Sci Rep* **2**, 591, doi:10.1038/srep00591 (2012).

6 Lee, M. M., Teuscher, J., Miyasaka, T., Murakami, T. N. & Snaith, H. J. Efficient hybrid solar cells based on meso-superstructured organometal halide perovskites. *Science* **338**, 643-647, doi:10.1126/science.1228604 (2012).

7 Burschka, J. *et al.* Sequential deposition as a route to high-performance perovskite-sensitized solar cells. *Nature* **499**, 316-319, doi:10.1038/nature12340 (2013).

8 Jeon, N. J. *et al.* Compositional engineering of perovskite materials for high-performance solar cells. *Nature* **517**, 476-480, doi:10.1038/nature14133 (2015).

9 Liu, M., Johnston, M. B. & Snaith, H. J. Efficient planar heterojunction perovskite solar cells by vapour deposition. *Nature* **501**, 395-398, doi:10.1038/nature12509 (2013).

10 Nie, W. *et al.* High-efficiency solution-processed perovskite solar cells with millimeter-scale grains. *Science* **347**, 522-525, doi:10.1126/science.aaa0472 (2015).

11 Li, X. *et al.* Improved performance and stability of perovskite solar cells by crystal crosslinking with alkylphosphonic acid ω-ammonium chlorides. *Nat Chem* **7**, 703-711, doi:10.1038/nchem.2324 http://www.nature.com/nchem/journal/v7/n9/abs/nchem.2324.html#supplementary-information (2015).

12 Zhou, H. *et al.* Interface engineering of highly efficient perovskite solar cells. *Science* **345**, 542-546 (2014).

13 Yang, W. S. *et al.* High-performance photovoltaic perovskite layers fabricated through intramolecular exchange. *Science* **348**, 1234-1237, doi:10.1126/science.aaa9272 (2015).

14 Hu, X. *et al.* High-Performance Flexible Broadband Photodetector Based on Organolead Halide Perovskite. *Adv. Funct. Mater.* **24**, 7373–7380, doi:10.1002/adfm.201402020 (2014).

15 Zhuo, S., Zhang, J., Shi, Y., Huang, Y. & Zhang, B. Self-Template-Directed Synthesis of Porous Perovskite Nanowires at Room Temperature for High-Performance Visible-Light Photodetectors. *Angew. Chem. Int. Ed.* **54**, 5693-5696, doi:10.1002/anie.201411956 (2015).

16 Deng, H. *et al.* Growth, Patterning and Alignment of Organolead Iodide Perovskite Nanowires for Optoelectronic Devices. *Nanoscale* **7**, 4163-4170, doi:10.1039/C4NR06982J (2015).

17 Chin, X. Y., Cortecchia, D., Yin, J., Bruno, A. & Soci, C. Lead iodide perovskite light-emitting field-effect transistor. *Nat. Commun.* **6**, 7383, doi:10.1038/ncomms8383 (2015).

18 Stranks, S. D. & Snaith, H. J. Metal-halide perovskites for photovoltaic and light-emitting devices. *Nat Nano* **10**, 391-402, doi:10.1038/nnano.2015.90 (2015).

19 Xing, G. *et al.* Low-temperature solution-processed wavelength-tunable perovskites for lasing. *Nat Mater* **13**, 476-480, doi:10.1038/nmat3911 http://www.nature.com/nmat/journal/v13/n5/abs/nmat3911.html#supplementary-information (2014).

20 Zhu, H. *et al.* Lead halide perovskite nanowire lasers with low lasing thresholds and high quality factors. *Nat. Mater.* **14**, 636–642, doi:10.1038/nmat4271 http://www.nature.com/nmat/journal/vaop/ncurrent/abs/nmat4271.html#supplementary-information (2015).

21 Kojima, A., Teshima, K., Shirai, Y. & Miyasaka, T. Organometal halide perovskites as visible-light sensitizers for photovoltaic cells. *Journal of the American Chemical Society* **131**, 6050-6051 (2009).

22 Dualeh, A. *et al.* Effect of Annealing Temperature on Film Morphology of Organic-Inorganic Hybrid Pervoskite Solid-State Solar Cells. *Advanced Functional Materials* **24**, 3250-3258, doi:10.1002/adfm.201304022 (2014).

23 Xiao, Z. *et al.* Solvent Annealing of Perovskite-Induced Crystal Growth for Photovoltaic-Device Efficiency Enhancement. *Adv. Mater.* **26**, 6503–6509, doi:10.1002/adma.201401685 (2014).

24 Zheng, X., Chen, B., Wu, C. & Priya, S. Room temperature fabrication of CH3NH3PbBr3 by anti-solvent assisted crystallization approach for perovskite solar cells with fast response and small J–V hysteresis. *Nano Energy* **17**, 269-278, doi:http://dx.doi.org/10.1016/j.nanoen.2015.08.023 (2015).

25 Zhou, Y. *et al.* Growth Control of Compact CH3NH3PbI3 Thin Films via Enhanced Solid-State Precursor Reaction for Efficient Planar Perovskite Solar Cells. *J. Mater. Chem. A* **3**, 9249-9256, doi:10.1039/C4TA07036D (2015).

26 Kim, H.-S. *et al.* Lead iodide perovskite sensitized all-solid-state submicron thin film mesoscopic solar cell with efficiency exceeding 9%. *Scientific reports* **2** (2012).

27 Lee, M. M., Teuscher, J., Miyasaka, T., Murakami, T. N. & Snaith, H. J. Efficient hybrid solar cells based on meso-superstructured organometal halide perovskites. *Science* **338**, 643-647 (2012).

28 Noh, J. H., Im, S. H., Heo, J. H., Mandal, T. N. & Seok, S. I. Chemical management for colorful, efficient, and stable inorganic–organic hybrid nanostructured solar cells. *Nano letters* **13**, 1764-1769 (2013).

29 Burschka, J. *et al.* Sequential deposition as a route to high-performance perovskite-sensitized solar cells. *Nature* **499**, 316-319 (2013).

30 Jeon, N. J. *et al.* Solvent engineering for high-performance inorganic–organic hybrid perovskite solar cells. *Nature materials* (2014).

31 Ryu, S. *et al.* Voltage output of efficient perovskite solar cells with high open-circuit voltage and fill factor. *Energ Environ Sci* **7**, 2614-2618, doi:10.1039/C4EE00762J (2014).

32 Sahli, F. *et al.* Fully textured monolithic perovskite/silicon tandem solar cells with 25.2% power conversion efficiency. *Nature Materials* **17**, 820-826, doi:10.1038/s41563-018-0115-4 (2018).

33 Jaishankar, M., Tseten, T., Anbalagan, N., Mathew, B. B. & Beeregowda, K. N. Toxicity, mechanism and health effects of some heavy metals. *Interdisciplinary Toxicology* **7**, 60-72, doi:10.2478/intox-2014-0009 (2014).

Chapter 2

Literature Review

2.1 Organometal Trihalide Perovskites structures

Perovskites originated from the discovery of $CaTiO_3$ by the Russian mineralogist Lev Perovski, who first characterized this structure. Later, lots of materials with the same crystal structure were discovered and more perovskites possess a similar formula of AMX_3, where M is a metal cation, A is a cation, and X is an oxide or a halide anion. Perovskite matrix is a merging of two cubic structures with 8 A cations placed at 8 vertices of a cube with M cation at the center. M cation also belongs to an M-centered octahedron forming by six X anions which located at six facet centers of the cube (Fig. 2.1a).

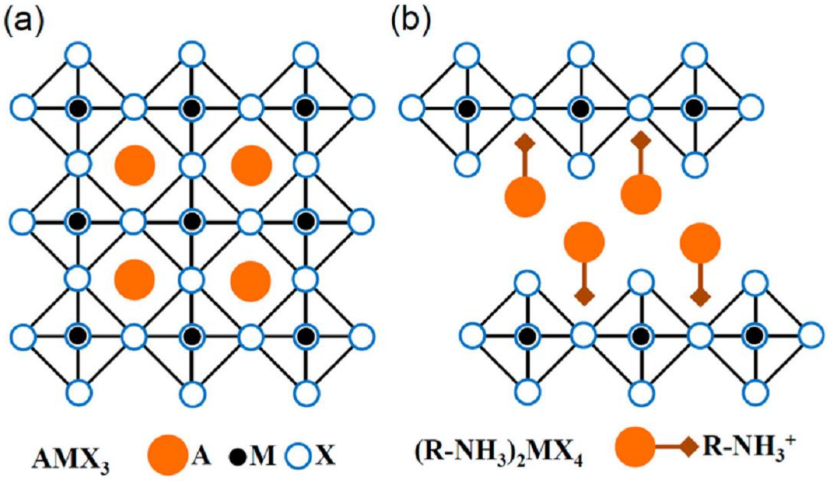

Figure 2.1 The crystal structures of the family of perovskite. (a) The AMX_3 perovskite structure and (b) the 2D layered $(R{-}NH_3)_2MX4$ perovskite structure (adopted from [1]).

The cubic geometry structure could be distorted to orthorhombic or rhombohedral ones when replacing A and M cations by other elements. The physical and optical properties of perovskites can be affected by these structural distortions. Particularly, the A and M sizes also have an impact on its lattice structures, and regulate the perovskite properties.[2]

In an intercalation of organic and inorganic on the molecular scale, the hybrid perovskites have attracted a special interest due to their unique structures. Typically, the organic group is an alkyl chain (Fig. 2.1). These hybrid perovskites are promising due to their signature optoelectronic properties. Additionally, organic layers help to designate the level of electronic properties and inner interactions in the inorganic layers[3]. Importantly, these perovskite thin films can be easily prepared by a low-cost process using low temperatures.

Herein, the hybrid lead halide perovskite ($CH_3NH_3PbI_3$), where A = $CH_3NH_3^+$, M = Pb^{2+}, and X = I^-, will be studied. The lead halide perovskite crystal structure is represented in Fig. 2.2.

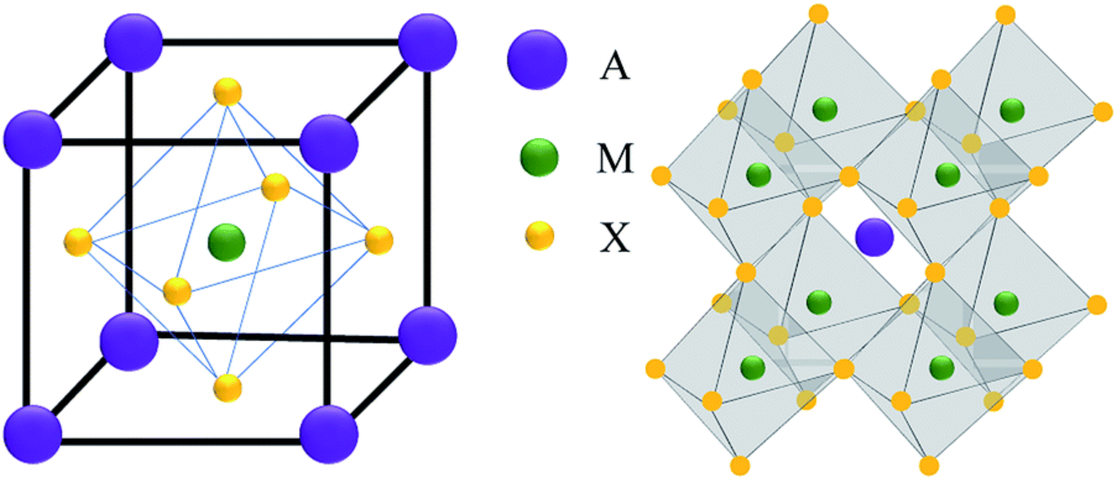

Figure 2.2 The 3D Lead Halide Perovskite structure of the $CH_3NH_3PbI_3$ Crystal.

A direct band gap of $CH_3NH_3PbI_3$ has been determined in the study of Kim et al.[4]. The optical band gap with a value of Eg = 1.5 eV was reported for $CH_3NH_3PbI_3$ deposited on mesoporous TiO_2. Schulz et al estimated that the position of the valence band energy was E_V = -5.43 eV below vacuum level, and the position of the conduction band is at E_C = -3.93 eV vs. vacuum.[5] Diffusion lengths of 130 nm for electrons and 90 nm for holes were also reported for $CH_3NH_3PbI_3$. In comparison to the report of Xing, the diffusion length of colloidal quantum dot films is about 30 nm, and different-method-prepared organic-conjugated materials is about 10 to 50 nm.[6]

2.2 Strategies in improving the stability of Organometal Trihalide Perovskites

Considering a reference perovskite cell using a layer of hole transport material, namely spiro-OMeTAD, with LiTFSI and TBP dopants. The material was coated on a layer of $CH_3NH_3PbI_3$ which was loaded into a layer of mesoporous TiO_2. Typical attempts to improve the cell stability would be introduced as follows.

2.3 Modifications of the traditional PSC components

2.3.1 Perovskite Modification

The perovskite cubic structure could be modified to rhombohedral or orthorhombic ones when A and M are substituted by other kinds of cations, leading to the changes of these electric and optical properties due to the structural distortions. The modification in perovskite properties can be conducted by replacing the size of A and X cations.[2] It is demonstrated to greatly improve the perovskite stability by regulating these compounds without losing the cell performances.[2,7,8]

In 2013, an attempt to modify the sensitizer $CH_3NH_3PbI_3$ was conducted by the group of Seok.[7] In this work, the ratio of I : Br in the perovskite of $MAPb(I_{1-x}Br_x)_3$ was modified with $x = 0, 0.06, 0.20$, and 0.29, based on the fact that $MAPbBr_3$ is more stable than $MAPbI_3$,[2,9] After the high humidity (55%) exposition for one day and 35% of humidity on following days, the $MAPb(I_{1-x}Br_x)_3$ solar cells were all more stable than the $CH_3NH_3PbI_3$ ones as expectation. The I: Br ratio of $x = 0.20$ provided the highest PCE and longest stability for 20 days (see Fig. 2.3a). It was also shown that during the first 6 days, the cells with ratios of $x = 0.20$ and 0.29 indicated an increasing tendency in PCE, for which the mechanism was not clear.

In the same way, the I: Cl mixed-halide perovskite $CH_3NH_3PbI_2Cl$ was also observed to have a remarkable stability during the air exposition. The absorption spectrum (Fig. 2.3b) retain its flattened chart over 1000 h during a constant sunlight illumination.[10]

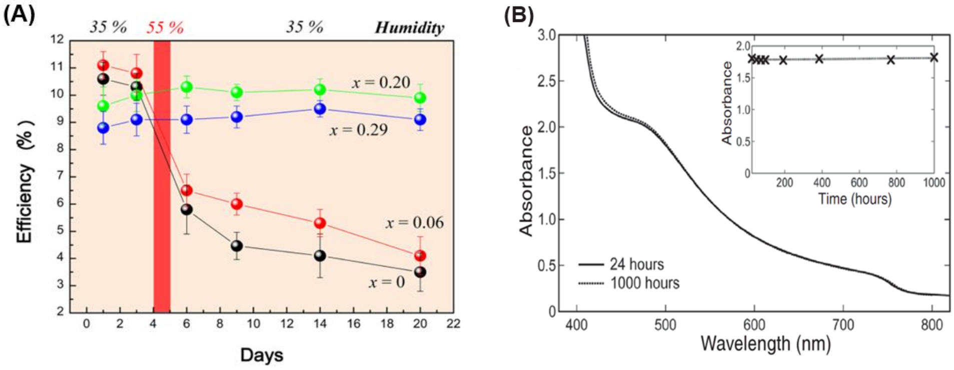

Figure 2.3 (A) Room temperature variation in PCE of the encapsulated $MAPb(I_{1-x}Br_x)_3$ solar cells in air at different humidity. After 20 days of air exposition, the cells with I : Br ratio of x = 0.2 shows the longest stability (adopted from [7]) (B) UV-Vis absorption spectra of the cells. Inset is its flattened absorbance chart over 1000 h during constant illumination (adopted from [10]).

Beside the composition of hybrid lead halide perovskite $MAPbX_3$, the compounds with a longer chain including $(CH_3NH_3)(C_6H_5(CH_2)_2NH_3)_2Pb_2I_7$ and $(C_6H_5(CH_2)_2NH_3)_2PbX_4$ (where X = Cl, Br, I) have been prepared. The alkylammonium cations can be changed from $C_6H_5C_2H_4NH_3$ to $C_nH_{2n+1}NH_3$ or $H_3NC_nH_{2n}NH_3$ (n = 4, 6, 8, 9, 10...) which the 2-D networks of PbI_4 play the role of anion components.[11]

The hygroscopic amine salts are the major cause which leads to the fast moisture degradation of lead halide perovskites which limits perovskites to practical applications. Changing alkylammonium chains to hydrophobic longer chains including $(C_6H_5(CH_2)_2NH_3)_2(CH_3NH_3)_2$ or $C_6H_5(CH_2)_2NH_3$ instead of the CH_3NH_3 can enhance the perovskite stability. Smith and co-workers fabricated the first-generation $(C_6H_5(CH_2)_2NH_3)_2(MA)_2[Pb_3I_{10}]$ solar cell that exhibited a stability for 46 days at the room temperature upon a 52% humidity exposition. The XRD results demonstrated the cell stability by the disappearance of any additional peak in the patterns (see Fig 2.4A).[12]

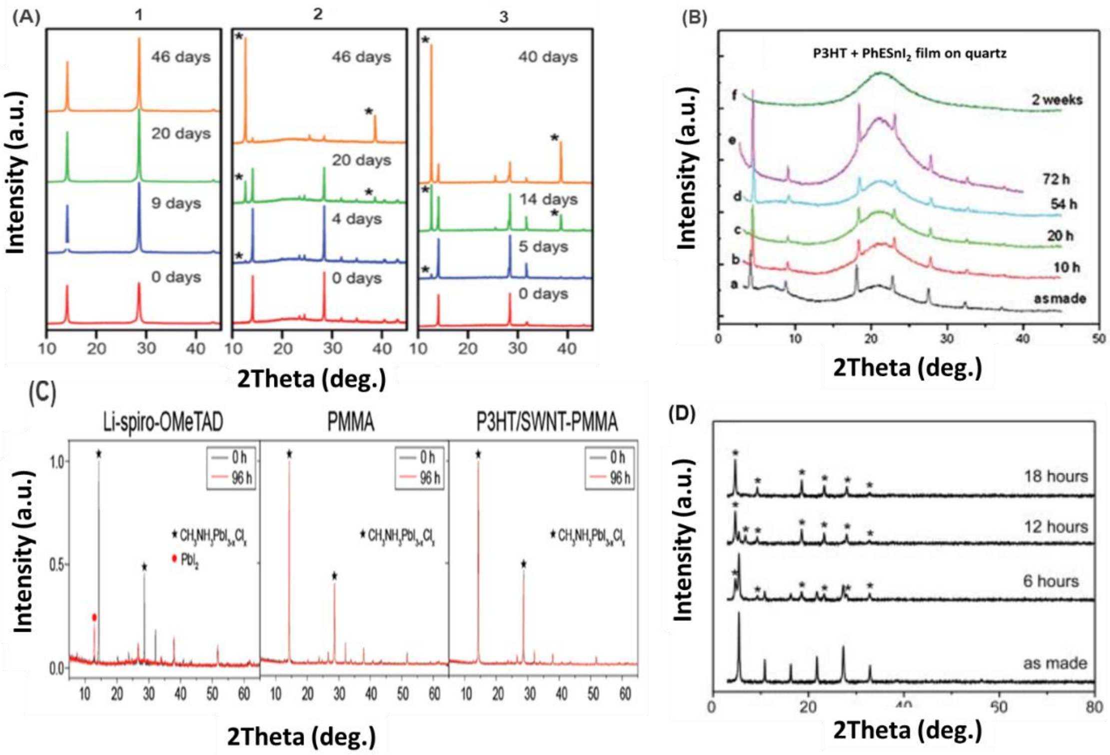

Figure 2.4 The stability test data using XRD (A) XRD patterns of $(PEA)_2(MA)_2[Pb_3I_{10}]$ (1), $(MA)[PbI_3]$ films based on PbI_2 (1a), and with ratio of $PbCl_2$:(MA)I of 1:3 (2b).[12] (B) Stability of a blend $(PEA)_2SnI_4/P_3HT$ film spin coateing on quartz. (C) XRD patterns stability after 96 h heat exposure of devices based on Li-spiro-OMeTAD, PMMA, and P3HT/SWNT-PMMA HTMs (adopted from [13]). (D) Stability of the spin-coated pure $(PEA)_2SnI_4$ film in air exposure (adopted from [2]).

The cell stability is also an important issue for tin-based halide perovskites.[14] Since the 1990's, the powder of $(C_nH_{2n+1}NH_3)_2SnX_3$ as well as $(CH_3NH_3)(C_nH_{2n+1}NH_3)_2Sn_2I_7$ tin halide perovskites have been synthesized by the Papavassiliou et al.[11] The reported characteristic features of these perovskites included the narrow luminescence bands and the excitonic absorption. Additionally, the pure crystalline form and spectroscopic data of $(C_6H_5(CH_2)_2NH_3)_2SnX_4$ (X = I, Br) are also reported. The spin-coated blend films were prepared using the $(C_6H_5(CH_2)_2NH_3)_2SnI_4$ precursor solution in tetrahydrofuran (THF) solvent adding P3HT. As shown in the XRD patterns (Fig. 2.4B), the layered blend film was stable during the air exposure for at least 72 h comparing to several hours decomposition of the pure film (without P3HT) (Fig. 2.4D).[2]

2.3.2 Additive Modification for the Hole Transport Materials

Since the negative influence of the conventional TBP and LiTFSI additives in spiro-OMETAD to perovskite cells, researching other kinds of Hole Transport Materials and dopants should be an appropriate way to enhance the PSC stability. In the work of the Zheng group, a material, namely DR3TBDTT, which is a high hydrophobic oligothiophene derivate, was introduced as an “additive-free” HTM in a 4.9% PEC perovskite cell.[15] After that, by doping a new additive PDMS to a controlled $CH_3NH_3PbI_{3-x}Cl_x$ cell, the PEC increased close to 8.9% (Fig. 2.5A). After 3 days during 50% humidity exposition, the perovskite cells based on DR3TBDT/PDMS exhibited a longer stability than the traditional cells. The 8.8% of PEC reduced to 8.0% comparing with a reduction of the controlled device from 8.9 to 3.9%. The additive-free hole transport films also exhibited a 107.41^{o} water contact angle since its hydrophobic property effectively prevents the water penetration into the perovskite (see Fig. 2.5B).

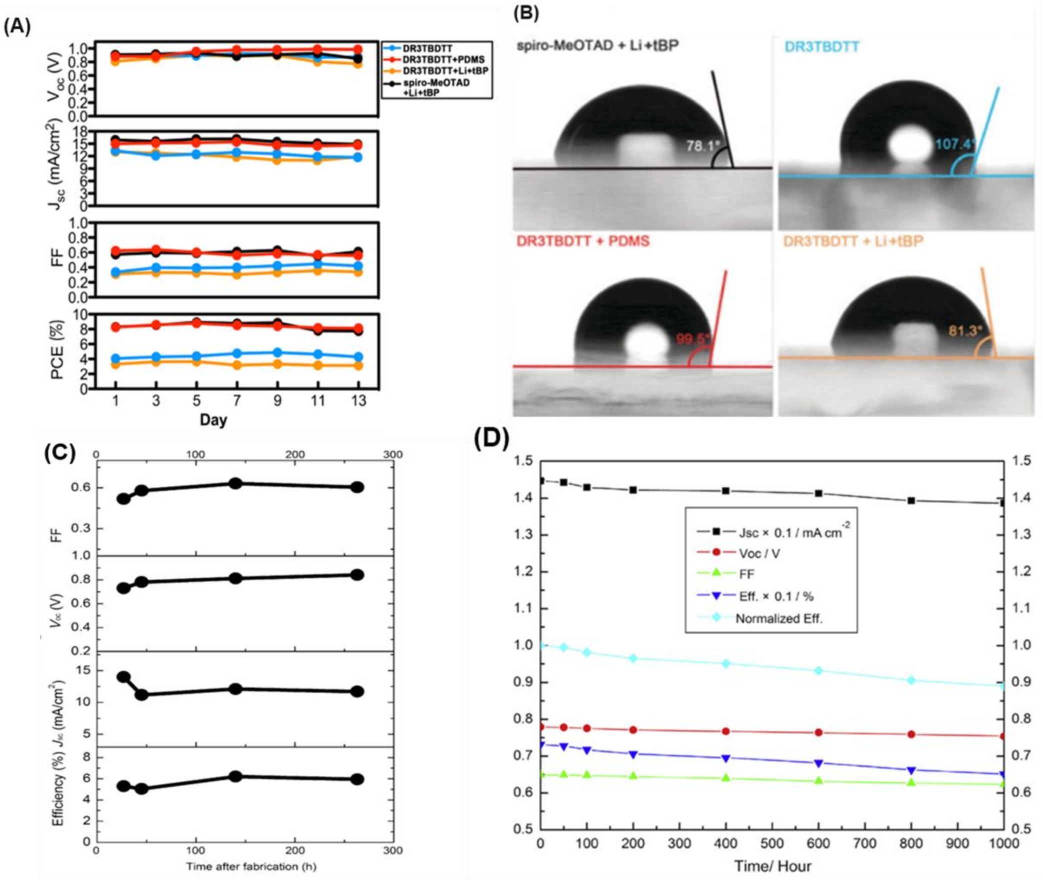

Figure 2.5 (A) Room temperature evolution of photovoltaic parameters of air-storing cells using DR3TBDTT and Spiro-OMeTAD HTMs with and without additives . (B) Water contact angles (adopted from [15]); (C) Stability of the $CH_3NH_3PbI_2Br$ cells adding P3HT to precursor solution (stability (adopted from [16]) and (D) Normalized Efficiency and photovoltaic performance time courses of the PANI based cells (adopted from [17]).

Using hole transport material without dopant has been a potential approach. In the study of the Liu group, the tetrathiafulvalene derivative (TTF-1) was employed as a dopant-free HTM.[18] The TTF-1 material exhibited its promising by improving the cell stability up to three times (360 h) comparing with a traditional one using spiro-OMeTAD (120 h) in air at 40% relative humidity.

In 2014, Li and co-workers introduced a work introducing a montmorillonite (MMT) layer on the perovskite surface. The MMT-TBP intercalation improved the direct contact between the TBP and perovskite layer thus enhances the cell stability.[19] Moreover, the limitation of charge recombination in the cell by using MTT leads to a PCE of 11.9% compared to 9 % of the without-MMT cell.

2.3.3 Polymer Hole Transport Materials

Another limitation that may limit perovskite cells to come out the market should be the high price of spiro-MeOTAD (see Table 2.1).

The spiro-MeOTAD and $CH_3NH_3PbI_3$ replacements by employing a dopant-free P3HT and $CH_3NH_3PbI_2Br$ for the PSCs, respectively, have been introduced by Zhang et al. in 2015.[16] The cells without any encapsulation exhibited their good efficiency stability about 6% of PCE after 250 h in air exposition while using a cheaper HTM and a more stable sensitizer (Fig. 2.5C). As a result, the replacements helped to solve both cost and stability issues for PSCs.

The Xiao group introduced a new device design by employing a dual-function polyaniline (PANI) for both sensitizer and hole transport materials.[17] The PANI solar cell with a 7.34% of PCE reduced its efficiency to 6.71% after 1000 h, which equals to a 91.42% retention in efficiency (Fig. 2.5D).

Table 2.1**:** A comparison in HTM cost for different solar cell configurations (adopted from [16]).

Cell structure	**Light sensitizer**	**HTM**	**Concentration** (HTM) **[mg mL^{-1}]**	**Cost** (HTM) **mL^{-1} [AU $]**
Mesoscopic	$CH_3NH_3PbI_3$	Spiro[20]	72.3	93
Mesoscopic	$CH_3NH_3PbI_{3-1}Cl_x$	Spiro[21]	88 (8 wt. %)	113
Planar	$CH_3NH_3PbI_3$	Spiro[22]	180	231
Mesoscopic	$CH_3NH_3PbI_3$	Spiro[4]	208 (0.170 M)	267
Nanowire	$CH_3NH_3PbI_2Br$	Spiro[23]	208 (0.170 M)	267
Mesoscopic	$CH_3NH_3PbI_3$	P3HT[24]	15	12
Planar	$CH_3NH_3PbI_{3-1}Cl_x$	P3HT[25]	16.6 (1.5 wt. %)	13
Mesoscopic	$CH_3NH_3PbI_3$	P3HT[26]	20	16
Mesoscopic	$CH_3NH_3PbI_2Br$	P3HT[16]	10	8

The negative role of the additive Li-TFSI in the cell degrading acceleration has been demonstrated by the Snaith group in 2014.[13] The faster degradation phenomenon of cells with and without Li-TFSI doped in spiro-OMeTAD was explained by its negative role in introducing water into the device. Then, an insulating poly(methyl methacrylate) (PMMA) polymer was exhibited the ability of retarding the cell degradation (Fig. 2.4C). Single-walled carbon nanotubes (SWNTs), along with P3HT, were combined with PMMA to improve the charge transporting ability of the polymer. The composite exhibited its protective ability, water resistance as well as thermal stability for the cell. The performed PCE was risen up to 15.3% with a 10 ± 2% in term of the average value. More remarkably, the device could still operate after dipping in water for 60 s demonstrating an impressive advance for high-efficiency and long-term stability of PSCs.

2.3.4 Surface Treatment and Inorganic Hole Transport Material

The idea for replacing the traditional spiro-OMeTAD with the inorganic hole transport material has been inspired by its cost which is ten times more expensive than Au and Pt. Since the CuI material is stable, cheap, and solution-processable, and has suitable band-edges for perovskite solar cell, the Christians group introduced the CuI as a hole conductor layer.[27] . The cells performed a PCE of 6.0%, which is close to that of the spiro-OMETAD based ones (7.9%) at the time the work was published. More importantly, the cell current retained its initial value for 2 h under continuous AM 1.5G light exposure, comparing to a 10% degradation of the spiro-OMETAD based one.

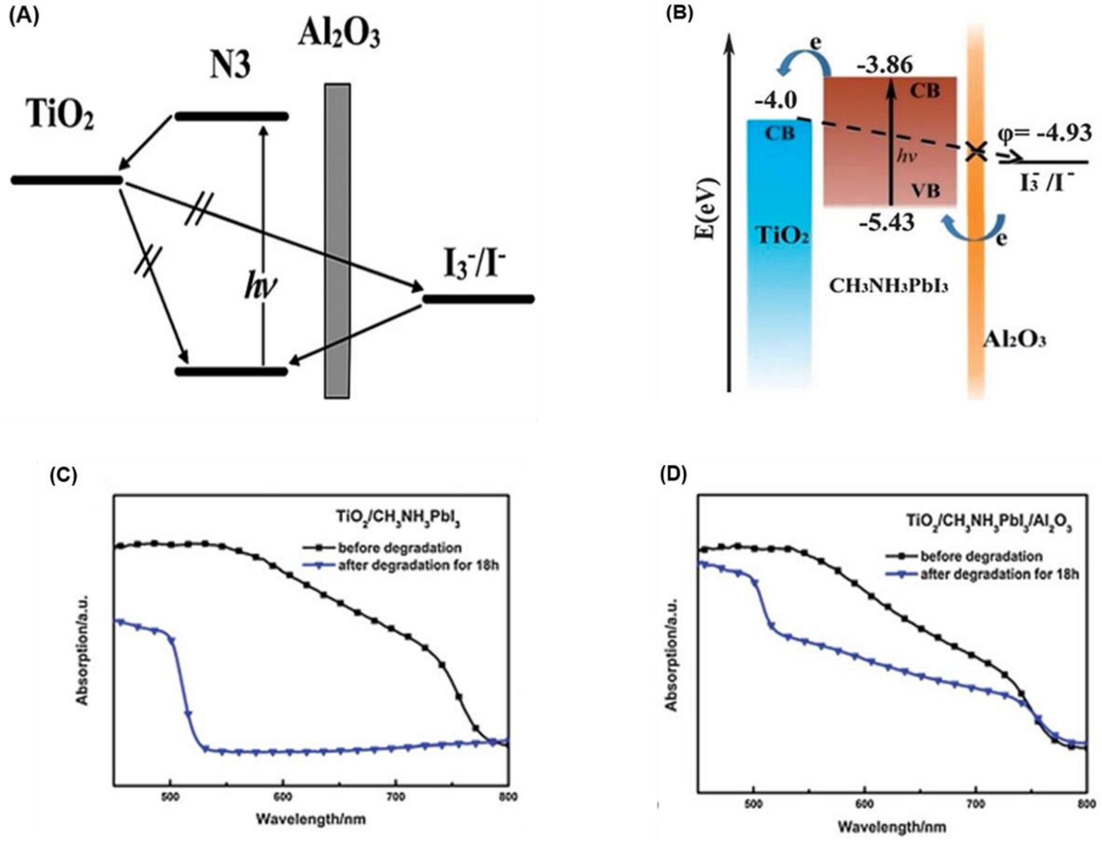

Figure 2.6 (A and B) Explaination of the interfacial charge transport processes taking place at interface of the TiO_2/dye (or perovskite)/Al_2O_3/electrolyte in a DSSC (adopted from [29,31]). The light absorption before and after 18 h of stability test for the samples (C) without Al_2O_3 and (D) with Al_2O_3 (adopted from [33]).

The photoanode of the cell is the contacting part to the electrolyte of the working environment. A feasible photoanode surface treatment has been a promising approach for cell stability enhancements. Major studies have focused on some Al_2O_3, SiO_2, ZnO thin oxide films which could be employed as a photoanode protective layer in liquid-state DSSCs.[28-32] The main consideration of these oxide protective layers in the DSSCs could be the charge suppression. As shown in Fig. 2.6A, Al_2O_3 has a higher conduction band comparing to TiO_2, so that the electrons would be injected from the protective material to TiO_2. As a consequence, the suppression of charge recombination between TiO_2 and the electrolyte could be obviously happened.

Li and co-workers were engaged by the above idea to employ a protective layer for PSCs.[31] The as-prepared TiO_2/perovskite films were dipped into a aluminumtriethyl ($Al(C_2H_5)_3$ 25% w/w in hexane) solution. The authors found out that the protective layer can obstruct the perovskite sensitizer into electrolyte corrosion. Additionally, a PCE improvement from 3.56% to 6.12% was obtained. In a later work, the authors used the same protective layer in solid-state PSCs by coating Al_2O_3 on top of a Spiro-MeOTAD HTM (see Fig. 2.6B).[33] Figure 2.6C shows the light absorption of the films. In the cell device, the Al_2O_3 protective layers play two roles: (i) prevent the perovskite from the humidity degradation and (ii) retard the electron recombination between TiO_2 and HTM. As a result, under sunlight exposure for 18 h with 60% humidity, the absorption of the Al_2O_3-modified perovskite cell was remained to certain degree even though degradation, comparing with a sharp drop in absorption spectrum for the without protective layer device.

Beside the idea of using the oxide protective layer for stabilization of PSC cells, metal layers have been recently employed by Da et al. The Cr, Co, and Ni layers were sputtered above an 80 nm Au cathode.[34] It was found out that after 12 days in ambient environment, the 8 nm Ni layer PSC retained PEC of around 12% which was evidently more stable than the bare PSC one (reduced from about 12% to 9%). For the photoelectrochemical water splitting tandem cell using PSC + Fe_2O_3 photoanode, Ni layer with a thickness of 8 nm were sputtered on the photoanode and showing a remarkable stability. Therefore, Ni is believed to act both catalyst for water oxidation reaction and protective layer of the perovskite cell.

Nevertheless, applying perovskite solar cells in PEC water splitting application has been a challenge. One of the possible approaches belongs to Luo and his co-workers who combined the PSC with electrocatalysts.[35]

2.4 Single Crystal of Organometal Trihalide Perovskites

Even though photovoltaic performances of hybrid PSCs have been advancing recently by using $MAPbX_3$ thin films, the improvements of efficiency and stability are also major issues. One of the promising approaches is using single crystals instead. The high-quality single crystals possess a continuous crystal lattice, less of bulk defects and low charge recombination relative to the grain boundary. Due to the above advances, the single crystals have been inspired more and more studies focusing on their optoelectronic, photonic, electric, and mechanical properties.[36-38] Comparing to the thin film counterpart, the perovskite single crystals have superior properties including a extremely low trap density (10^9–10^{10} cm^{-3}), a long diffusion length (>175 μm) as well as a high carrier mobility (164 ± 25 cm^2 V^{-1} s^{-1}). [39-42] Therefore, the optoelectronic devices based on the hybrid perovskite single crystal are worthy undertaken.

2.5 References

1 Snaith, H. J. Perovskites: The Emergence of a New Era for Low-Cost, High-Efficiency Solar Cells. *The Journal of Physical Chemistry Letters* **4**, 3623-3630, doi:10.1021/jz4020162 (2013).

2 Cheng, Z. & Lin, J. Layered organic–inorganic hybrid perovskites: structure, optical properties, film preparation, patterning and templating engineering. *CrystEngComm* **12**, 2646-2662 (2010).

3 Mitzi, D. B. Solution-processed inorganic semiconductors. *Journal of Materials Chemistry* **14**, 2355-2365, doi:10.1039/B403482A (2004).

4 Kim, H.-S. *et al.* Lead iodide perovskite sensitized all-solid-state submicron thin film mesoscopic solar cell with efficiency exceeding 9%. *Scientific reports* **2** (2012).

5 Schulz, P. *et al.* Interface energetics in organo-metal halide perovskite-based photovoltaic cells. *Energ Environ Sci* **7**, 1377-1381 (2014).

6 Xing, G. *et al.* Long-range balanced electron-and hole-transport lengths in organic-inorganic CH3NH3PbI3. *Science* **342**, 344-347 (2013).

7 Noh, J. H., Im, S. H., Heo, J. H., Mandal, T. N. & Seok, S. I. Chemical management for colorful, efficient, and stable inorganic–organic hybrid nanostructured solar cells. *Nano letters* **13**, 1764-1769 (2013).

8 Mitzi, D. B. *et al.* Hybrid field-effect transistor based on a low-temperature melt-processed channel layer. *Advanced materials* **14**, 1772-1776 (2002).

9 Mosconi, E., Amat, A., Nazeeruddin, M. K., Grätzel, M. & De Angelis, F. First-principles modeling of mixed halide organometal perovskites for photovoltaic applications. *The Journal of Physical Chemistry C* **117**, 13902-13913 (2013).

10 Lee, M. M., Teuscher, J., Miyasaka, T., Murakami, T. N. & Snaith, H. J. Efficient hybrid solar cells based on meso-superstructured organometal halide perovskites. *Science* **338**, 643-647 (2012).

11 Papavassiliou, G. C. *et al.* Preparation and Characterization of (C~ 6H~ 5CH~ 2CH~ 2NH~ 3)~ 2SnI~ 4 and (C~ 6H~ 5CH~ 2CH~ 2NH~ 3)~ 2SnBr~ 4. *ZEITSCHRIFT FUR NATURFORSCHUNG B* **48**, 1013-1013 (1993).

12 Smith, I. C., Hoke, E. T., Solis-Ibarra, D., McGehee, M. D. & Karunadasa, H. I. A layered hybrid perovskite solar-cell absorber with enhanced moisture stability. *Angewandte Chemie International Edition* **53**, 11232-11235, doi:10.1002/anie.201406466 (2014).

13 Habisreutinger, S. N. *et al.* Carbon nanotube/polymer composite as a highly stable charge collection layer in perovskite solar cells. *Nano letters* (2014).

14 Umari, P., Mosconi, E. & De Angelis, F. Relativistic GW calculations on CH3NH3PbI3 and CH3NH3SnI3 Perovskites for Solar Cell Applications. *Scientific reports* **4**, 4467, doi:doi:10.1038/srep04467 (2014).

15 Zheng, L. *et al.* A hydrophobic hole transporting oligothiophene for planar perovskite solar cells with improved stability. *Chemical communications* **50**, 11196-11199, doi:10.1039/c4cc04680c (2014).

16 Zhang, M. *et al.* Stable and Low-Cost Mesoscopic CH3 NH3 PbI2 Br Perovskite Solar Cells by using a Thin Poly(3-hexylthiophene) Layer as a Hole Transporter. *Chemistry* **21**, 434-439, doi:10.1002/chem.201404427 (2015).

17 Xiao, Y. *et al.* An all-solid-state perovskite-sensitized solar cell based on the dual function polyaniline as the sensitizer and p-type hole-transporting material. *Journal of Power Sources* **267**, 1-8 (2014).

18 Liu, J. *et al.* A dopant-free hole-transporting material for efficient and stable perovskite solar cells. *Energy & Environmental Science* **7**, 2963-2967, doi:Doi 10.1039/C4ee01589d (2014).

19 Li, W. *et al.* Montmorillonite as bifunctional buffer layer material for hybrid perovskite solar cells with protection from corrosion and retarding recombination. *Journal of Materials Chemistry A* **2**, 13587-13592 (2014).

20 Burschka, J. *et al.* Sequential deposition as a route to high-performance perovskite-sensitized solar cells. *Nature* **499**, 316-319 (2013).

21 Wojciechowski, K., Saliba, M., Leijtens, T., Abate, A. & Snaith, H. J. Sub-150° C processed meso-superstructured perovskite solar cells with enhanced efficiency. *Energy & Environmental Science* **7**, 1142-1147 (2014).

22 Chen, Q. *et al.* Planar heterojunction perovskite solar cells via vapor-assisted solution process. *Journal of the American Chemical Society* **136**, 622-625 (2013).

23 Qiu, J. *et al.* All-solid-state hybrid solar cells based on a new organometal halide perovskite sensitizer and one-dimensional TiO 2 nanowire arrays. *Nanoscale* **5**, 3245-3248 (2013).

24 Heo, J. H. *et al.* Efficient inorganic-organic hybrid heterojunction solar cells containing perovskite compound and polymeric hole conductors. *Nature photonics* **7**, 486-491 (2013).

25 Conings, B. *et al.* Perovskite-Based Hybrid Solar Cells Exceeding 10% Efficiency with High Reproducibility Using a Thin Film Sandwich Approach. *Advanced materials* **26**, 2041-2046 (2014).

26 Bi, D. *et al.* Efficient and stable CH3NH3PbI3-sensitized ZnO nanorod array solid-state solar cells. *Nanoscale* **5**, 11686-11691, doi:10.1039/c3nr01542d (2013).

27 Christians, J. A., Fung, R. C. & Kamat, P. V. An inorganic hole conductor for organo-lead halide perovskite solar cells. Improved hole conductivity with copper iodide. *Journal of the American Chemical Society* **136**, 758-764, doi:10.1021/ja411014k (2014).

28 Law, M. *et al.* ZnO-Al2O3 and ZnO-TiO2 core-shell nanowire dye-sensitized solar cells. *The Journal of Physical Chemistry B* **110**, 22652-22663 (2006).

29 Luo, F., Wang, L., Ma, B. & Qiu, Y. Post-modification using aluminum isopropoxide after dye-sensitization for improved performance and stability of quasi-solid-state solar cells. *Journal of Photochemistry and Photobiology A: Chemistry* **197**, 375-381 (2008).

30 Palomares, E., Clifford, J. N., Haque, S. A., Lutz, T. & Durrant, J. R. Slow charge recombination in dye-sensitised solar cells (DSSC) using Al 2 O 3 coated nanoporous TiO 2 films. *Chemical Communications*, 1464-1465 (2002).

31 Li, W. *et al.* Post modification of perovskite sensitized solar cells by aluminum oxide for enhanced performance. *Journal of Materials Chemistry A* **1**, 11735-11740 (2013).

32 Liu, S.-Y. *et al.* Improved hydrogen gas generation rate of n-GaN photoelectrode with SiO2 Protection layer on the ohmic contacts from the electrolyte. *Journal of The Electrochemical Society* **157**, B266-B268 (2010).

33 Niu, G. *et al.* Study on the stability of CH 3 NH 3 PbI 3 films and the effect of post-modification by aluminum oxide in all-solid-state hybrid solar cells. *Journal of Materials Chemistry A* **2**, 705-710 (2014).

34 Da, P. *et al.* High-Performance Perovskite Photoanode Enabled by Ni Passivation and Catalysis. *Nano Letters* **15**, 3452-3457, doi:10.1021/acs.nanolett.5b00788 (2015).

35 Luo, J. *et al.* Water photolysis at 12.3% efficiency via perovskite photovoltaics and Earth-abundant catalysts. *Science* **345**, 1593-1596, doi:10.1126/science.1258307 (2014).

36 Brenner, T. M., Egger, D. A., Kronik, L., Hodes, G. & Cahen, D. Hybrid organic—inorganic perovskites: low-cost semiconductors with intriguing charge-transport properties. *Nature Reviews Materials* **1**, 15007, doi:10.1038/natrevmats.2015.7 (2016).

37 Saidaminov, M. I. *et al.* High-quality bulk hybrid perovskite single crystals within minutes by inverse temperature crystallization. *Nature Communications* **6**, 7586, doi:10.1038/ncomms8586

https://www.nature.com/articles/ncomms8586#supplementary-information (2015).

38 Maculan, G. *et al.* CH3NH3PbCl3 Single Crystals: Inverse Temperature Crystallization and Visible-Blind UV-Photodetector. *The Journal of Physical Chemistry Letters* **6**, 3781-3786, doi:10.1021/acs.jpclett.5b01666 (2015).

39 Baikie, T. *et al.* Synthesis and crystal chemistry of the hybrid perovskite (CH3NH3)PbI3 for solid-state sensitised solar cell applications. *Journal of Materials Chemistry A* **1**, 5628, doi:10.1039/c3ta10518k (2013).

40 Dang, Y. *et al.* Bulk crystal growth of hybrid perovskite material CH3NH3PbI3. *CrystEngComm* **17**, 665-670, doi:10.1039/c4ce02106a (2015).

41 Dong, Q. *et al.* Electron-hole diffusion lengths > 175 μm in solution-grown CH3NH3PbI3 single crystals. *Science* **347**, 967-970, doi:10.1126/science.aaa5760 (2015).

42 Shi, D. *et al.* Low trap-state density and long carrier diffusion in organolead trihalide perovskite single crystals. *Science* **347**, 519-522, doi:10.1126/science.aaa2725 (2015).

Chapter 3

Experimental Methodology

3.1 Fabrication of the perovskite cells

3.1.1 Fabrication of TiO_2 substrates

The substrates for PEC cell were fluorine doped tin oxide glass (FTO, resistance < 14 Ω\□, 2.2 nm of thickness, Pilkington). The FTO substrates were ultrasonic cleaned using DI water, ethanol and acetone. For the TiO_2 precursor preparation, a commercial TiO_2 paste (Dyesol DSL 30 NRD) was used, diluted 1:3.5 (wt) in absolute ethanol with stirring in 24h. The TiO_2 precursor (60 µl) was spin-coated on 3 ×3 cm FTO substrates (5000 rpm, 30 s). After drying for 15 min at 125^{o}C, the films were sintered for 30 min at 500^{o}C. The average mesoporous size is of about 20 nm.

3.1.2 Fabrication of perovskite layer

There are two methods to make the perovskite layer as shown in Fig. 3.1:

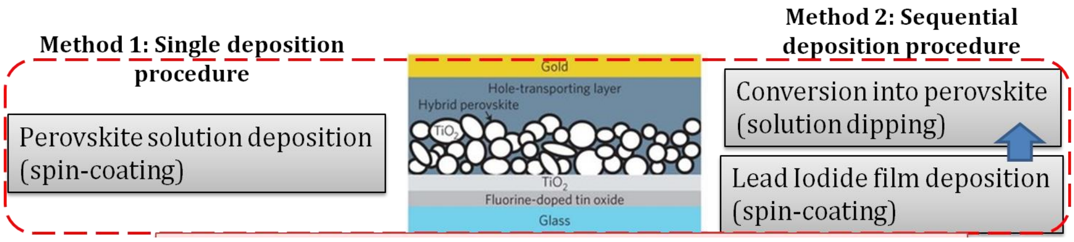

Figure 3.1 Two procedures for fabrication of perovskite solar cells

- The single procedure: Lead Halide perovskite ($CH_3NH_3PbI_3$) was prepared by mixing Methylammonium Iodide (CH_3NH_3I, 160.57 mg) and Lead Iodide (PbI_2, 470.33 MG, Aldrich) in 1 mL N, N-*dimethylformamide* (DMF, 99.8% Aldrich) at 70 °C with stirring inside glove box. In order to make perovskite layer, 40 microliters of perovskite precursor solution were spin-coated on the mesoporous TiO_2 layer at 4000 rpm for 30 s. Then the film was dried at 100 °C for 30 min.

- The sequential procedure: 461 mg PbI_2 was dissolved in 1 ml *N*, *N*-dimethylformamide (DMF, 99.8% Aldrich) at 70 °C to make 1M PbI_2 solution. 40

microliters of perovskite precursor solution were spin-coated on the mesoporous TiO_2 layer at 4000 rpm for 30 s. Then the film was dried at 100 °C for 10 min. The HTM was formed by the same way in the one-step coating procedure. Then the Au layer was fabricated by thermal evaporation method.

3.1.3 Single crystal growth methods

Based on the inverse temperature behaviour in solubility, the Inverse Temperature Crystallization (ITC) have been employed to grow the perovskite single crystals.[1-3] In this method, the room temperature precursor solutions are heated up to specific temperatures, in which the solubility of the materials is lower than that at room temperature. The residual amount of materials in the precursors will ignite to the crystallization. The solvents for ITC method should be GBL, DMF and the mixture of them with some antisolvents to accelerate the growth rates. The ICT method has been demonstrated its ability to grow the high-quality single crystals such as $CH_3NH_3PbX_3$ ($X = I, Br, Cl$).[1,4,5]

The second common growth technique should be the slow evaporation method. Since the evaporable solvents are used for the precursor solutions, the method has been through a slow evaporation of the solvent to increase the amount of materials in precursors as well as to reduce the volume of solvents used. Then, the material residues will promote the crystallizations. This is a facile growth method due to a fast rate but not an appropriate way to grow the high-quality single crystals.[5-9] Furthermore, the evaporated solvents may impact in a harmful way to the human being. However, for some 2D layered perovskite single crystals, the slow evaporation exhibits its irreplaceability. To grow the single crystal employing this method, a safe condition for growth process should be applied.

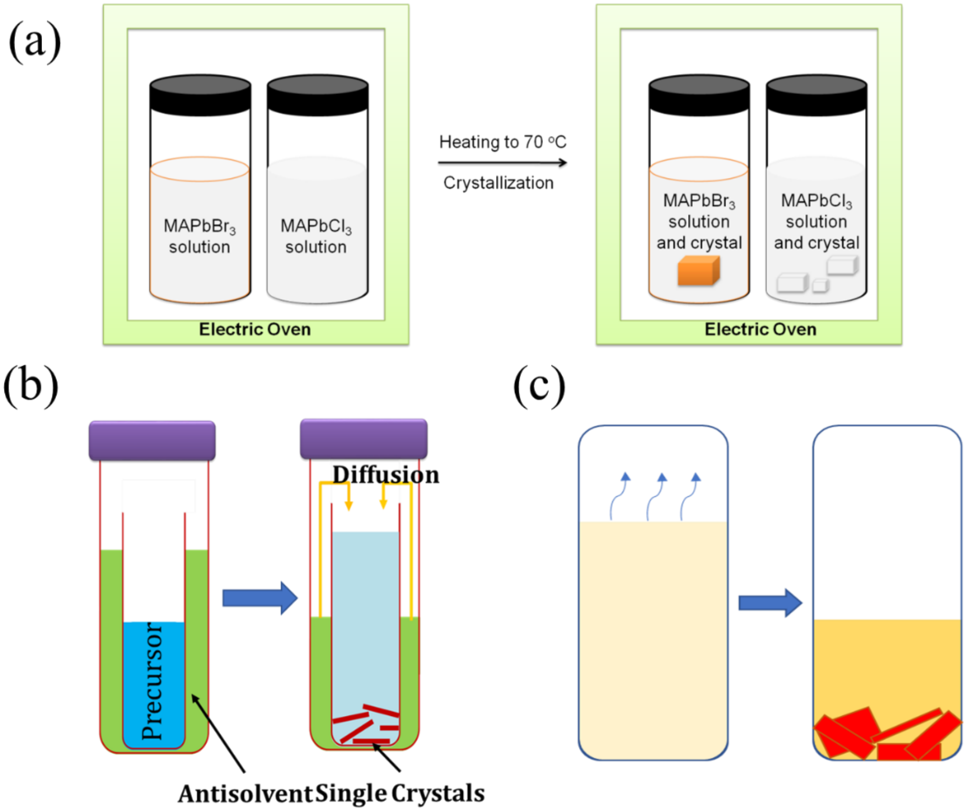

Figure 3.2 Illustrations of the perovskite growth technique (a) Inverse Temperature Crystallization method, (b) Antisolvent Crystallization method, and (c) Slow evaporation method.

Antisolvent Crystallization (AC) method should be placed in the third common growth technique. To apply the AC method, appropriate solvents, which possess a low solubility to the materials, are chosen with a specific ratio between antisolvent/solvent. Normally, the antisolvents play the role of decreasing the solubility of the precursor and thus ignite to the perovskite crystallization. Interestingly, the mixture solvents sometimes help the perovskite dissolve easier. The typical antisolvents could be ACN, Ethanol, DMF, and DMSO.[10-12]

3.2 Characterizations

The morphology of the samples was characterized by a JEOL JSM-6700F field emission scanning electron microscope using 10 kV and 10 µA electron beam. X-ray diffraction patterns (XRD) were recorded by a Bruker D8 Advanced diffractometer with CuKα radiation (Average wavelength λ = 1.54184 Å).

The absorbance of the high transparent PEPC single crystal was recorded by UV-Vis-NIR Spectrophotometer Shimadzu UV3600 in integrating-sphere mode.

Fig. 3.2 illustrates the diagram of a photoluminescence measurement system. A 0.45mW continuous-wave He-Cd laser with the wavelength of 442 nm is used as an excited source. The laser beam is periodically interrupted by an optical chopper which is widely used in combination with a lock-in amplifier (Fig. 3.2). The chopper is used to modulate the intensity of the laser beam, and a lock-in amplifier is used to enhance the signal-to-noise ratio. After going through a mirror and lens system, the laser beam is exposed to the sample. A 50 µm slit helps to obtain a monochromatic reflectance light beam. Then, the beam is received by a monochromator. This monochromator allows a wavelength of 750 nm to transmit. A photomultiplier tube changes optical signals to digital signals which are processed by a computer to get the photoluminescence data of the sample.

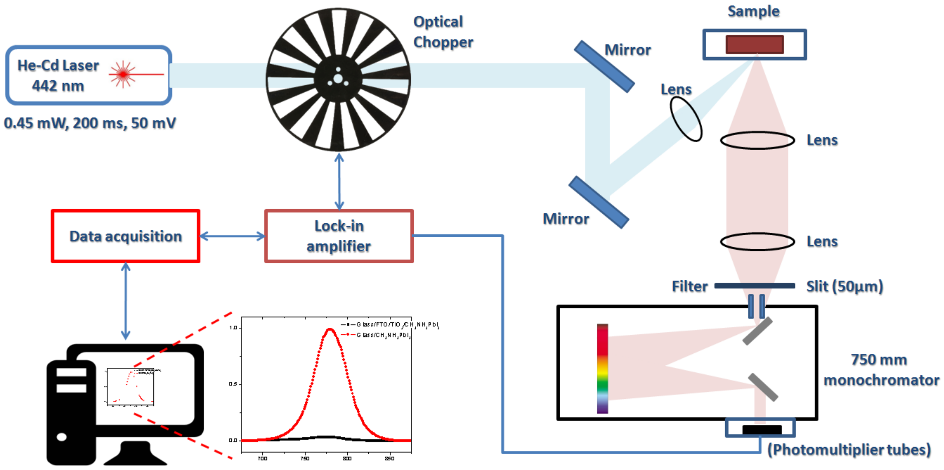

Figure 3.3 Illustration diagram of a photoluminescense measurement system.

X-ray powder diffraction (XRD) patterns were collected using a Bruker-AXS D8 Advance X-ray diffractometer with CuKα (λ=1.54186 Å) in the range 2θ of 10-50^{o} with step size 0.05^{o} and a time setting of 0.5 second per step.

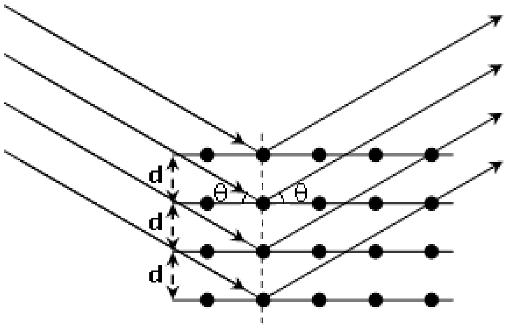

Figure 3.4 Illustration of the XRD diffraction mechanism.

Asylum Research MFP-3D AFM was used for topographic images and piezoelectric measurements of crystals using contact mode and Piezoelectric Force Microscopy (PFM) mode, respectively. Samples for piezoelectric measurements were prepared by using the adhesive tape to peel off layers of PEPC from its as-grown single crystals. Then, silver paste was used to contact the samples with the AFM holder. After 30 min, the tape was removed from the holder and left behind the peeled layers which contacted with holder by a dried silver paste layer. Piezoelectric signal was collected from the top of the samples at various positions, from which piezo-responses depicting the amplitude, phase. The silver paste played the role of bottom electrode for PFM measurements. All measurements were performed using conductive PtIr coated cantilevers (ANSCM-PT, AppNano) with a nominal spring constant of 3 N/m and a resonance frequency of 375 kHz.

Ferroelectric polarization hysteresis was measured by a precision LC ferroelectric tester (Radiant Technologies) loops conducted at room temperature and frequency f = 200 Hz.

Dielectric constant was measured using an LCR metre (Agilent E4980A) over a temperature range from 30 °C to 165 ºC in various frequencies.

Differential scanning calorimetry (DSC) was recorded on a DSC Q10 (TA Instruments) at a rate of 5 ºC/min over a temperature range from 10 °C to 170 ºC under nitrogen (flow rate 50 mL/min).

Thermal gravimetric analysis (TGA) was conducted on a TGA Q500 (TA Instruments) at a rate of 5 ºC/min over a temperature range from 10 °C to 700 ºC under an air flow (flow rate 60 mL/min).

Solubility test: The PEPC powder for the solubility test was obtained by grinding the prepared crystals. The 200 µl vials of DMSO solvent were heated at under stirring while the perovskite powder was added with a small amount of 0.01 g by 0.01 g. Saturation condition was obtained when the perovskite powder did not dissolve completely after 30 mins in the solvent. The process was repeated at various temperatures.

3.3 References

1 Saidaminov, M. I. *et al.* High-quality bulk hybrid perovskite single crystals within minutes by inverse temperature crystallization. *Nature Communications* **6**, 7586, doi:10.1038/ncomms8586 https://www.nature.com/articles/ncomms8586#supplementary-information (2015).

2 Maculan, G. *et al.* CH3NH3PbCl3 Single Crystals: Inverse Temperature Crystallization and Visible-Blind UV-Photodetector. *The Journal of Physical Chemistry Letters* **6**, 3781-3786, doi:10.1021/acs.jpclett.5b01666 (2015).

3 Yangyang, Z. *et al.* Preparation and characterization of high-quality perovskite CH 3 NH 3 PbX 3 (I, Br) single crystal. *IOP Conference Series: Materials Science and Engineering* **167**, 012019 (2017).

4 Dong, Q. *et al.* Electron-hole diffusion lengths > 175 μm in solution-grown CH₃NH₃PbI₃ single crystals. *Science* **347**, 967-970, doi:10.1126/science.aaa5760 (2015).

5 Mitzi, D. B. Synthesis, Crystal Structure, and Optical and Thermal Properties of (C4H9NH3)2MI4 (M = Ge, Sn, Pb). *Chemistry of Materials* **8**, 791-800, doi:10.1021/cm9505097 (1996).

6 Park, G. *et al.* Solvent-dependent self-assembly of two dimensional layered perovskite (C(6)H(5)CH(2)CH(2)NH(3))(2)MCl(4) (M = Cu, Mn) thin films in ambient humidity. *Scientific reports* **8**, 4661, doi:10.1038/s41598-018-23012-2 (2018).

7 Dang, Y., Ju, D., Wang, L. & Tao, X. Recent progress in the synthesis of hybrid halide perovskite single crystals. *CrystEngComm* **18**, 4476-4484, doi:10.1039/C6CE00655H (2016).

8 Chen, Y., He, M., Peng, J., Sun, Y. & Liang, Z. Structure and Growth Control of Organic–Inorganic Halide Perovskites for Optoelectronics: From Polycrystalline Films to Single Crystals. *Advanced Science* **3**, 1500392, doi:doi:10.1002/advs.201500392 (2016).

9 Patel, J. B., Milot, R. L., Wright, A. D., Herz, L. M. & Johnston, M. B. Formation Dynamics of CH3NH3PbI3 Perovskite Following Two-Step Layer Deposition. *The Journal of Physical Chemistry Letters* **7**, 96-102, doi:10.1021/acs.jpclett.5b02495 (2016).

10 Konstantakou, M., Perganti, D., Falaras, P. & Stergiopoulos, T. Anti-Solvent Crystallization Strategies for Highly Efficient Perovskite Solar Cells. *Crystals* **7**, 291 (2017).

11 Paek, S. *et al.* From Nano- to Micrometer Scale: The Role of Antisolvent Treatment on High Performance Perovskite Solar Cells. *Chemistry of Materials* **29**, 3490-3498, doi:10.1021/acs.chemmater.6b05353 (2017).

12 Liu, Y., Yang, Z. & Liu, S. Recent Progress in Single-Crystalline Perovskite Research Including Crystal Preparation, Property Evaluation, and Applications. *Advanced Science* **5**, 1700471, doi:doi:10.1002/advs.201700471 (2018).

Chapter 4

Growth and Ferroelectric Property of Two-dimensional Layered Hybrid Perovskite $(C_6H_5C_2H_4NH_3)_2PbCl_4$ Single Crystals and Ferroelectric Properties

Recently, two-dimensional (2D) layered organic-inorganic perovskites have been a hot topic not only in photovoltaics but also in laser and photo-detection applications due to their remarkable electronic and optical properties. Structurally, these hybrids are suitable for studying of piezoelectricity. However, the piezoelectric measurements of such hybrids have been limited by the internal stress in their substrate interface which leads to the suppression of their piezoelectric performance, and the absence of a fast method for making the single crystals of sufficient size and high quality. Here, we report a facile solvent method in growing the 2D layered $(C_6H_5C_2H_4NH_3)_2PbCl_4$ *(or PEPC) perovskite single crystals. The XRD patterns reveal their high crystalline quality with (400) dominant plane. The ferroelectric properties of their crystals have been found by using the Piezoelectric Force Microscopy (PFM). An effective piezoelectric coefficient of 90 pm* V^{-1}*, a remnant polarization of about 0.85* $\mu C\ cm^{-2}$ *and a coercive field of about 1.5 kV/cm were generated. These results provide a new way to develop new piezoelectric/ferroelectrics and photovoltaics based on 2D layered hybrid perovskite single crystals.*

4.1 Introduction

Organic-inorganic trihalide perovskites have been recently the most promising materials for not only photovoltaics but also lasers, light-emitting diodes, and photodetectors.[1-5] With perovskite structure, these materials have been expected to employ in piezoelectric and ferroelectric applications. However, only a few perovskite components have been reported to ferroelectric behaviours. According to Benedek and co-workers, structural distortions in the perovskite family of materials are the major factor that determines their ferroelectricity.[6] In particular, the cation displacements that accompany the octahedral rotations play a crucial role in suppressing ferroelectricity in these materials. Consequently, the study on ferroelectricity of hybrid trihalide perovskites has been limited to several case reports. By using computational studies including electronic structure, molecular dynamics, and Monte Carlo simulation techniques, Walsh et al. demonstrated the possible formation of ferroelectric domains in the methylammonium-based systems.[7] Additionally, the Coll group introduced a study on ferroelectric properties of methylammonium lead iodide ($MAPbI_3$) perovskite.[8] In this work, $MAPbI_3$ perovskite exhibits a strong increase of piezoelectric response under illumination but does not possess permanent polarization at room temperature.

The film-devices also suffer the internal stress in the interface with substrates (clamping effect) which directly leads to the suppression of their piezoelectric performance. Moreover, the instability and disorder in methylammonium polycrystalline films can obscure the ferroelectric performance of trihalide perovskites. Currently, the perovskite single crystal has been attracted more and more attentions to its remarkable advancement in improving electronic, photovoltaic properties as well as stability.[9] In ferroelectric applications, the crystals can overcome the clamping effect due to its free standing nature. It is demonstrated to greatly improve the stability of perovskite by replacing alkylammonium chains from methylammonium to hydrophobic longer chains such as benzylammonium and phenylethylammonium, which are called two-dimensional perovskites.[10] The Liao group reported the ferroelectricity behaviour of two-dimensional Benzylammonium Lead Chloride $(C_6H_5CH_2NH_3)_2PbCl_4$ single crystals which have a ferroelectric spontaneous polarization of Ps = 13 $\mu C\ cm^{-2}$ and a higher Curie Temperature of Tc = 438 K with a band gap of 3.65 eV. The crystals were synthesized by slow evaporating of a solution at 363 K using N,N-dimethylformamide (DMF) as solvent.[11]

4.2 Single Crystal Growth Process for PEPC

The options of suitable solvents have been a crucial issue that determines the crystal growth process and its quality. For lead trihalide perovskite, the most commonly used solvents are ɣ-butyrolactone (GBL), DMF, and dimethylsulphoxide (DMSO).[12] For PbI_2 and $PbBr_2$ based perovskite crystallizations, GBL and DMF has been widely used, respectively, as these organic solvents can minimize the interactions between the ions during the growth crystal process as well as poor hydrogen bond-forming ability. For $PbCl_2$ based perovskite, DMF can be used as solvent in the crystalline growth.[13,14] However, the precursor solution saturates at very low concentration which leads to low effective crystallization process. Meanwhile, DMSO can well dissolve all PbI_2, $PbBr_2$, and $PbCl_2$ based perovskites. Moreover, the solubility of $PbCl_2$ in DMSO is much higher than that in DMF, which would be beneficial for improving the uniformity of the perovskite films.[15,16] Zhang et. al reported that the solution of $PbCl_2$ based perovskite in DMSO system dramatically improved the film properties resulting in crack-free morphology and enhanced light absorption of the sample, while remaining its crystalline structure.[13] So that, DMSO can be a suitable solvent for PEPC crystallization process.

Recently, anti-solvent vapor –assisted crystallization (AVC) method has been used for the growth of perovskite crystals. In AVC method, an appropriate anti-solvent is slowly diffused into a solution containing the crystal precursors, leading to the growth of crystal.[17] By using AVC method with a solvent as DMF and an anti-solvent as nitromethane, Eijk and the co-authors prepared colourless transparent two-dimensional $(C_6H_5C_2H_4NH_3)_2PbBr_4$, abbreviated $PhEPbBr_4$, perovskite crystals for scintillation applications.[18] The $PhEPbBr_4$ crystals obtained the size of 5 × 6 × 1 mm3 after two months of growth. In addition, regarding to the retrograde solubility behaviour of MA-based perovskites in certain solvents, inverse temperature crystallization (ITC) has been also introduced.[19,20] The ITC method overcomes the time consumption of conventional crystallization methods such as the typical cooling or AVC techniques.[21,22] In the work of the Saidaminov group, the solubility of MAPbI3 and FAPbI3 in GBL, MAPbBr3 in DMF as well as FAPbBr3 in DMF:GBL (1:1 v/v) has been reported. The hybrids exhibited the retrograde solubility behaviours in the corresponding solvents and their single crystals have been prepared using ITC method.[12] However, the solubility of PbCl2 exhibits the increase behaviour in DMSO. Warren and the co-workers reported that in 100% DMSO, the solubility of PbCl2 at 303 K was 0.585 mol/1, and increased significantly to 1.13 mol/l at 318.5 K.[23] For the increasing solubility behaviour component, the facile low-temperature solution growth process can be employed. The low-temperature solution growth is the simplest method for crystallizations of organic crystals for mass production, in which the relative supersaturation is the most significant parameter that affects the growth rate of the crystals.[24]

Herein, we present a facile low-temperature method in growing the 2D layered PEPC single crystals using DMSO as solvent. The PEPC crystals with the band gap of about 3.54 eV have pure phase and high crystallinity as confirmed by XRD data. The phase hysteresis loop and domain regions on single crystal and thin film can be observed by using Piezoelectric Force Microscopy (PFM) measurements. The box-in-box switching test and ferroelectric hysteresis test were also performed to study the ferroelectrics of PEPC material.

4.3 Structure Characterizations

Figure 4.1 shows the growth process of PEPC single crystals. PEPC was prepared by mixing a stoichiometric amount of PbCl2 and 2-Phenylethylamine hydrochloride in DMSO solvent. It is known that the concentration of PbCl2-based solution increases by increasing temperature due to its solubility behaviour. However, the temperature decrease from over 50^{o}C during the filtration step leads to rapid precipitation in the solution which affect the crystallization process of PEPC. We observed that the 1.2 M of well-dissolved solution was obtained by heating the solution at 50^{o}C under stirring. After that, the solution was filtered using PTFE filter with 0.2 µm pore size and replaced in vials. More importantly, the clear solutions were obtained after filtering process. The vials containing clear solutions were kept at room temperature under ambient condition and humidity of around 50%. Small plate-like crystals were obtained after 5 min and mm-size rectangle crystals were formed after 3 h. Figure 4.1a shows the 3 mm × 5 mm rectangle plate-like crystal which were grown after 6 h in DMSO solvent, and Figures 4.1 (b and c) are the photographs of transparent colourless PEPC crystals.

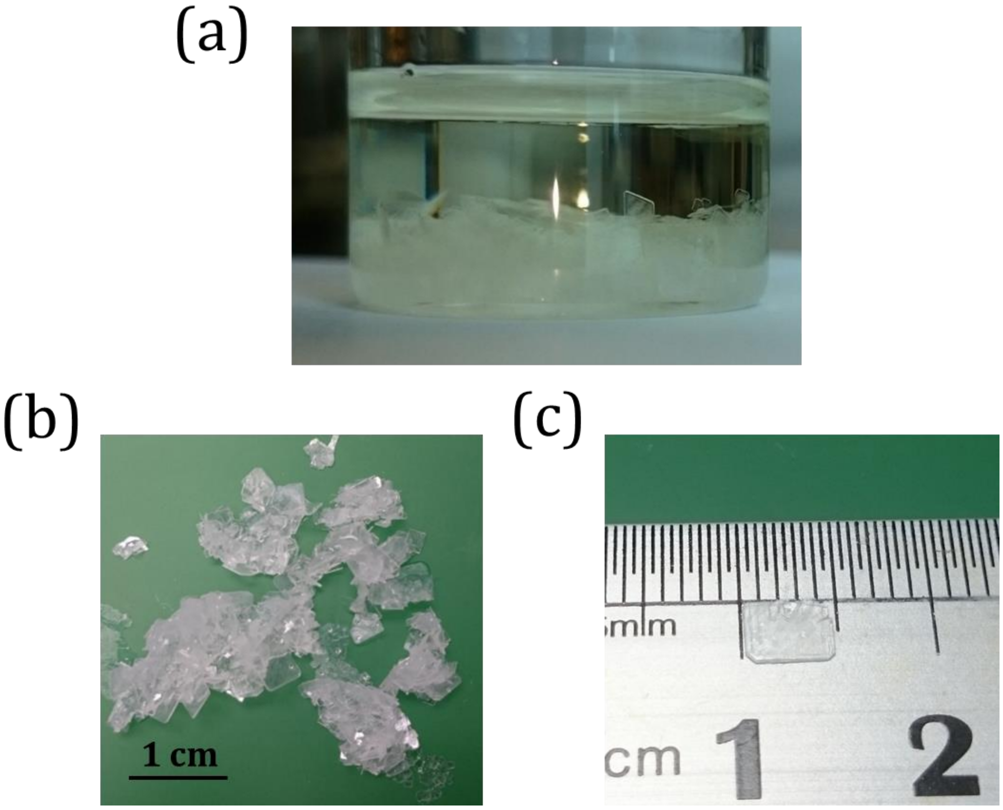

Figure 4.1 Crystal growth process. (a) PEPC rectangle plate-like crystals grown in a vial using DMSO as solvent, (b, c) Photographs of transparent colorless PEPC crystals after 6 h of growth.

We also conduct the solubility test for PEPC single crystals. The PEPC powder for the solubility test was obtained by grinding prepared crystals. 200 µl vials of DMSO solvent were heated at under stirring while the perovskite powder was added with a small amount. The temperature-dependent solubility of PEPC single crystals shows in Figure 4.2. The solubility of PEPC at 50^{o}C was 0.7 ± 0.05 g/ml corresponds to approximately 1.2 M of solution concentration. After 1 month of growth, we obtained centimeter-scale PEPC single crystals (inset image in Fig. 4.5).

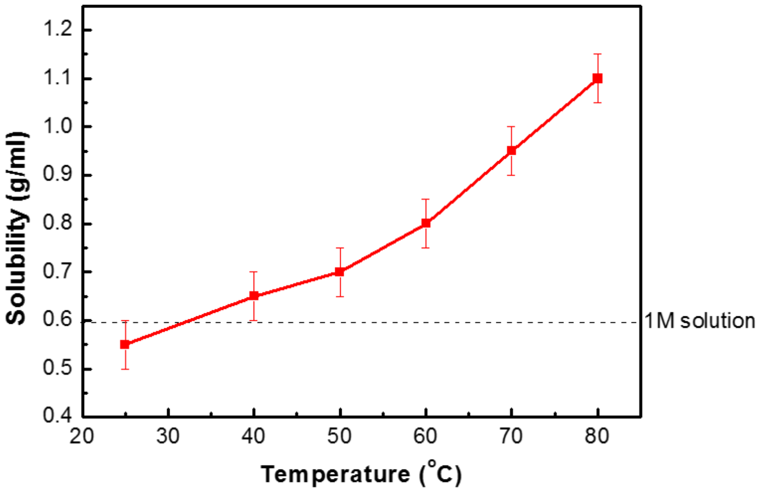

Figure 4.2 Temperature-dependent solubility of PEPC single crystals. The error bars correspond ±0.05 g/ml.

To characterize our as-deposited films, x-ray diffraction (XRD) with Cu Kα radiation was employed to determine the crystal structure and phases X-ray diffraction (XRD) was employed to characterize the crystallinity of the as-grown PEPC crystals. Figure 4.3 shows the powder XRD patterns of the PEPC powder grinding from large crystals. The calculated powder XRD (red line in Fig. 4.3) was used for comparison. The consistency in peak positions between the experimental and calculated patterns indicates the pure pattern and phase of as-grown PEPC crystals. Particularly, the dominant peaks in powder PEPC crystals are at 2θ = 10.5 °, 15.9 °, 21.15 °, 26.48 °, 31.94 °, and 37.35 ° corresponding to lattice planes of (400), (600), (800), (10 00), (12 00), and (14 00), respectively. Additionally, the only (n00) (n = 2, 4, 6 …) peaks in XRD pattern of as-grown single crystal, without detecting any impurity phases, can confirm to its high crystallinity.

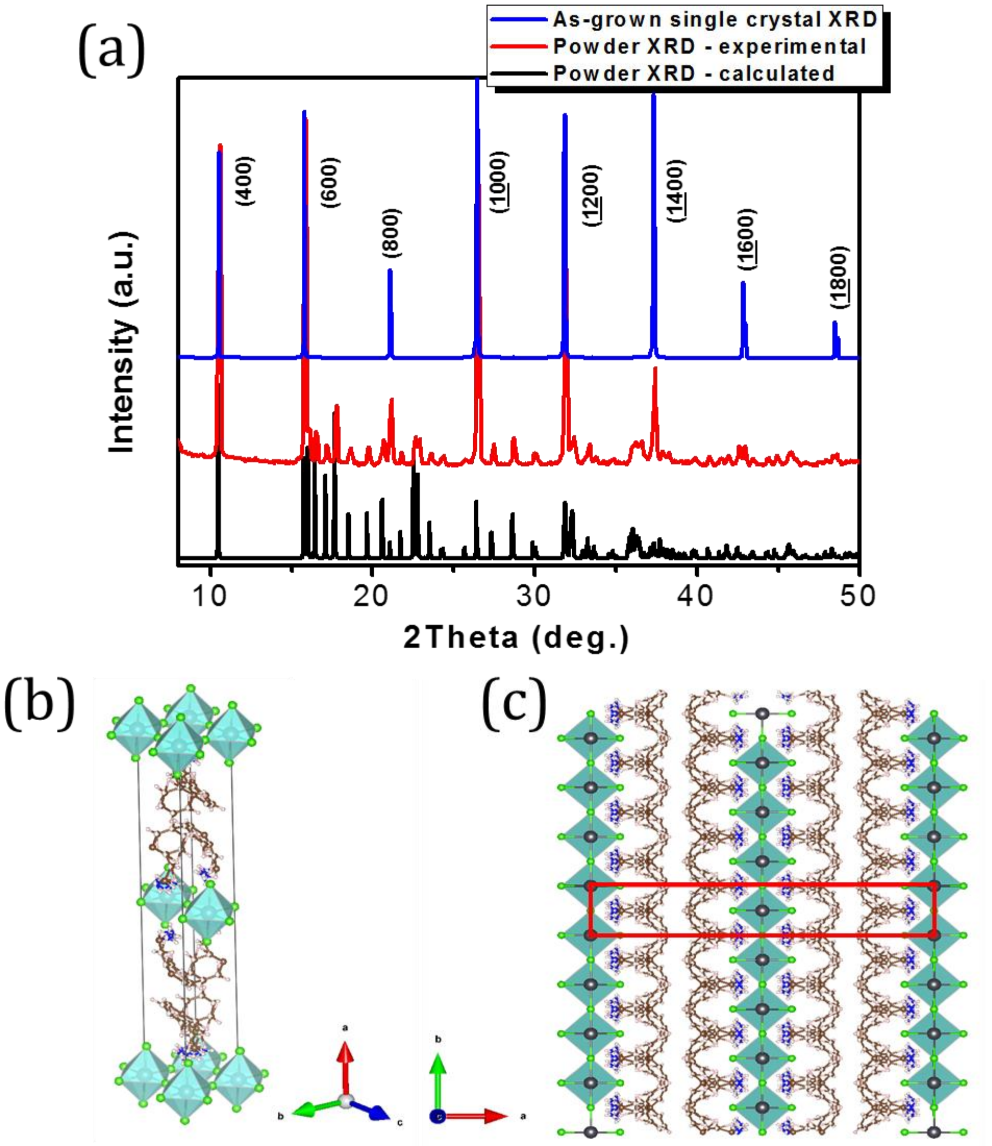

Figure 4.3 Structural properties of PEPC single crystals. (a) XRD patterns recorded on the crystal surface (black) and powder (blue). The red pattern is simulated for the perovskite powder, (b) Sketch of the PEPC perovskite atomic structure of one unit-cell, and (c) layered organic-inorganic structure viewed along c axis and the unit-cell is indicated by a red rectangle. The black balls at the centre of the octahedrons represent the Pb atoms while Cl atoms are displayed in green. The blue and brown symbols represent the phenylethylammonium chains.

Table 4.1: Crystallographic Data for PEPC or $(C_6H_5CH_2CH_2NH_3)_2PbCl_4$.

Chemical Formula	$C_{16}H_{24}Cl_4N_2Pb$
Formula weight, g mol^{-1}	593.39
Wavelength, Å	CuKα (λ=1.5418 Å)
Crystal System	Monoclinic
Lattice type	C
Space group name	C 2/m
Space group number	12
V, $Å^3$	1056.391501
Z	2
Lattice parameters	
a, Å	33.81600
b, Å	5.61210
c, Å	5.57800
α, deg	90.0000
β, deg	93.6900
γ, deg	90.0000

where a, b, c, unit-cell parameters; α, β, γ, unit-cell angles; V, unit-cell volume; Z, number of formula units in the unit cell.

Crystallographic data in Table S2 shows that PEPC belongs to monoclinic crystal system with space group of C 2/m. Unit-cell parameters and angles are a = 33.81600 Å, b = 5.61210 Å, c = 5.57800 Å, and $\alpha = \gamma = 90.00^o$, $\beta = 93.69^o$, respectively. By using unit-cell parameters, we simulated the structure of 2D layered organic-inorganic PEPC perovskite.[25] Figures 4.3 (b and c) depicts the sketch of the PEPC perovskite atomic structure of one unit-cell, and layered organic-inorganic structure viewed along c axis, respectively. The XRD and simulation results can explain for the growth mechanism as well as the layered structure in AFM image of PEPC crystals. The only-peak in XRD pattern of the as-grown PEPC crystal indicates that the crystal is completely occupied by the (400) facet, resulting in the preferable crystal growth along the [400] direction, which is perpendicular to the c-axis.[26] Therefore, the thickness of one unit-cell layer equals to the value of the c parameter or 5.57800 Å. As a result, about 18 unit-cells are evaluated for one 10 nm thick layer in AFM image.

The paraelectric-ferroelectric phase transitions in classic oxide perovskite ferroelectrics $BaTiO_3$, $PbTiO_3$ and $BiFeO_3$ are generally driven by off centring of a 'lone-pair cation' or an octahedral 'd0 cation' through the second-order Jahn–Teller effect. However, a new mechanism of hexagonal $YMnO_3$ was theoretically reported by the Spaldin group in 2004, which is so-called "geometric ferroelectricity".[27] Another ferroelectric mechanism should be "hybrid improper ferroelectricity - HIF" which was introduced by Benedek and Fennie in 2011 for the layered $Ca_3Mn_2O_7$ perovskite.[28] The hybrid improper ferroelectricity requires coupling of two distinct non-polar modes to produce a net polar symmetry. These later two mechanisms are typically driven by purely geometric effects. Particularly, the ferroelectricity arises from the tilting of MnO_5 polyhedra in the case of $YMnO_3$, and octahedral rotations and/or cation ordering in the more general case of $Ca_3Mn_2O_7$ perovskite.

Unlike in the case of 3-D perovskites, where the octahedral tilts centrosymmetrically, the 2-D layered perovskites (i.e., PEPC, PECC) consist of octahedral tilting and twisting in the structure which can naturally give rise to a polarization (Fig. 4.4).

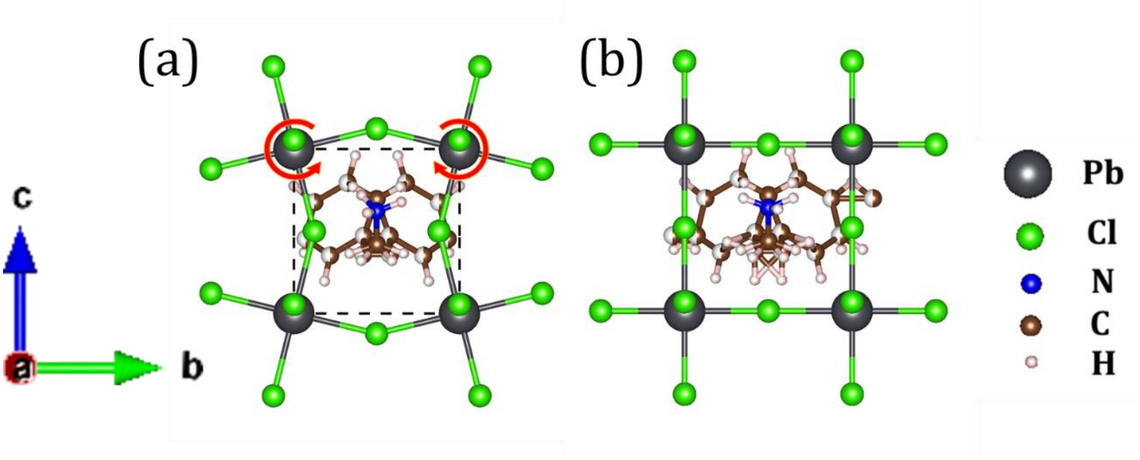

Figure 4.4 The tilting and twisting of $PbCl_6$ octahedra in the 2-D PEPC perovskite structure (a) under T_C temperature, the structure is anisotropic where b-axis polarity arises as a natural consequence of the 'in-phase' tilting around the a-axis, and (b) above T_C temperature, the lattice is symmetric with no octahedral tilting.

The Curie Temperatures, Crystal Structures, and Ferroelectric Types of Typical Ferroelectric materials are shown in Table 1.

Table 4.2: Curie Temperature, Crystal Structure, and Ferroelectric Type of Typical Ferroelectric materials.

Material	**T_C (°C)**	**Crystal Structure**	**Ferroelectric Type**
$Pb(Zr,Ti)O_3$	200	Tetragonal	lone pair
$BaTiO_3$	130[29]	Tetragonal	lone pair
$PbTiO_3$	470[30]	Tetragonal	lone pair
$BiFeO_3$	820[31]	Rhombohedral	lone pair
$Ca_3Mn_2O_7$	220-320[2]	Tetragonal	HIF
$YMnO_3$	1000[28,32]	Hexagonal[33]	geometric
$(Benzylammonium)_2PbCl_4$	165[11]	Orthorhombic	geometric
PEPC (This work)	150	Monoclinic	geometric

4.4 AFM Topography of the Crystal Surface

The topography of as-grown PEPC single crystals was performed using Atomic Force Microscope (AFM MFP-3D, Asylum Research). A topographical image of 50 × 50 μm^2 surface area of as-grown PEPC single crystal is shown in Figure 4.4a. We observed layered structure of the crystal surface with a surface root mean square (RMS) roughness of about 4.6 nm (see Table 4.3). Figure 4.5b shows the cross section of crystal surface along the red line in Figure 4.5a which indicates that the thickness of each layer equals to about 10 nm.

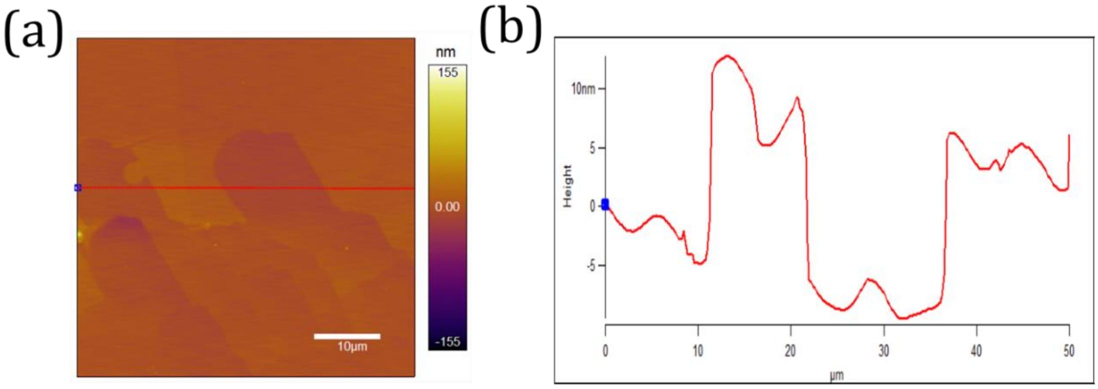

Figure 4.5 (a) AFM topographical image of the as-grown PEPC single crystal surface, and (b) Cross section along the red line in (a).

Table 4.3: Roughness Data of the as-grown PEPC single crystal from Fig. 4.4a.

Parameter	**Full Image Values:**
Standard Deviation, nm	4.572
Max, nm	81.325
Min, nm	-28.384
RMS, nm	**4.572**
Average Deviation, nm	3.260
Skew	0.563
Kurtosis	12
Surface Area, μm²	2500

4.5 Optical and Photonic Properties

The photoluminescence and UV-vis spectra of the layered PEPC single crystal are shown in Figure 3 and Figure 4.6, respectively. The UV-vis spectra confirms their absorption maximum peak at approximately 338 nm,[34] which is ascribed to the exciton absorption of the layered perovskite lying at the red side of the continuum absorption due to inter-band transition.

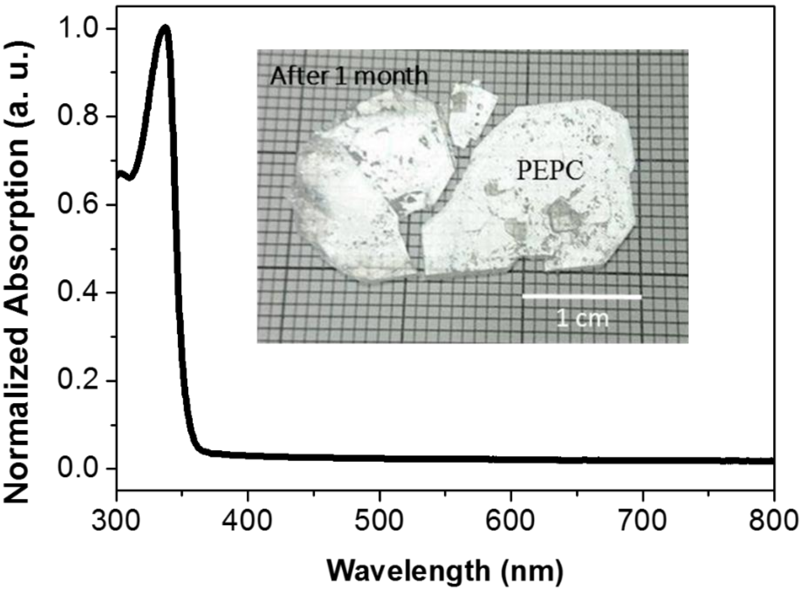

Figure 4.6 Ultraviolet-vis absorption spectra of single crystals. of the 310 - 800 nm range showing the absorption maximum peak at 338 nm. Inset: Photograph of PEPC single crystals after 1 month of growth.

Contrast to the observed sharp excitonic absorption peak, the PEPC single crystal shows a strong broad band white light emission centered at around 500 – 600 nm, with negligible band edge emission detected. The white light emission of a variety of 2D perovskites has been discovered and well-studied, which is generally attributed to the consequence of strong exciton-lattice coupling in the 2D perovskite system, namely self-trapped exciton emission. Due to the highly-distorted lattice with respect to the ground state by strong exciton-phonon coupling, the self-trapped exciton emission can be very broad and featureless in contrast with free excitons. [35-37] The negligible free exciton emission indicates the self-trapping of the free excitons should be ultrafast and barrierless.[37] Fitting the temperature-dependent PL intensity in Figure 4.7b yields thermal activation energy of around 116 meV, implying the strong 'trapping' of the excitons due to local potential/defects and/or large exciton binding energy due to multi-quantum-well structure of 2D perovskites.[38] Consistent with the PL intensity results, the self-trapped excitons have a lifetime of around 4.5 ns at room temperature, which drastically increased by 3 orders to around 1.5 μs at 77 K (Figs 4.7c,d). This indicates the high stabilization of these self-trapped excitons under low temperature.

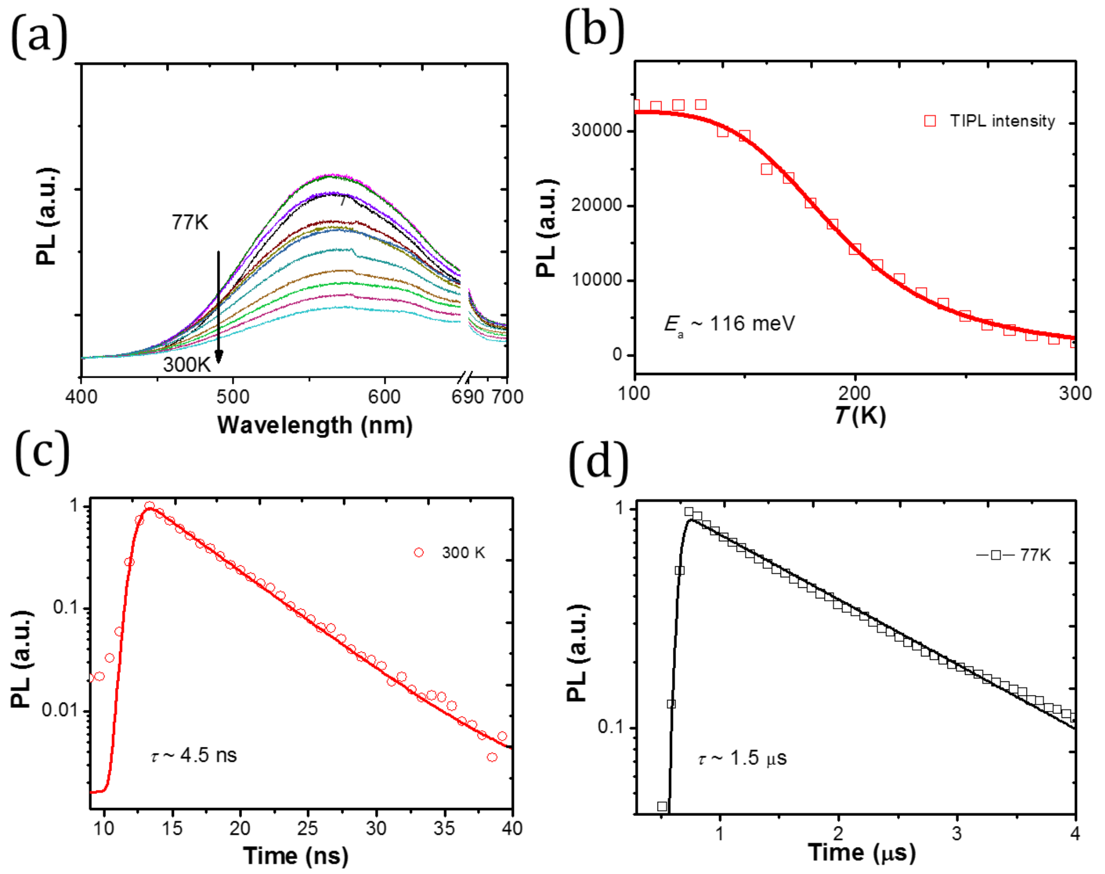

Figure 4.7 Optical properties of PEPC single crystals. (a) The PL spectra of the PEPC SC with different temperatures. (b) The temperature-dependent PL intensity. (c-d) The time-resolved PL at 300 K and 77 K, respectively. All measurements were performed with 340 nm excitation.

4.6 Piezoelectric Force Microscopy Characterizations

Piezoelectric Force Microscopy (PFM) measurement with a maximum bias voltage of ±10 V was employed to investigate the piezoelectric properties at room temperature of the PEPC crystals. Figure 4.8a shows the schematic diagram of the measurement set-up. All measurements were performed using conductive PtIr coated cantilevers (ANSCM-PT, AppNano) with a resonance frequency of 375 kHz. For undertaking the suitably strong applied electric field through the single crystal, we used the adhesive tape to peel off layers of PEPC from the as-grown single crystal. The piezoelectric measurements were conducted on thin layered crystal surface. Silver paste was used to contact the peeled sample with the sample holder and played the role of bottom electrode. Piezoelectric signal was recorded from the top of the samples at various positions, from which piezo-responses depicting the amplitude and phase as a function of bias voltage.

The phase signals in Figure 4.8b exhibits a ∼180° reproducible hysteresis loop which indicates that the downward polarization obtains under the application of a negative poling voltage and becomes upward when the poling voltage exceeds the coercive bias voltage. The coercive voltage of ∼0.85 V was evaluated using the equation $(V_C^+ - V_C^-)/2$, where V_C^+ and V_C^- are the forward and reverse coercive bias voltages.[39] For the peeled single crystal with thickness of 5 µm (Fig. 4.8d), the coercive field is estimated of about 1.7 kV cm^{-1}, which is much smaller than those of some typical ferroelectric materials like PVDF (500 kV cm^{-1})[40], BTO (10 kV cm^{-1})[41], PZT (20 to 80 kV cm^{-1})[42], DIPAC (9 kV cm^{-1})[43], and α-DIPAB (5.0 kV cm^{-1}).[44] The shift toward positive bias voltage of the hysteresis loop is relative to the difference in work functions of two electrodes: 5.6 eV for PtIr and 4.6 eV for silver paste.[45,46] The amplitude (blue curve in Fig. 4.8c) shows the displacement of the AFM tip caused by the deformation of the sample under the bias voltage resulted in a butterfly-like curve, suggesting the switching of the ferroelectric domains.

The value of piezoelectric coefficient d_{33} can be calculated from the amplitude curve through the following equation:[47,48]

$$d_{33} = \frac{D - D_I}{V - V_I} \qquad (4.1)$$

where D is the measured value of piezoelectric deformation, V is the applied voltage, while D_I, V_I are the piezoelectric deformation and applied voltage of the intersection, respectively. The black curve in Figure 4.8c shows the piezoelectric coefficient curve d_{33} of PEPC samples which is calculated using equation (4.1). It indicates that the maximum value of 90 pm V^{-1} of d_{33} can be obtained. This piezoelectric coefficient d_{33} value of PEPC single crystal is comparable to other typical ferroelectric materials like

$PbTiO_3$ (65 pm V^{-1})[49], $PbZr_{0.2}Ti_{0.8}O_3$ bulk crystal (87 pm V^{-1})[50], $BaTiO_3$ thin film (40 pm V^{-1}) [51], PVDF (25.49 - 49.61 pm V^{-1}) [52], and PVDF/GO nanofibers (-93.75 pm V^{-1}).[53]

Single frequency PFM mode (AFM MFP-3D, Asylum Research) was employed under a 1.0 V AC drive amplitude voltage to investigate for imaging the piezo-response of PEPC samples. The phase image depicts two domain regions with a clear 180° contrast (Fig. 4.8f) which are accordingly presented in the amplitude image (Fig. 4.8e). This domain area is irrelevant to its topography (Fig. 4.8d). Particularly, the bright and dark regions in the phase image exhibit the piezo active areas where the bright areas corresponding to the positive and the dark areas corresponding to the negative orientation.

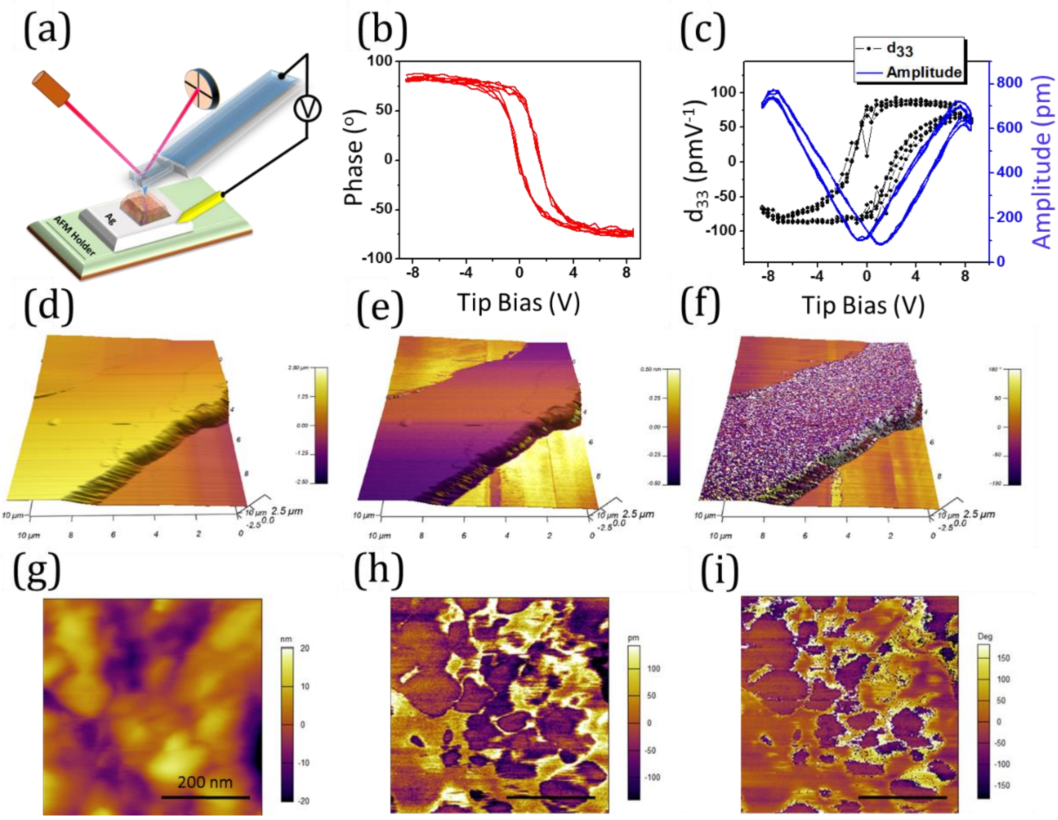

Figure 4.8 Piezoelectric effect of PEPC single crystals. (a) Schematic diagram of the piezoelectric measurement set-up for the single crystals. (b) Phase hysteresis loops measured on the crystal surface under application of tip bias voltage, (c) Amplitude signal (blue curve), and piezoelectric coefficient d_{33} (black curve). (d-f) Topography of

the peeled PEPC single crystals, and its corresponding amplitude and phase response images, respectively. (g-i) Topographical image of the peeled PEPC thin film sample, and its corresponding amplitude and phase response images, respectively.

The domain structural images for the PEPC thin film sample are shown in Figures 4.8g-i. The domains of thin film are smaller than that in single crystal due to its poly-crystallization. The phase PFM images of the thin film sample also reveal the two polarization domain regions with 180^o contrast. Figure 4.8b shows the dependence of phase and amplitude of the thin film sample with bias voltage which displays a 180^o hysteresis loop and a butterfly curve, respectively. As indicated in the smaller phase hysteresis loop, the local coercive field of the thin film is smaller than that of the single crystal.

However, even though 180^o hysteresis loops have been obtained in both PEPC single crystal and thin film samples, it does not warrant the switchable polarization under the electric field.[54] Therefore, the local switching test to confirm the switchable ability was performed by applying the box-in-box bias between the conductive PFM tip.

4.7 Box-in-box Switching Testing

Firstly, the PFM measurement was carried out over an initial area, whose topography, amplitude and phase signals are shown in Figures 4.9a, c, g, respectively. Then a selected region of $5 \times 5\ \mu m^2$ was polarized using an +9 V bias applied to the PFM tip. The brighter box in the center of Figures 4.9d, h indicates that the polarization was oriented upward. After that, an area of $2.5 \times 2.5\ \mu m^2$ inside the bigger box was scanned using an opposite bias of -9 V, the polarization orientation of this box-in-box region was switched downward as shown in Figures 4.9e, i.

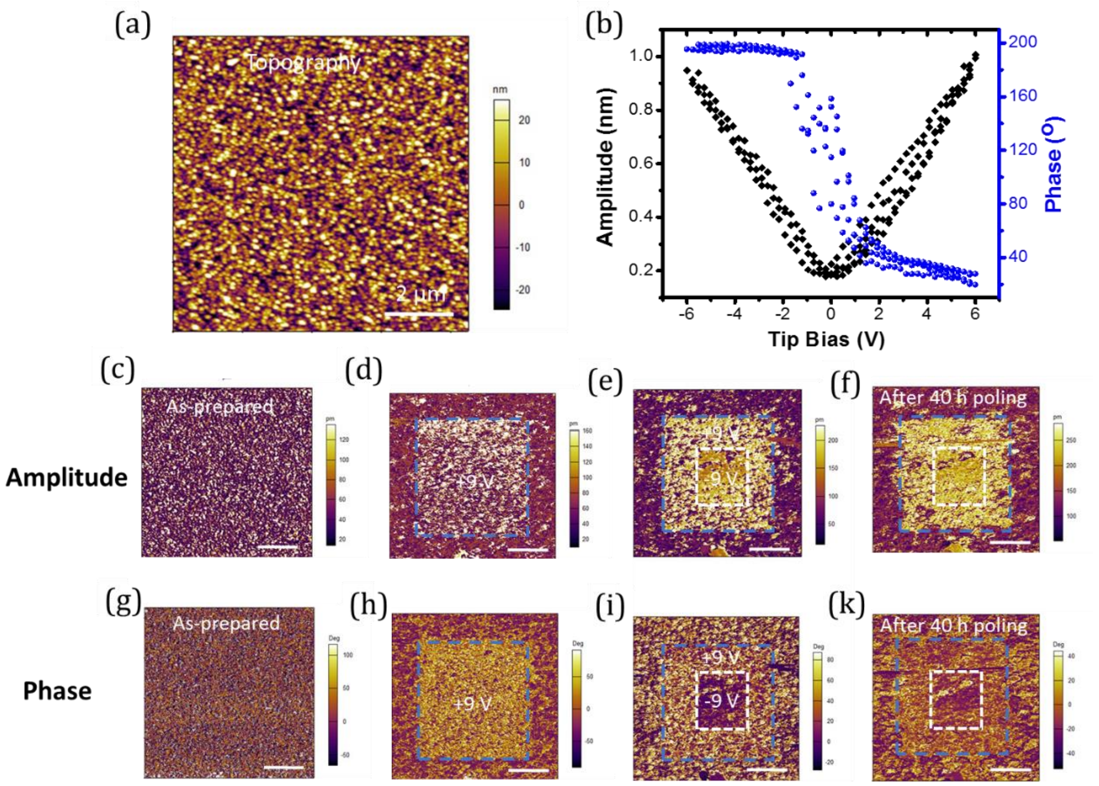

Figure 4.9 Box-in-box switching measurement of PEPC on the PEPC thin film sample. (a) Topography of the as-prepared thin film. (b) Phase and amplitude curve employed on the as-prepared thin film. (c-f) Amplitude images of (c) as-prepared sample, (d) after writing polarization “upward” by applying a box of +9V bias, (e) after switching polarization “downward” by applying a box-in-box of -9V bias. And (g-k) their corresponding phase images, respectively. The scale bar is 2 µm.

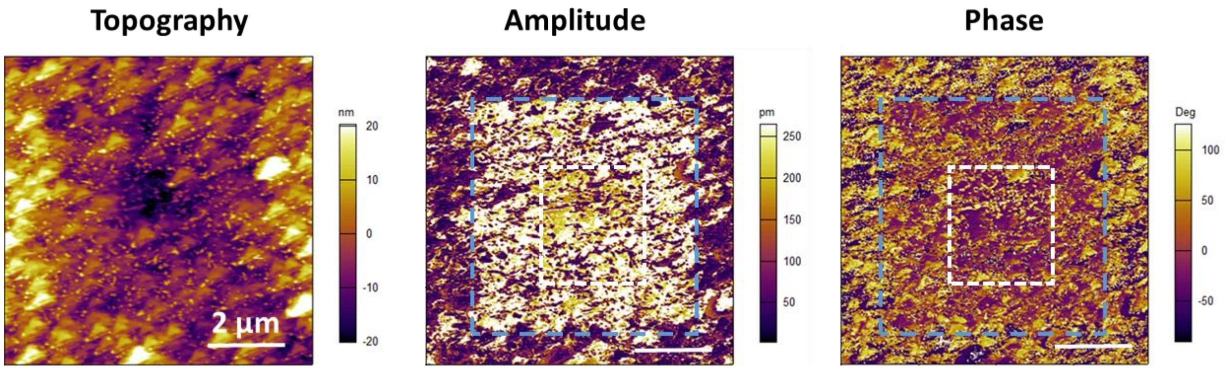

Figure 4.10. The box-in-box switching area after 20 days.

After 40 h poling, the downward polarization area in the small box became disappeared, resulted to the blurred colour region in Figures 4.9f, k, while the upward polarization area remained, even after 20 days (Fig. 4.10). The gradual loss of downward polarization can be attributed to the presence of substrate-induced strains and internal bias in the PEPC thin film.[55]

4.8 Phase Transition Behaviours

We measured the ferroelectric hysteresis loop for the PEPC single crystal at frequency 200 Hz and room temperature. As shown in Figure 4.12a, a typical ferroelectric hysteresis loop is observed in the polarization vs. electric field (P-E) curves of PEPC single crystal. In some cases, the lossy dielectrics could also provide a hysteresis loop for a dielectric material in the procedure of electrical hysteresis measurements. However, these kinds of the hysteresis loops are accompanied with higher leakage currents since the dielectric loss is proportional to conductivity.[56] In our ferroelectric hysteresis loop measurements for PEPC single crystal, extremely low leakage currents (about 10^{-8} A cm^{-2}) were obtained (Fig. 4.11). These results demonstrate the observed hysteresis loops in P-E measurements of PEPC single crystal are due to its ferroelectricity.

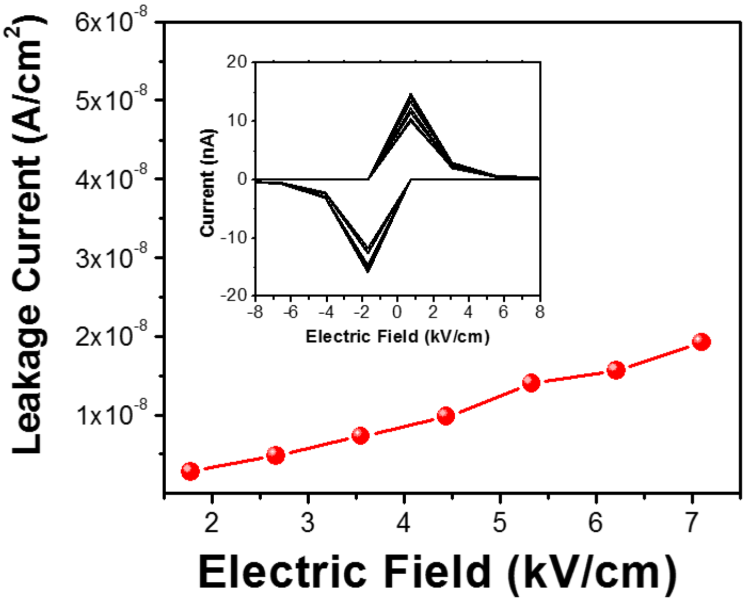

Figure 4.11 Leakage current vs. electric field for PEPC single crystal. Inset: Current response as a function of electric field, measured by Conducting-AFM. Inset: current peaks in the curves.

The P-E hysteresis loop indicates that a remnant polarization, Pr, as large as about 0.85 μC cm^{-2} and a coercive field, Ec, of about 1.5 kV/cm can be obtained after applying an electric field of 3.5 kV/cm. As shown in Figure 4.12b, by increasing of electric field, we can increase the remnant polarization (from 0.85-1.2 μC cm^{-2}) and coercive field (from 1.5-1.8 kV/cm) which is consistent with the estimated value from the PFM phase hysteresis loop of PEPC single crystal.

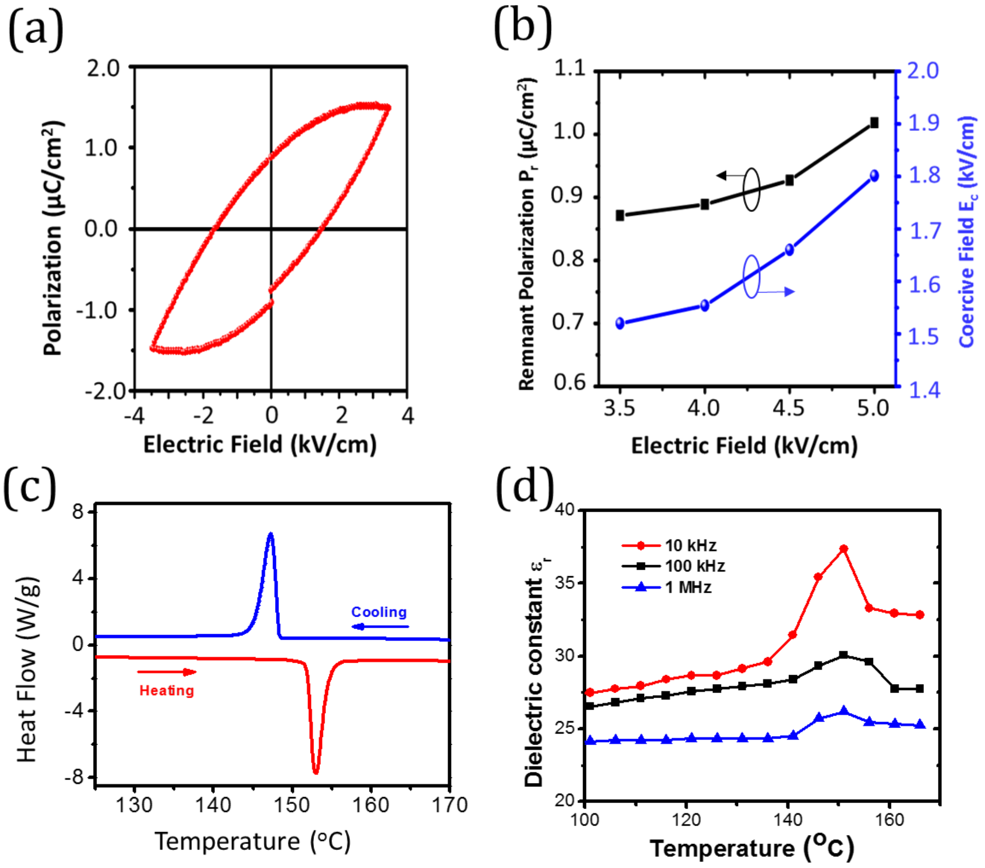

Figure 4.12 Evidences for phase transitions for the PEPC single crystal. (a) Electric polarization (P) versus electric field (E) hysteresis. (b) Changes of Remnant polarization (P_r) and Coercive field (E_C) with applied electric fields. (c) Heating and cooling DSC

curves. (d) Temperature dependences of the real part of dielectric constant ε_r measured at 10 kHz, 100 kHz and 1 MHz, respectively.

4.9 Differential Scan Calorimetry Measurement and Thermal and Moisture Stability

The heating and cooling DSC curves (Fig. 4.12c) show peaks at 153°C and 147.1°C, respectively, which correspond to the phase transition of the PEPC single crystal from ferroelectric (low temperature) to paraelectric (high temperature). The Curie temperature T_c = 150 °C can be calculated from the DSC results. The dielectric constant as a function of the temperature in the frequencies of 10 kHz, 100 kHz and 1 MHz is presented in Figure 4.12d, respectively. As expected, the dielectric constant undergoes a jump with a maximum dielectric constant value at temperature of around 150 °C which reveals a ferroelectric transition, consistent with that in the differential scan calorimetry (DSC) results.

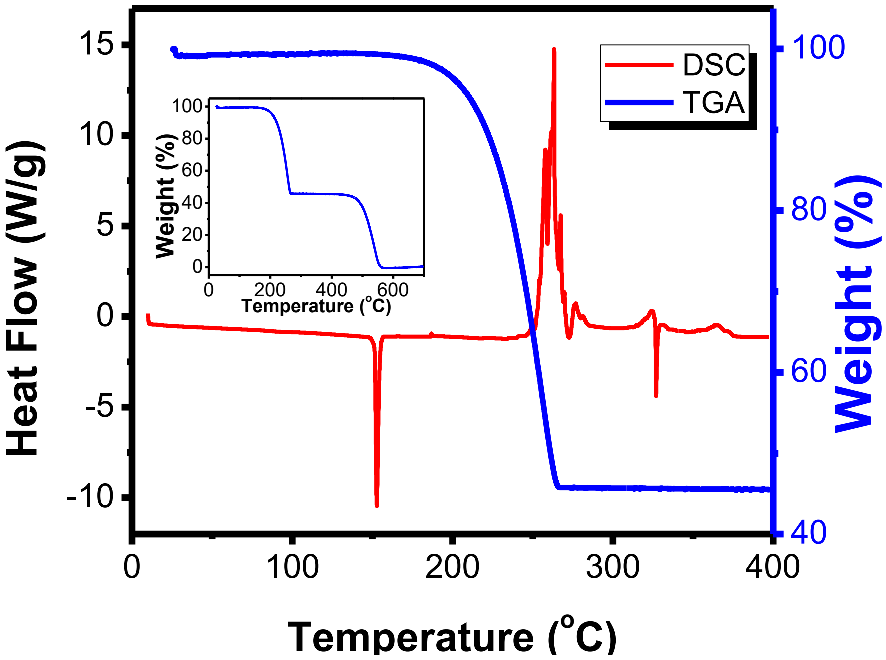

Figure 4.13 TGA and DSC curves of the PEPC single crystal. In set: the TGA from 10^{o}C -700^{o}C.

Figure 4.13 shows TGA and DSC curves of the PEPC single crystal. The decomposition profile proceeds with two steps. The first weight loss, which starts from about 190°C, indicating a major loss of Cl and organic compounds such as HCl and PEA. The DSC peak at 262°C indicating to this decomposition. At higher temperatures, the weight loss is possibly associated with the combustion of $PbCl_2$. The DSC peak located at 153°C corresponding to the phase transition of the PEPC, and the DSC peak at 327°C can be the melting peak of Pb.

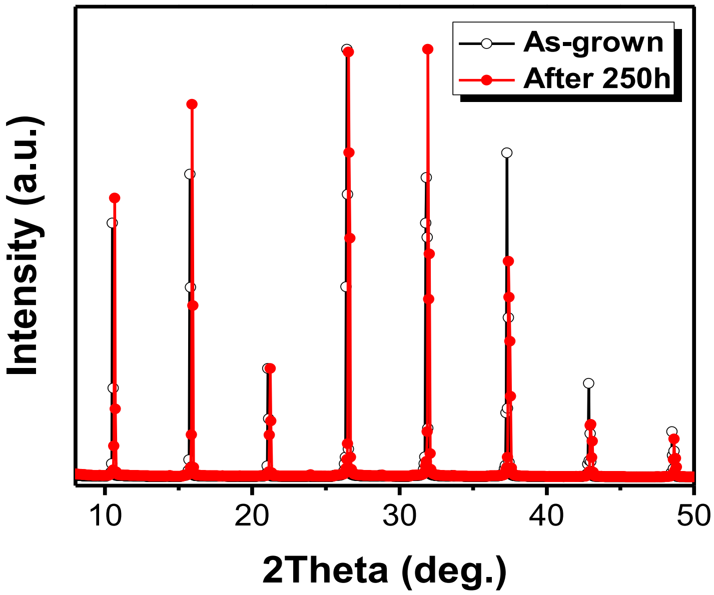

Figure 4.14 XRD patterns of as-grown single crystal (black line) and after 250 h in ambient condition (red line**),** reveal the stability of PEPC single crystal resulting from no new peaks can be detected in XRD pattern.

The stability of PEPC single crystals have been also investigated. Figure 4.14 reveals the stability of PEPC single crystal resulting from no new peaks can be detected in XRD pattern after 250 h.

4.10 Summary

In summary, we have reported a facile solution method to grow the stable PEPC perovskite single crystal. The ferroelectrics of the single crystal were confirmed by PFM, box-in-box local switching testing, and ferroelectric testing. The PEPC crystal can generate a remnant polarization of about 0.85 μC cm^{-2}, a coercive field of about 1.5 kV/cm and an effective piezoelectric coefficient of 90 pm V^{-1}. Our results provide a new way to functionalize a new piezoelectric/ferroelectrics and photovoltaics based on 2D layered hybrid perovskite single crystals.

4.11 References

1 Kojima, A., Teshima, K., Shirai, Y. & Miyasaka, T. Organometal halide perovskites as visible-light sensitizers for photovoltaic cells. *Journal of the American Chemical Society* **131**, 6050-6051 (2009).

2 Burschka, J. *et al.* Sequential deposition as a route to high-performance perovskite-sensitized solar cells. *Nature* **499**, 316-319, doi:10.1038/nature12340 http://www.nature.com/nature/journal/v499/n7458/abs/nature12340.html#supplementary-information (2013).

3 Zhu, H. *et al.* Lead halide perovskite nanowire lasers with low lasing thresholds and high quality factors. *Nature materials* **14**, 636-642, doi:10.1038/nmat4271 http://www.nature.com/nmat/journal/v14/n6/abs/nmat4271.html#supplementary-information (2015).

4 Xing, G. *et al.* Long-Range Balanced Electron- and Hole-Transport Lengths in Organic-Inorganic CH3NH3PbI3. *Science* **342**, 344-347, doi:10.1126/science.1243167 (2013).

5 Yakunin, S. *et al.* Detection of X-ray photons by solution-processed lead halide perovskites. *Nat Photon* **9**, 444-449, doi:10.1038/nphoton.2015.82 http://www.nature.com/nphoton/journal/v9/n7/abs/nphoton.2015.82.html#supplementary-information (2015).

6 Benedek, N. A. & Fennie, C. J. Why Are There So Few Perovskite Ferroelectrics? *The Journal of Physical Chemistry C* **117**, 13339-13349, doi:10.1021/jp402046t (2013).

7 Walsh, A. Principles of Chemical Bonding and Band Gap Engineering in Hybrid Organic–Inorganic Halide Perovskites. *The Journal of Physical Chemistry C* **119**, 5755-5760, doi:10.1021/jp512420b (2015).

8 Coll, M. *et al.* Polarization Switching and Light-Enhanced Piezoelectricity in Lead Halide Perovskites. *The Journal of Physical Chemistry Letters* **6**, 1408-1413, doi:10.1021/acs.jpclett.5b00502 (2015).

9 Nie, W. *et al.* High-efficiency solution-processed perovskite solar cells with millimeter-scale grains. *Science* **347**, 522-525, doi:10.1126/science.aaa0472 (2015).

10 Tiep, N. H., Ku, Z. & Fan, H. J. Recent Advances in Improving the Stability of Perovskite Solar Cells. *Adv Energy Mater* **6**, 1501420-n/a, doi:10.1002/aenm.201501420 (2016).

11 Liao, W.-Q. *et al.* A lead-halide perovskite molecular ferroelectric semiconductor. *Nature Communications* **6**, 7338, doi:10.1038/ncomms8338

https://www.nature.com/articles/ncomms8338#supplementary-information (2015).

12 Saidaminov, M. I., Abdelhady, A. L., Maculan, G. & Bakr, O. M. Retrograde solubility of formamidinium and methylammonium lead halide perovskites enabling rapid single crystal growth. *Chemical communications* **51**, 17658-17661, doi:10.1039/C5CC06916E (2015).

13 Zhang, Z. *et al.* DMSO-based PbI2 precursor with PbCl2 additive for highly efficient perovskite solar cells fabricated at low temperature. *Rsc Adv* **5**, 104606-104611, doi:10.1039/C5RA25160E (2015).

14 Zhang, S. *et al.* Synthesis and optical properties of novel organic-inorganic hybrid UV (R-NH3)2PbCl4 semiconductors. *Journal of Materials Chemistry* **21**, 466-474, doi:10.1039/C0JM02121K (2011).

15 Wu, Y. *et al.* Retarding the crystallization of PbI2 for highly reproducible planar-structured perovskite solar cells via sequential deposition. *Energ Environ Sci* **7**, 2934-2938, doi:10.1039/C4EE01624F (2014).

16 Jeon, N. J. *et al.* Solvent engineering for high-performance inorganic–organic hybrid perovskite solar cells. *Nature materials* **13**, 897-903, doi:10.1038/nmat4014

http://www.nature.com/nmat/journal/v13/n9/abs/nmat4014.html#supplementary-information (2014).

17 Fang, Y., Dong, Q., Shao, Y., Yuan, Y. & Huang, J. Highly narrowband perovskite single-crystal photodetectors enabled by surface-charge recombination. *Nat Photon* **9**, 679-686, doi:10.1038/nphoton.2015.156

http://www.nature.com/nphoton/journal/v9/n10/abs/nphoton.2015.156.html#supplementary-information (2015).

18 Eijk, C. W. E. v. *et al.* in *2008 IEEE Nuclear Science Symposium Conference Record.* 3525-3528.

19 Ku, Z. *et al.* Solvent engineering for fast growth of centimetric high-quality CH3NH3PbI3 perovskite single crystals. *New Journal of Chemistry* **40**, 7261-7264, doi:10.1039/C6NJ00188B (2016).

20 Saidaminov, M. I. *et al.* High-quality bulk hybrid perovskite single crystals within minutes by inverse temperature crystallization. *Nature communications* **6**, doi:10.1038/ncomms8586 (2015).

21 Maculan, G. *et al.* CH3NH3PbCl3 Single Crystals: Inverse Temperature Crystallization and Visible-Blind UV-Photodetector. *The Journal of Physical Chemistry Letters* **6**, 3781-3786 (2015).

22 Dong, Q. *et al.* Electron-hole diffusion lengths> 175 μm in solution-grown CH3NH3PbI3 single crystals. *Science* **347**, 967-970 (2015).

23 Warren, G. W. & Henein, H. Solubility of PbCl2 in DMSO and DMSO—water solutions. *Hydrometallurgy* **46**, 243-247, doi:http://dx.doi.org/10.1016/S0304-386X(97)00011-X (1997).

24 Zaitseva, N. *et al.* Application of solution techniques for rapid growth of organic crystals. *Journal of Crystal Growth* **314**, 163-170, doi:http://dx.doi.org/10.1016/j.jcrysgro.2010.10.139 (2011).

25 Momma, K. & Izumi, F. VESTA 3 for three-dimensional visualization of crystal, volumetric and morphology data. *Journal of Applied Crystallography* **44**, 1272-1276, doi:doi:10.1107/S0021889811038970 (2011).

26 Wang, J., Zhang, G., Yu, H., Wang, Y. & Chen, C. in *Handbook of Crystal Growth (Second Edition)* 169-208 (Elsevier, 2015).

27 Van Aken, B. B., Palstra, T. T. M., Filippetti, A. & Spaldin, N. A. The origin of ferroelectricity in magnetoelectric YMnO3. *Nature Materials* **3**, 164, doi:10.1038/nmat1080 (2004).

28 Benedek, N. A. & Fennie, C. J. Hybrid Improper Ferroelectricity: A Mechanism for Controllable Polarization-Magnetization Coupling. *Physical Review Letters* **106**, 107204, doi:10.1103/PhysRevLett.106.107204 (2011).

29 Shieh, J., Yeh, J. H., Shu, Y. C. & Yen, J. H. Hysteresis behaviors of barium titanate single crystals based on the operation of multiple 90° switching systems. *Materials Science and Engineering: B* **161**, 50-54, doi:https://doi.org/10.1016/j.mseb.2008.11.046 (2009).

30 in *Ternary Compounds, Organic Semiconductors* (eds O. Madelung, U. Rössler, & M. Schulz) 1-7 (Springer Berlin Heidelberg, 2000).

31 Bensaid, D., Benkhettou, N.-E. & Kourdassi, A. Structural and Electronic Properties of Bixo<sub>3</sub> (X = Mn, Fe, Cr). *Journal of Modern Physics* **Vol.02No.07**, 9, doi:10.4236/jmp.2011.27075 (2011).

32 Łukaszewicz, K. & Karut-Kalicińska, J. X-Ray investigations of the crystal structure and phase transitions of YMnO3. *Ferroelectrics* **7**, 81-82, doi:10.1080/00150197408237954 (1974).

33 Howard, C. J., Campbell, B. J., Stokes, H. T., Carpenter, M. A. & Thomson, R. I. Crystal and magnetic structures of hexagonal YMnO3. *Acta Crystallographica Section B* **69**, 534-540, doi:doi:10.1107/S205251921302993X (2013).

34 Jemli, K. *et al.* Two-Dimensional Perovskite Activation with an Organic Luminophore. *ACS applied materials & interfaces* **7**, 21763-21769, doi:10.1021/acsami.5b05279 (2015).

35 Dohner, E. R., Hoke, E. T. & Karunadasa, H. I. Self-Assembly of Broadband White-Light Emitters. *Journal of the American Chemical Society* **136**, 1718-1721, doi:10.1021/ja411045r (2014).

36 Dohner, E. R., Jaffe, A., Bradshaw, L. R. & Karunadasa, H. I. Intrinsic White-Light Emission from Layered Hybrid Perovskites. *Journal of the American Chemical Society* **136**, 13154-13157, doi:10.1021/ja507086b (2014).

37 Hu, T. *et al.* Mechanism for Broadband White-Light Emission from Two-Dimensional (110) Hybrid Perovskites. *Journal of Physical Chemistry Letters* **7**, 2258-2263, doi:10.1021/acs.jpclett.6b00793 (2016).

38 Tanaka, K. *et al.* Electronic and excitonic structures of inorganic-organic perovskite-type quantum-well crystal (C4H9NH3)(2)PbBr4. *Jpn J Appl Phys 1* **44**, 5923-5932, doi:10.1143/Jjap.44.5923 (2005).

39 Bharathi, P., Thomas, P. & Varma, K. B. R. Piezoelectric properties of individual nanocrystallites of Ba0.85Ca0.15Zr0.1Ti0.9O3 obtained by oxalate precursor route. *Journal of Materials Chemistry C* **3**, 4762-4770, doi:10.1039/C5TC00530B (2015).

40 Horiuchi, S. *et al.* Quantum ferroelectricity in charge-transfer complex crystals. *Nature communications* **6**, 7469, doi:10.1038/ncomms8469

http://www.nature.com/articles/ncomms8469#supplementary-information (2015).

41 Horiuchi, S. & Tokura, Y. Organic ferroelectrics. *Nature materials* **7**, 357-366 (2008).

42 Foster, C. M. *et al.* Single-crystal Pb(ZrxTi1−x)O3 thin films prepared by metal-organic chemical vapor deposition: Systematic compositional variation of

electronic and optical properties. *Journal of Applied Physics* **81**, 2349-2357, doi:10.1063/1.364239 (1997).

43 Fu, D.-W. *et al.* Diisopropylammonium Chloride: A Ferroelectric Organic Salt with a High Phase Transition Temperature and Practical Utilization Level of Spontaneous Polarization. *Advanced materials* **23**, 5658-5662, doi:10.1002/adma.201102938 (2011).

44 Fu, D.-W. *et al.* Diisopropylammonium Bromide Is a High-Temperature Molecular Ferroelectric Crystal. *Science* **339**, 425-428, doi:10.1126/science.1229675 (2013).

45 Jalalian, A., Grishin, A. M., Wang, X. L., Cheng, Z. X. & Dou, S. X. Large piezoelectric coefficient and ferroelectric nanodomain switching in Ba(Ti0.80Zr0.20)O3-0.5(Ba0.70Ca0.30)TiO3 nanofibers and thin films. *Appl Phys Lett* **104**, 103112, doi:doi:http://dx.doi.org/10.1063/1.4867013 (2014).

46 Weeber, A. *et al.* Proceedings of the 4th International Conference on Crystalline Silicon Photovoltaics (SiliconPV 2014)2D-modelling of Metal-Si Emitter Interface Assuming Schottky or Ohmic Contact. *Energy Procedia* **55**, 107-114, doi:http://dx.doi.org/10.1016/j.egypro.2014.08.088 (2014).

47 Kholkin, A. L., Wütchrich, C., Taylor, D. V. & Setter, N. Interferometric measurements of electric field-induced displacements in piezoelectric thin films. *Review of Scientific Instruments* **67**, 1935-1941, doi:doi:http://dx.doi.org/10.1063/1.1147000 (1996).

48 Chen, Z. *et al.* Piezoelectric properties of rhombic LiNbO3 nanowires. *Rsc Adv* **2**, 7380-7383, doi:10.1039/C2RA20237A (2012).

49 Kighelman, Z., Damjanovic, D., Cantoni, M. & Setter, N. Properties of ferroelectric PbTiO3 thin films. *Journal of Applied Physics* **91**, 1495-1501, doi:10.1063/1.1431432 (2002).

50 Haun, M. J., Furman, E., Jang, S. J. & Cross, L. E. Thermodynamic theory of the lead zirconate-titanate solid solution system, part V: Theoretical calculations. *Ferroelectrics* **99**, 63-86, doi:10.1080/00150198908221440 (1989).

51 Park, K.-I. *et al.* Piezoelectric BaTiO3 Thin Film Nanogenerator on Plastic Substrates. *Nano letters* **10**, 4939-4943, doi:10.1021/nl102959k (2010).

52 Soin, N. *et al.* Exclusive self-aligned [small beta]-phase PVDF films with abnormal piezoelectric coefficient prepared via phase inversion. *Chemical communications* **51**, 8257-8260, doi:10.1039/C5CC01688F (2015).

53 Liu, X., Ma, J., Wu, X., Lin, L. & Wang, X. Polymeric Nanofibers with Ultrahigh Piezoelectricity via Self-Orientation of Nanocrystals. *ACS nano*, doi:10.1021/acsnano.6b07961 (2017).

54 Liu, F. *et al.* Room-temperature ferroelectricity in CuInP2S6 ultrathin flakes. *Nature communications* **7**, 12357, doi:10.1038/ncomms12357

http://www.nature.com/articles/ncomms12357#supplementary-information (2016).

55 Soni, R. *et al.* Giant electrode effect on tunnelling electroresistance in ferroelectric tunnel junctions. *Nature communications* **5**, 5414, doi:10.1038/ncomms6414

http://www.nature.com/articles/ncomms6414#supplementary-information (2014).

56 Zhao, S.-P. & Ren, X.-M. Toward design of multiple-property inorganic-organic hybrid compounds based on face-sharing octahedral iodoplumbate chains. *Dalton Transactions* **40**, 8261-8272, doi:10.1039/C0DT01806F (2011).

Chapter 5

Synthesis of Single Crystals of Two-dimensional Layered Hybrid Perovskite $(C_6H_5C_2H_4NH_3)_2CuCl_4$ Single Crystals and Mechanical Applications.

Beside the instability of lead halide perovskites which limit the ability of the materials to commercial applications, the heavy metal is also an environmental consideration. The success of achieving the 2D layered lead halide perovskite single crystals has enabled the field to grow new 2D lead-free hybrid materials. The stability issue of halide perovskites and the environmental concern about heavy metal compositions have been solved by using the 2D lead-free crystals. This chapter focuses on the synthesis of layered lead-free $(C_6H_5C_2H_4NH_3)_2CuCl_4$ *single crystals using supersaturation crystallization method. Their electronic properties have been characterized.*

5.1 Introduction

The hybrid organic-inorganic metal trihalide perovskites has attracted numerous studies because these materials possess possibilities for tailoring functionalities and physical properties. Recently, due to the easy in growth process and the stability issue single crystals of 2D layered $(C_6H_5\text{-}C_2H_4\text{-}NH_3)_2MCl_4$ (M = metals) has been a hot topic. We have succeeded in synthesis the PEPC reporting in the former chapter with lots of interesting properties. However, the environmental issue has not solved which limit the ability of PEPC to broad applications. In this chapter, toward the processing of a safe and multifunctional material, the lead-free $(C_6H_5\text{-}C_2H_4\text{-}NH_3)_2CuCl_4$ (PECC) single crystals are synthesized.

In previous reports, PECC single crystals were grown by spin coating and slow evaporation techniques which could only provide small crystals.[1,2] Herein, we introduce a PECC growth process using supersaturation method and DI water solvent at low temperature. The structure, morphology, topography, phase transition and device application of the as-prepared single crystals are also introduced.

5.2 Single Crystal Growth Process for PECC

The PECC precursor solution are prepared by mixing a stoichiometric amount of $CuCl_2$ and 2-Phenylethylamine hydrochloride in deionized (DI) water. Then, the solution is heated to 70^oC under stirring for 30 mins. After that, the temperature is reduced slowly to the room temperature. Some small dark yellow single crystals form in the solution and increase their side when the temperature low down (Fig. 5.1a).

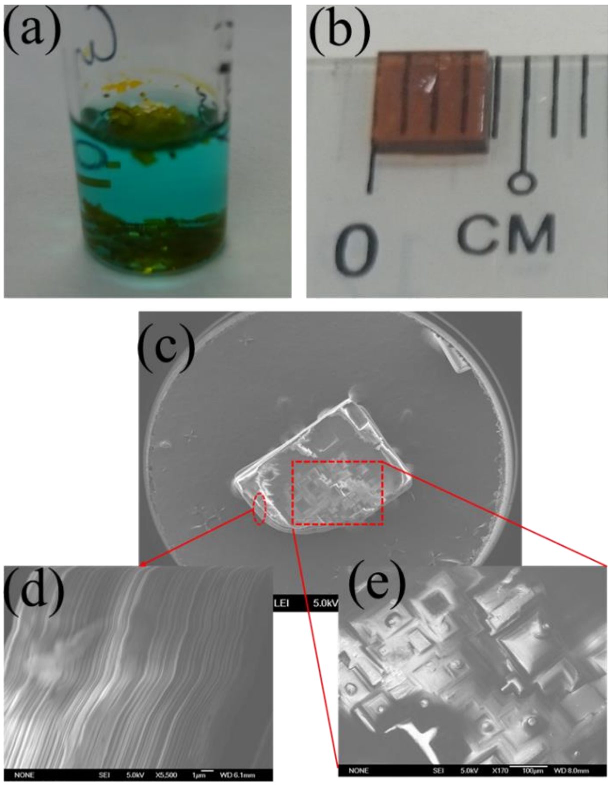

Figure 5.1 Crystal growth process. (a) PECC plate-like crystals grown in a vial using DI water as solvent, (b) Photographs of a brown PECC crystals after 3 h of growth, (c) The surface morphology of the as-prepared single crystal with the side-view (d) and top-view (e).

The process is repeated by taking some small seeds and put in to the new precursor solution. The seeds become bigger with a rectangle crystal of 4 × 4 mm in size after 3h growing which exhibits a facile growth rate (Fig. 5.1b). All steps of the crystallization process are employed under normal humidity of the lab and using DI water as the solvent. Therefore, the as-prepared single crystals possess long moisture stability. The crystal can be stored outside the glove box for months without any degradation.

Scanning electron microscopy (SEM) images of one small crystal (Fig 5.1c, d, e) show that the surface of as-prepared PECC single crystal is not smooth. Rectangle holes on the crystal surface are clearly seen. The forming of these hole can be explained by the layer-by-layer growth mode of the 2D layered perovskite crystal. The rectangle shape of the holes is relative to the crystalline structure of the perovskite material.

Particularly, the layered structure of the as-prepared crystal is obviously observed in the SEM side-view image (Fig. 5.1d). This characteristic should be used to make the micro layered devices based on the perovskite by peeling off its layers from a big crystal.

5.3 Structure Characterization

Recently, the crystal structure of $(C_6H_5C_2H_4NH_3)_2CuCl_4$ has been reported by Said et al.[1] Sketch of the PECC perovskite atomic structure shows in Figure 5.2b. According to the report, the PECC single crystal belongs to the Orthorhombic system, C2cb (no 64) with unit cell parameter a = 39.021(8) Å, b = 7.343 0(15) Å, c = 7.393 9(15) Å.

The XRD patterns of the single crystal, powder and pellet PECC are shown in Figure 5.2a. The pellets, which make from the grilled single crystal, is polycrystal resulting to the similar XRD patterns of powder (red) and pellet (black). Therefore, the polarization (if any) of the PECC pellet will oriented randomly.

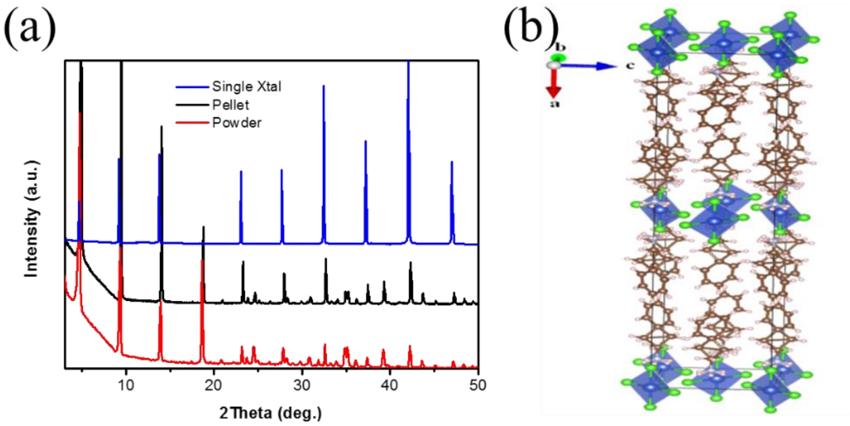

Figure 5.2 Structural properties of PECC single crystals. (a) XRD patterns recorded on the crystal surface (blue) and powder (red) and the pellet sample (black), (b) Sketch of the PECC perovskite atomic structure of one unit-cell (adopted from [1]).

The XRD pattern of the PECC single crystal shows the sharp peaks which demonstrates the high crystal quality of the as-prepared crystal (blue pattern in Fig. 5.2a). In comparison, the position of these peaks shows the agreement with the previous reports (see Fig. A1 in the Appendix). [1,3-5]

5.4 AFM Topography of the Crystal Surface

An Atomic Force Microscope (AFM MFP-3D, Asylum Research) is used to characterize the topography of as-grown PECC single crystals. The samples for experiment are peeled off from the big single crystal using the sticky tape. The step like AFM image is shown in Figure 5.3a.

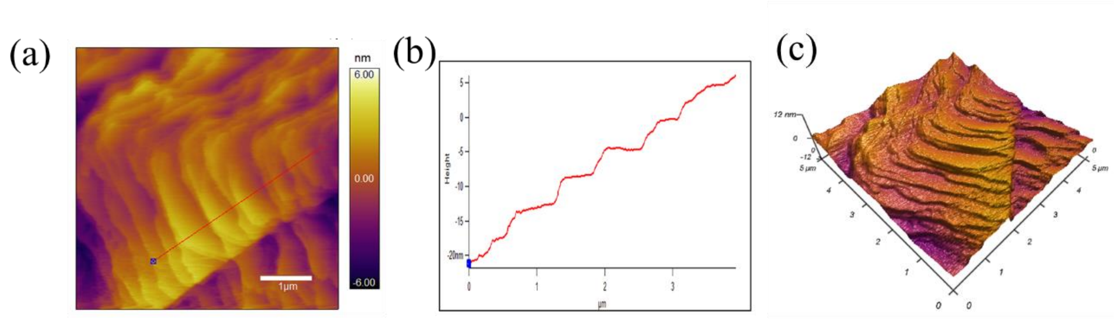

Figure 5.3 AFM topographic images of the PECC crystal (a) surface top view, (b) cross sectional profile along the redline in (a), and (c) 3D view.

As shown in Table 5.1, the layered structure of PECC single crystal have the surface roughness (RMS) of about 1.5 nm, and the thickness of each layer of about 5 nm estimating from the cross-sectional data (Fig. 5.3b). The 3D view image of the peeled sample in Figure 5.3c clearly represents to its layer structure.

Table 5.1: Roughness Data of the as-grown PECC single crystal from Fig. 5.3a.

Parameter	**Full Image Values:**
-----------------------------	-------------------
Standard Deviation, nm:	1.507
Max, nm	4.239
Min, nm	-5.465
RMS, nm	**1.507**
Average Deviation, nm	1.172
Skew:	-0.28

5.5 Piezoelectric Force Microscopy Characterizations and Phase Transition Behaviours

Similar to the PEPC crystal characterization, Piezoelectric Force Microscopy (PFM) measurement with a maximum bias voltage of ±10 V was employed to investigate the piezoelectric properties at room temperature of the PEPC crystals. The measured samples are also peeled off from a big single crystal to thin layered flake to guarantee the applied electric field through the samples.

Figure 5.4a shows the topography of a flake sample, and the corresponding amplitude and phase images. We can observe the different domain of the flake sample, clearly in the amplitude image.

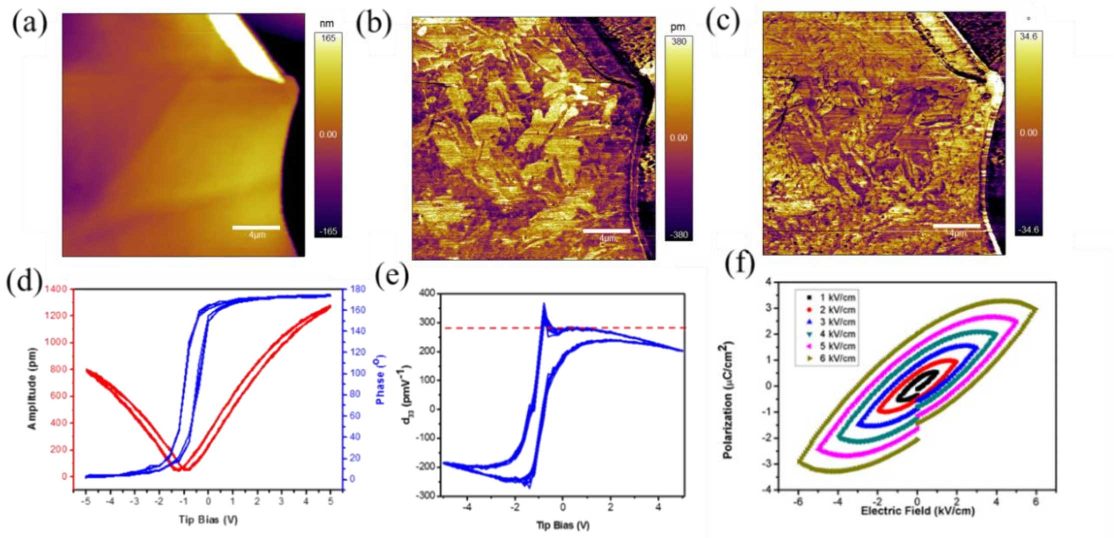

Figure 5.4. Characterizations of $PEACuCl_4$ single crystal: (a) Topography of the crystal flake, and its corresponding (b) amplitude and (c) phase images, (d) Amplitude and Phase signals, (e) piezoelectric coefficient d_{33}, (f) Polarization-Electric Field curves.

Phase and amplitude signals in Figure 5.4 d, e exhibit a 180° reproducible hysteresis loop in phase, and a butterfly like in amplitude curves which indicates that the change from downward to upward in polarization under the positive and negative applying of electric fields.

The piezoelectric coefficient d_{33} is also calculated from the former results and the equation 4.1. It indicates that a maximum value of piezoelectric coefficient of 270 V^{-1}

can be obtained. This result is a remarkable high value comparing to BaTiO$_{3,}$ PbZr$_{0.2}$Ti$_{0.8}$O$_{3,}$ PbTiO$_{3,}$ PVDF/GO nanofibers and as-prepared PEPC in the former chapter as well. [6] [7] [8] [9] [10]

The ferroelectric hysteresis loops of PECC single crystals with different apply voltages at frequency of 200 Hz and room temperature are shown in Figure 5.4d. The results demonstrate the ferroelectric behaviour of the as-prepared single crystals.

5.6 Box-in-box Switching Testing

Figure 5.5 shows the domain structural images of the PECC thin film sample. Like PEPC samples, the polycrystal thin film domains of PECC are smaller than that in single crystal. A large amount of red domain areas in Figure 5.5c indicates that the positive polarizations are dominant in the thin film sample.

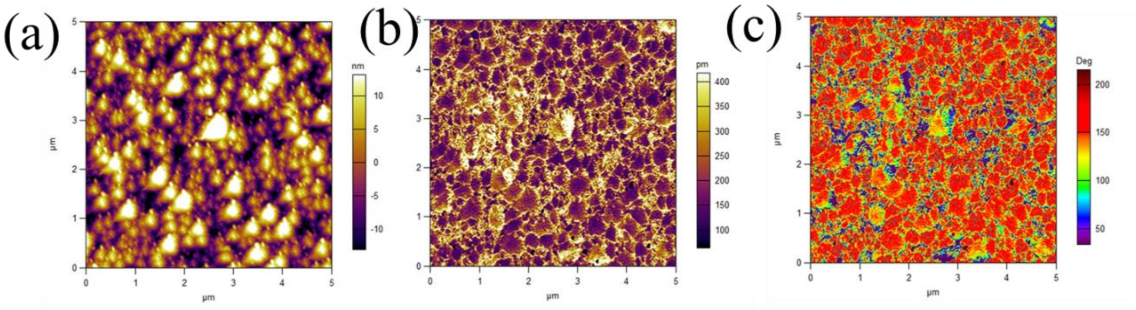

Topography

Amplitude

Phase

Figure 5.5 PFM images of a PECC thin film . (a) Topography of the as-prepared thin film. (b) Phase and amplitude curve employed on the as-prepared thin film.

Even though an 180^{o} change in hysteresis loop in thin film and flake samples of PECC does not guarantee the switchable ability of polarization under the electric field applications. Thus, the local switching test is employed to confirm.

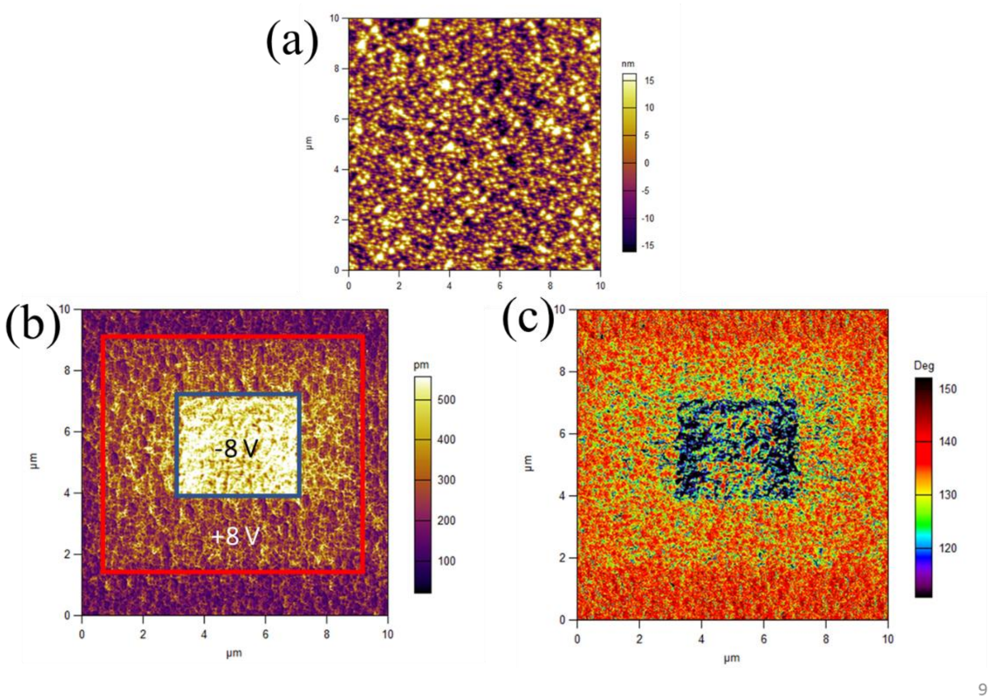

Figure 5.6 Box-in-box switching measurement of the PECC thin film.

A box-in-box switching test of the PECC thin film for an area of 10 × 10 μm^2 using ±8V applied bias via a Pt coated tip is presenting in Figure 5.6. A brighter square in the center of amplitude image corresponding to a darker area of phase image indicates the upward polarization orientation. Meanwhile, the downward polarization orientation is represented by a bigger square which can be observed through the contrast color between the square and the as-prepared thin film amplitude and phase signals (Fig. 5.6b, c).

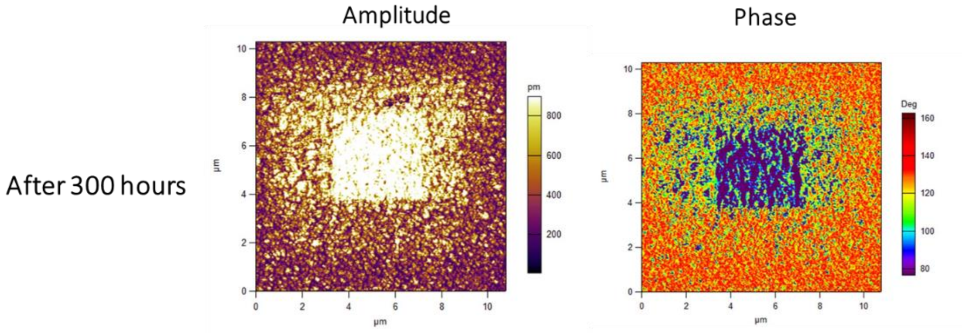

Figure 5.7 The Box-in-box area after 300 hours

Interestingly, after 300 hours of poling, the box-in-box amplitude and phase patterns are remained as shown in Figure 5.7. As the samples are stored outside glovebox under normal humidity condition at room temperature, it indicates the moisture stability of the PECC material.

5.7 Differential Scan Calorimetry Measurement (DSC) and Thermal and Moisture Stability

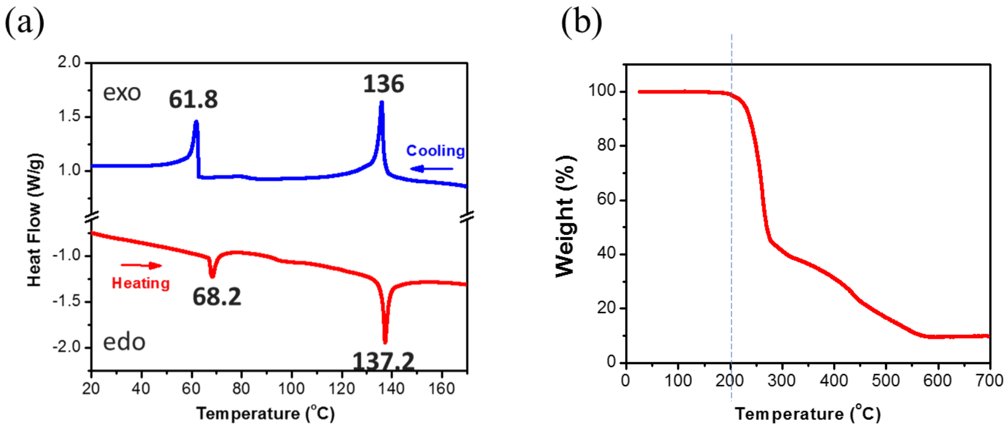

Figure 5.8 (a) DSC curves, and (b) TGA curve of the PECC single crystals.

The DSC and TGA curves of the PEPC single crystal are represented in Figure 5.8. The TGA data demonstrated that the as-prepared PECC perovskite single crystals are stable up to 200°C resulting in no change in TGA curve under the former temperature. Therefore, the two peaks in the DSC image (Gif. 5.8) attribute to two phases changing of the material. The two-phase changing temperature is 65°C and 136.6°C

The decomposition profile of the PECC single starts from the first weigh loss at about 200°C, indicating a major loss of Cl and organic compounds such as HCl and PEA. At higher temperatures, the weight loss is possibly associated with the combustion of $CuCl_2$.

5.8 PECC Piezoelectric Device

To investigate the ability of the as-prepared PECC single crystals in electronic application, we make a device from the PECC pellet which has an XRD pattern as shown in Figure 5.2a. The as-prepared PECC single crystals are collected of the growth process, then grilled and made to a pellet (Fig. 5.9a Inset). The SEM morphology image shows the compact structure of the PECC pellet.

To apply the pellet to piezoelectric, we need to do the poling process which help to rearrange the domain orientation in the pellet. Figure 5.9b illustrated the Corona Poling Process.[11] Corona Poling Process is a partial breakdown method of air, at atmospheric pressure, and is initiated by a discharge in an inhomogeneous high electric field, then helps to pole the polarization orientation of the sample (see Figure 5.9b).The pellet with a Cu bottom electrode is placed between a hot plate and needles, then to be applied with high voltage. In the first step of the Poling process, the temperature is increased above the curie temperature of the material to thermal erase the polarization in the polycrystal pellet. Then the high voltage is applied which help to polarize the pellet to one dominant direction (Fig. 5.9c).

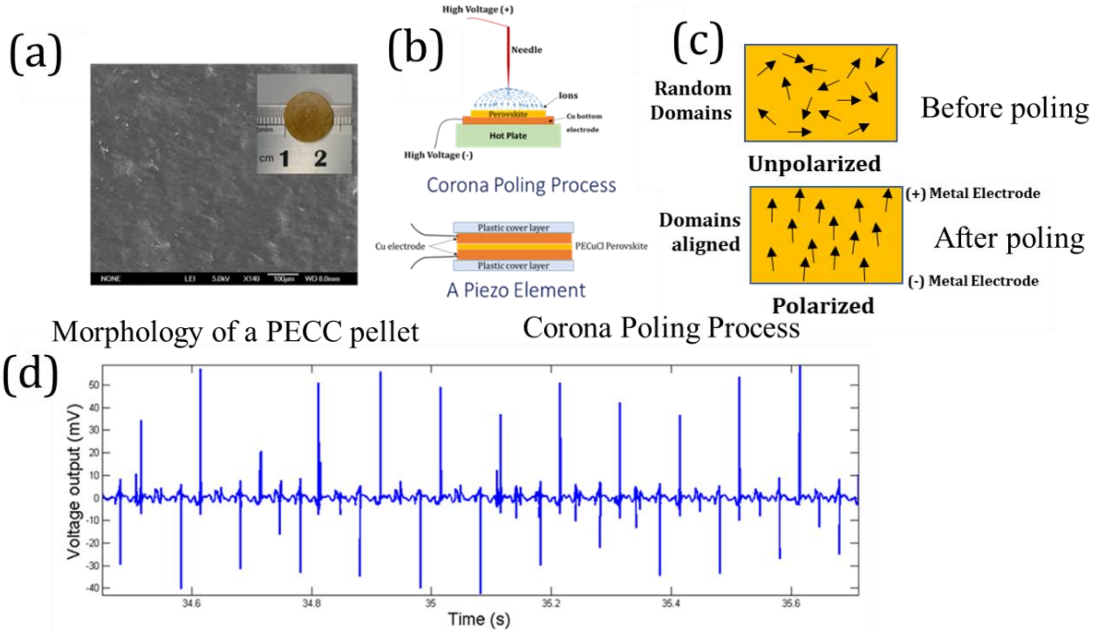

Figure 5.9 (a) Morphology of a PECC pellet. Inset is the photograph of the pellet. (b) Illustration of the Corona Poling Process and the device structure. (c) Illustration of the domain orientations before and after the poling process. (d) the Output voltage signal of a PECC device.

A Piezo Element with the structure is shown in Figure 5.9b is using for Vibration Controlled Test. Interestingly, a 50 mV output generated from the test demonstrates that the PECC device enable to be the potential material for piezoelectric (Fig. 5.9d).

5.9 Summary

In summary, we have introduced about the growth process of $(C_6H_5C_2H_4NH_3)_2CuCl_4$ single crystals using DI water as the solvent. The XRD data and SEM image demonstrate the high crystal quality of the as-prepared single crystal and their layered structure. The DSC and TGA data indicate the thermal stability of about 200°C and their phase transition behaviour of the crystals. The PFM results and box-in-box switching test show the domain structure in the crystal and thin film, and the ability to change the polarization orientation of the thin film sample. Particularly, a piezo device based on the crystal could generate a 0.05 V output. These results have promised new opportunities to employ the lead-free $(C_6H_5C_2H_4NH_3)_2CuCl_4$ single crystals in piezoelectric.

5.11 References

1 Said, K. & Abdesselam, B. A Cu based layered multifunctional material: (C 8 H 12 N) 2 CuCl 4 Optical and electronic properties. *Materials Research Express* **5**, 076305 (2018).

2 Park, G. *et al.* Solvent-dependent self-assembly of two dimensional layered perovskite (C6H5CH2CH2NH3)2MCl4 (M = Cu, Mn) thin films in ambient humidity. *Scientific reports* **8**, 4661, doi:10.1038/s41598-018-23012-2 (2018).

3 Solis-Ibarra, D., Smith, I. C. & Karunadasa, H. I. Post-synthetic halide conversion and selective halogen capture in hybrid perovskites. *Chemical Science* **6**, 4054-4059, doi:10.1039/C5SC01135C (2015).

4 3D long-range magnetic ordering in (C 2 H 5 NH 3) 2 CuCl 4 compound revealed by internal magnetic field from muon spin rotation and first principal calculation. *Physica B: Condensed Matter* (2018).

5 Yi, H.-B., Xia, F.-F., Zhou, Q. & Zeng, D. [CuCl3]− and [CuCl4]2− Hydrates in Concentrated Aqueous Solution: A Density Functional Theory and ab Initio Study. *The Journal of Physical Chemistry A* **115**, 4416-4426, doi:10.1021/jp109723v (2011).

6 Kighelman, Z., Damjanovic, D., Cantoni, M. & Setter, N. Properties of ferroelectric PbTiO3 thin films. *Journal of Applied Physics* **91**, 1495-1501, doi:10.1063/1.1431432 (2002).

7 Haun, M. J., Furman, E., Jang, S. J. & Cross, L. E. Thermodynamic theory of the lead zirconate-titanate solid solution system, part V: Theoretical calculations. *Ferroelectrics* **99**, 63-86, doi:10.1080/00150198908221440 (1989).

8 Park, K.-I. *et al.* Piezoelectric BaTiO3 Thin Film Nanogenerator on Plastic Substrates. *Nano letters* **10**, 4939-4943, doi:10.1021/nl102959k (2010).

9 Soin, N. *et al.* Exclusive self-aligned [small beta]-phase PVDF films with abnormal piezoelectric coefficient prepared via phase inversion. *Chemical communications* **51**, 8257-8260, doi:10.1039/C5CC01688F (2015).

10 Liu, X., Ma, J., Wu, X., Lin, L. & Wang, X. Polymeric Nanofibers with Ultrahigh Piezoelectricity via Self-Orientation of Nanocrystals. *ACS nano*, doi:10.1021/acsnano.6b07961 (2017).

11 Jung, Y., Kwak, J.-H., Lee, Y. H., Kim, W. D. & Hur, S. Development of a Multi-Channel Piezoelectric Acoustic Sensor Based on an Artificial Basilar Membrane. *Sensors (Basel, Switzerland)* **14**, 117-128, doi:10.3390/s140100117 (2014).

Chapter 6

Synthesis of Single crystals of 3D Methylammonium Lead Halide Perovskite $CH_3NH_3PbI_3$

The organic lead trihalide perovskites ($CH_3NH_3PbX_3$*, X=Cl, Br, I) thin films have demonstrated their attractions through the numerous perovskite studies in electronic and photonic applications.*[1-4] *Perovskite materials have been intensively employed not only in solar cells,*[5-14] *but also in photodetectors.*[15-17] *light-emitting diodes,*[18,19] *and lasing,*[20,21] *However, the major drawback of perovskite thin films is the moisture instability which limited them for being launched to the commercial market. In that critical situation, the single crystal has promised to enable the perovskite solar cells to break through their limitations. More and more reports have shown that the perovskite single crystal helped to suppress the charge recombination and prevent the bulk defect density, leading to higher PCE and longer stability.*[22-25] *Unlike traditional PSCs based on spin coating or dip coating polycrystal thin films, the single crystal one has been difficult to handle due to the lack of the sufficient growth crystallization methods. This chapter shows the result for large centimeter scaled* $CH_3NH_3PbI_3$ *perovskite single crystals growing by solution crystallization method and their crystalline, optoelectronic properties.*

6.1 Introduction

The idea to grow the large lead halide perovskite single crystals has engaged from the inverse temperature behaviour of precursor solutions of materials. The solubility of lead halide perovskite decreases with the temperature increase. Since the report of $CH_3NH_3PbI_3$ single crystal synthesis in 1987, which was grown from a HI acid solutions with Pb^{2+} and $CH_3NH_3^+$ ions in a proportional ratio,[26] more and more studies about $CH_3NH_3PbI_3$ perovskite single crystals have been reported based on the inverse temperature method.[27,28] [29,30] The extremely low trap density of the single crystal perovskites were measured of 10^9–10^{10} cm^{-3}, resulting in a long diffusion lengths (>175 μm) as well as a high carrier mobility (164 ± 25 cm^2 V^{-1} s^{-1}). These results have enabled the ability to synthesize high-performance single crystalline PSCs in large or wafer scales.

However, the limitation of the above crystallization methods was the time consumption which prevent them to fulfil the large-scale production standard. Recently, the solubility of $CH_3NH_3PbI_3$ have been observed to substantially reduce at elevated temperatures in certain organic solvents.[31,32] In the report, by using γ-butyrolactone (GBL) as the solvent to dissolve CH_3NH_3I and PbI_2 with the solution temperature up to 110°C, the authors have succeed in growing the crystals in large scales. Herein, a prompt method to grow high-quality centimetric $CH_3NH_3PbI_3$ single crystals under a lower temperature (70°C) using a novel solvent engineering approach have been introduced. The characterizations of the single crystal are also reported.

6.2 $CH_3NH_3PbI_3$ Crystal Growth Process

First, the six vials containing 1 mL of GBL solution were filled with CH_3NH_3I and PbI_2 in 1.23 M concentration. Then, different amount of acetonitrile (ACN) are added into the six successive vials respectively with 0; 0.2; 0.4; 0.6; 0.8; and 1.0 mL. After 1h of stirring at the room temperature (25°C), the solution in the first vial that using pure GBL remains cloudy, indicating the limitation in solubility in pure GBL.

Interestingly, although ACN is an anti-solvent for $CH_3NH_3PbI_3$,[33] the GBL/ACN mixture solvent exhibit to be a good solvent for the perovskite and all precursor solutions are clear. After that, the solutions are heated to 70°C for 30 minutes. Interestingly, the small black $CH_3NH_3PbI_3$ crystals appear inside the vials with ACN in GBL volumes equal or higher than 0.6 mL (Fig. 6.1b), and more crystals are obtained in the vials with higher ratios of ACN : GBL in solutions.

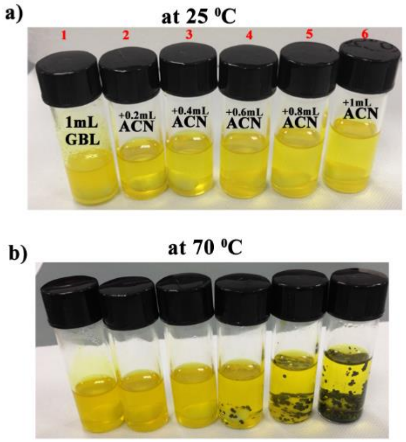

Figure 6.1 Photographs of precursor $CH_3NH_3PbI_3$ solutions with different ratio of ACN : GBL solvents at (a) room temperature and (b) after heating at 70°C.

In the second step, some small seed $CH_3NH_3PbI_3$ crystals are taken out from a vial and put into a new vial containing a fresh precursor solution at room temperature with similar solvent ratio as the former step (Fig. 6.2). The precursor solution is heated up to 70°C, allowing the further growth of the seeds (Fig. 6.2b). The prepared crystals by this novel solvent method have a same growth rate to the reported methods while synthesized at lower temperature, 70°C comparing to 110°C in reported ones.[31,32] The growth process was repeated at different temperatures and ratios. The ability of centimeter scaled growth of the novel solvent method has been demonstrated, resulting in the diameter of crystal of close to 1 cm after only 6 hours to even 1.7 cm after 3 days (Fig. 6.2b, c).

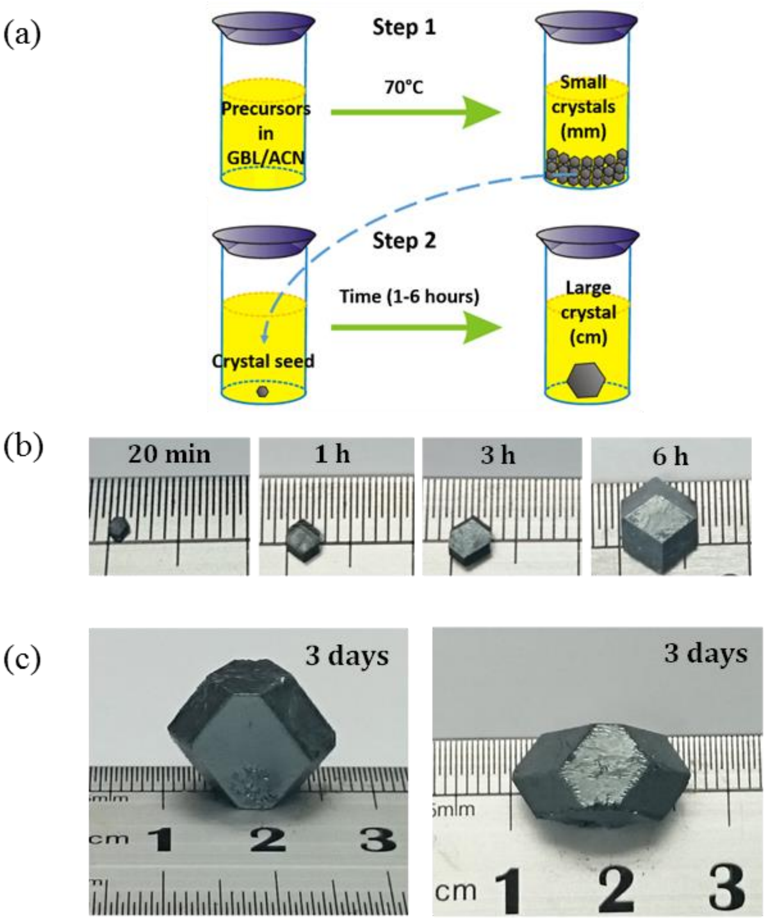

Figure 6.2 a) Schematics of the two-step solvent engineering process for the growth of large $CH_3NH_3PbI_3$ single crystals. b) Photographs of crystals obtained after various growth times (20 min to 6 h). c) Front (left) and side (right) views of a crystal obtained after 3 days (diameter=1.7 cm).

6.3 Solubility Test

In order to investigate the soluble ability in mixed solvents of as-prepared perovskite $CH_3NH_3PbI_3$ crystals, a solubility test has been employed. The powder for the solubility test was obtained by grinding the prepared crystals. The 200 µl vials of GBL/ACN solvent were heated under stirring while the perovskite powder was added with a small amount of 0.01 g by 0.01 g. Saturation condition was obtained when the perovskite powder did not dissolve completely after 30 mins in the solvent.

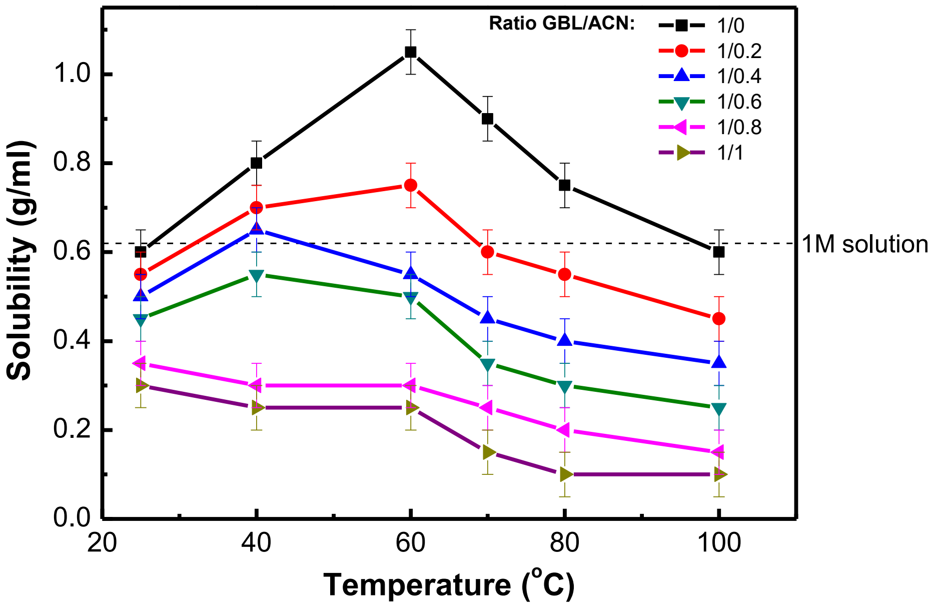

Figure 6.3 The temperature-dependent solubility of $CH_3NH_3PbI_3$ in GBL/ACN solvent with different ratios (v/v). The error bar is ± 0.05 g.

We note that the solubility of CH_3NH_3I and PbI_2 precursors in GBL/ACN solvent mixtures is more sensitive to temperature than in pure GBL (see figure 6.3).

6.4 Structure Characterizations

Figure 6.4a shows powder XRD patterns of the $CH_3NH_3PbI_3$ crystal powder grinding from the large as-prepared crystals. The positions of major peaks are at $2\theta=14.1°$, 28.4° and 40.4° (Fig. 6.4a, black pattern) indicate a tetragonal structure of as-prepared $CH_3NH_3PbI_3$ single crystals. Additionally, the sharp peaks of dominant (121) and (022) planes at $2\theta=23.5°$ and 24.5°, respectively, further reveal its tetragonal phase and its high crystalline quality as well. For comparison, the standard pattern data of a $CH_3NH_3PbI_3$ material with pure tetragonal phase are also calculated (Fig. 6.4a, red pattern), showing the phase matching with standard data of as-prepared single crystals. Figure 6.4b shows the simulated tetragonal structure of the $CH_3NH_3PbI_3$ crystal.

The high-resolution XRD was also employed to characterize the structure of $CH_3NH_3PbI_3$ single crystals. The only peaks of (112), (020), (224), (040), (336) and (060) planes at 2θ = 19.89°, 19.99°,40.43°, 40.63°, 62.44° and 62.76°, respectively, showing in the blue pattern in Fig. 6.4., confirm that the single-crystalline nature of as-prepared $CH_3NH_3PbI_3$ crystals.

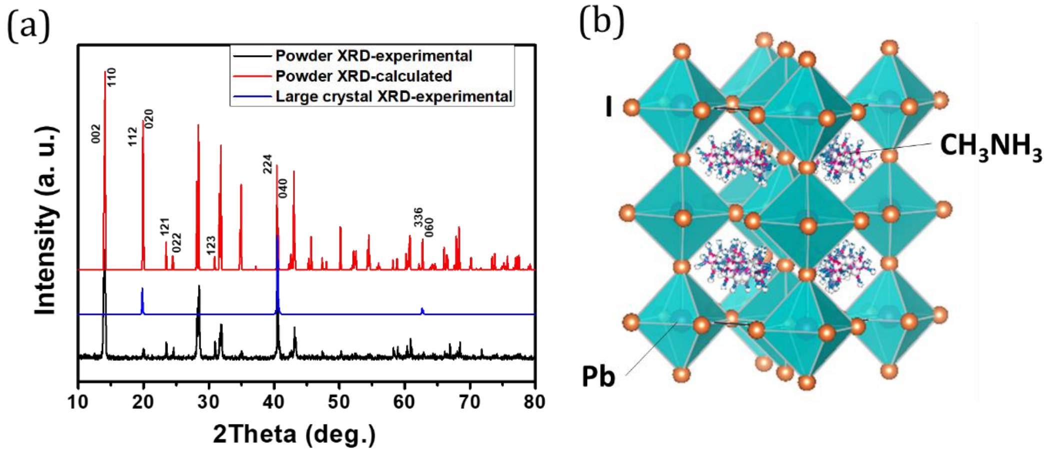

Figure 6.4 (a) XRD patterns collected on as-prepared single crystals (blue) and $CH_3NH_3PbI_3$ powder (black). The red pattern is the calculated data for the perovskite powder. (b) $CH_3NH_3PbI_3$ crystal structure.

For more phase confirmation, pole figures were taken from the $CH_3NH_3PbI_3$ crystal facets. The figures show an expected pattern for the [34] front facet, indicating that the <010> plane is parallel to the sample surface and also reveal its natural facets [34] and [35] by using the Euler angles calculation. (Fig. 6.5).

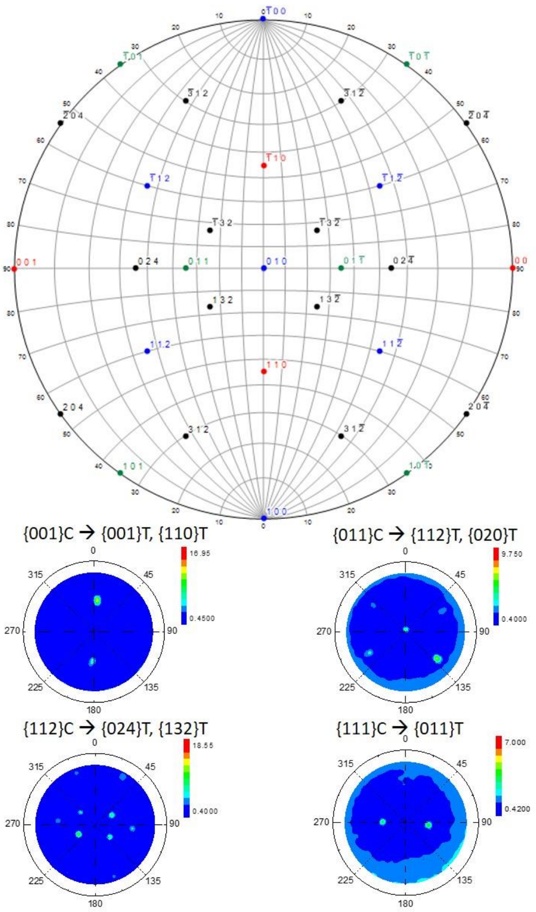

Figure 6.5 Natural facet pole figures of the as-prepared $CH_3NH_3PbI_3$ single crystal. Top: expected pattern for the [34] front facet. Bottom: corresponding experimental patterns.

6.5 SEM Morphology of Crystals

Figure 6.6 shows SEM images of an as-prepared $CH_3NH_3PbI_3$ single crystal. Due to the imbalance in growth rate between the lower part and upper part, which is in contact with the precursor solution, the perfect crystal with its shape as shown in Figure 6.7b are not easy to obtain. Instead of that, the non-perfect tetragonal crystals are formed. The outline of the crystal is indicated in Figure 6.7a. From the SEM surface images of the as-prepared crystal, we can observe the surface of as-prepared crystals with the smooth areas, followed with island-like and terrace-like ones.

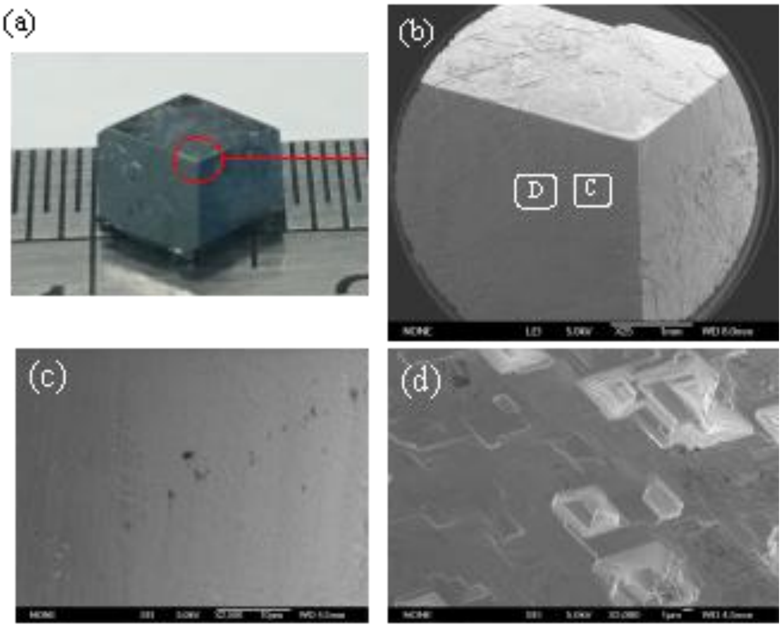

Figure 6.6 (a) Photography and(b-d) SEM images of a non-perfect tetragonal $CH_3NH_3PbI_3$ single crystal. (c and d) SEM images in show magnified view of one side faces indicated in (b).

The tetragonal terraces indicates a layer-by-layer growth mode of the as-prepared perovskite crystals. During the simultaneous nucleation and process, the nucleation clusters become larger and form the tetragonal islands on the crystal surface which may evolve into truncated tetragonal bipyramids with a dominant (100) plane.

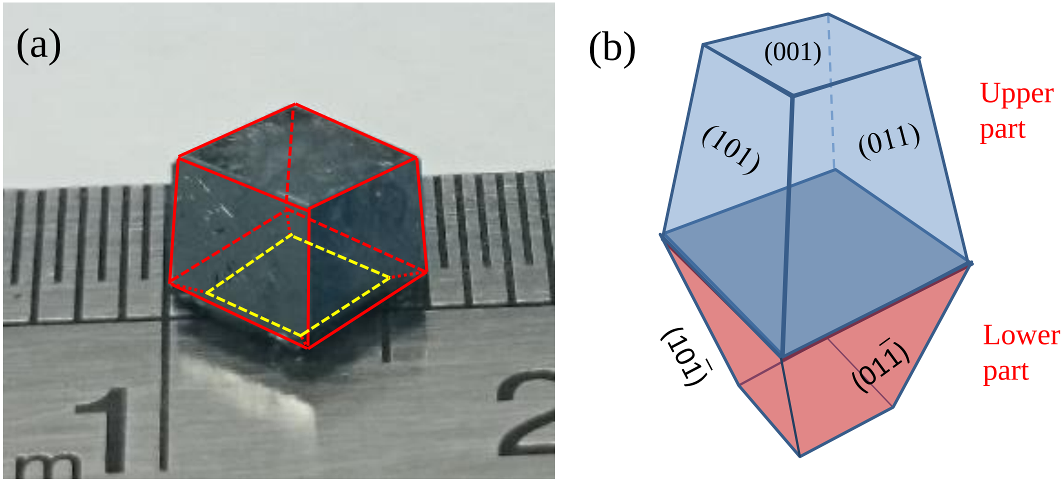

Figure 6.7 (a) Photograph of a non-perfect tetragonal crystal due to imbalanced growth rates between the upper part and lower part of the crystal. The outline of the crystal is indicated. (b) Schematics of a perfect tetragonal crystal. The upper part of the crystal in contact with solution.

6.6 Thermal Stability Test

The instability has been a major issue that limits the perovskite thin films in applications. The perovskite thin films were demonstrated to decompose at the temperature as low as 150°C.[22,32] For the as-prepared single crystal one, the thermal stability is characterized using thermogravimetric analysis (TGA) method. The characterization is working under nitrogen flow from room temperature up to 600°C (Fig. 6.8). The TGA results of as-prepared perovskite crystals shows no signature of mass loss with the temperature under 240°C, indicating their higher thermal stability comparing to the thin film counterpart. Over 240°C, the crystals undertake a 20% mass loss of HI, following by a 6% mass loss of the CH_3NH_2 component at 337°C, indicating a stronger binding of the amine group in the perovskite compound than HI. At around 385°C and beyond, the inorganic precursor PbI_2 is gradually sublimed.

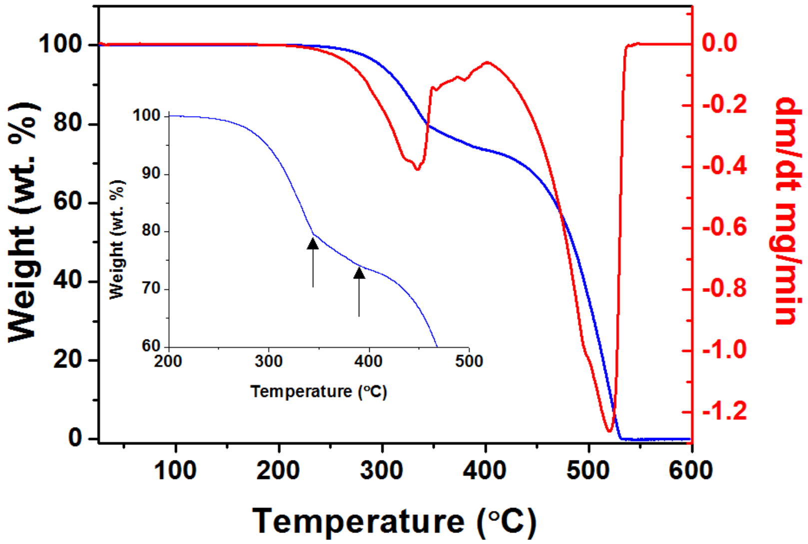

Figure 6.8 Thermal gravimetric analysis (TGA) of the $CH_3NH_3PbI_3$ single crystals.

6.7 Photonic Properties

Last, but not least, the photonic properties of large $CH_3NH_3PbI_3$ crystals were investigated. The steady-state PL of the crystals in Figure 6.9 shows a red shift in PL position of the as-prepared crystals comparing to the thin film counterpart (783 nm for single crystal and 775 nm for thin film). The result should refer to a weaker lattice strain in single crystal than thin film one.[30] Additionally, at the respective measured PL peak wavelengths, their time-dependent PL signals were also evaluated.

Figure 6.9b represents their respective biexponential fitting carrier dynamics. On the one hand, the single crystal performs a slower (τ=57.0±0.7 ns) and a fast lifetime (τ=4.9±0.1 ns). The slow lifetime is considered the carrier recombination lifetime from beneath the surface (in the bulk), while the fast one is ascribed to that on the surface.[30] On the other hand, the thin film only exhibited a fast decay (τ=5.1±0.1 ns).

In comparison with the surface as well as polycrystalline thin film, the longer recombination lifetime in bulk $CH_3NH_3PbI_3$ crystal can attribute to the reduce in trap density, characteristic of bulk properties of the materials.[29,30] The impurities and surface defects in crystal front face and a thin film counterpart have a fiercely impact on their recombination lifetime resulting to a faster lifetime of approximately 5 ns.

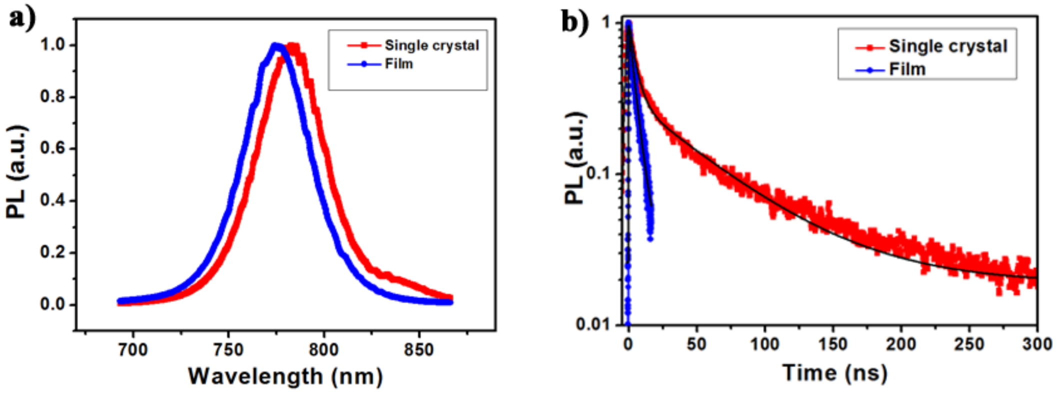

Figure 6.9 (a) Steady-state and (b) time-resolved PL spectra of $CH_3NH_3PbI_3$ single crystals and thin films counterpart. Black lines correspond calculated fits.

6.8 Summary

In summary, we have introduced a facile, novel method in synthesize the centimetric $CH_3NH_3PbI_3$ perovskite single crystals at low temperature (70°C) using mixtures solvent of ACN/GBL. The SEM and XRD results demonstrate the high quality of the tetragonal structure $CH_3NH_3PbI_3$ crystals with a better thermal stability comparing to the thin films, resulting from the TGA data. The time-dependent PL signals reveal the slow carrier dynamic, which confirming the lifetime of carriers propagating deeper in the crystal. Our work should provide new approaches to employ the centimetric $CH_3NH_3PbI_3$ single crystals for both scientific study and technological applications in PV solar cells.

6.9 References

1 Im, J. H., Lee, C. R., Lee, J. W., Park, S. W. & Park, N. G. 6.5% efficient perovskite quantum-dot-sensitized solar cell. *Nanoscale* **3**, 4088-4093, doi:10.1039/c1nr10867k (2011).

2 Wehrenfennig, C., Eperon, G. E., Johnston, M. B., Snaith, H. J. & Herz, L. M. High Charge Carrier Mobilities and Lifetimes in Organolead Trihalide Perovskites. *Advanced Materials* **26**, 1584-1589, doi:10.1002/adma.201305172 (2014).

3 Edri, E. *et al.* Why lead methylammonium tri-iodide perovskite-based solar cells require a mesoporous electron transporting scaffold (but not necessarily a hole conductor). *Nano Lett* **14**, 1000-1004, doi:10.1021/nl404454h (2014).

4 Xing, G. *et al.* Long-range balanced electron- and hole-transport lengths in organic-inorganic CH3NH3PbI3. *Science* **342**, 344-347, doi:10.1126/science.1243167 (2013).

5 Kim, H. S. *et al.* Lead iodide perovskite sensitized all-solid-state submicron thin film mesoscopic solar cell with efficiency exceeding 9%. *Sci Rep* **2**, 591, doi:10.1038/srep00591 (2012).

6 Lee, M. M., Teuscher, J., Miyasaka, T., Murakami, T. N. & Snaith, H. J. Efficient hybrid solar cells based on meso-superstructured organometal halide perovskites. *Science* **338**, 643-647, doi:10.1126/science.1228604 (2012).

7 Burschka, J. *et al.* Sequential deposition as a route to high-performance perovskite-sensitized solar cells. *Nature* **499**, 316-319, doi:10.1038/nature12340 (2013).

8 Jeon, N. J. *et al.* Compositional engineering of perovskite materials for high-performance solar cells. *Nature* **517**, 476-480, doi:10.1038/nature14133 (2015).

9 Liu, M., Johnston, M. B. & Snaith, H. J. Efficient planar heterojunction perovskite solar cells by vapour deposition. *Nature* **501**, 395-398, doi:10.1038/nature12509 (2013).

10 Nie, W. *et al.* High-efficiency solution-processed perovskite solar cells with millimeter-scale grains. *Science* **347**, 522-525, doi:10.1126/science.aaa0472 (2015).

11 Li, X. *et al.* Improved performance and stability of perovskite solar cells by crystal crosslinking with alkylphosphonic acid ω-ammonium chlorides. *Nat Chem* **7**, 703-711, doi:10.1038/nchem.2324 http://www.nature.com/nchem/journal/v7/n9/abs/nchem.2324.html#supplementary-information (2015).

12 Zhou, H. *et al.* Interface engineering of highly efficient perovskite solar cells. *Science* **345**, 542-546 (2014).

13 Yang, W. S. *et al.* High-performance photovoltaic perovskite layers fabricated through intramolecular exchange. *Science* **348**, 1234-1237, doi:10.1126/science.aaa9272 (2015).

14 Hu, X. *et al.* High-Performance Flexible Broadband Photodetector Based on Organolead Halide Perovskite. *Adv. Funct. Mater.* **24**, 7373–7380, doi:10.1002/adfm.201402020 (2014).

15 Zhuo, S., Zhang, J., Shi, Y., Huang, Y. & Zhang, B. Self-Template-Directed Synthesis of Porous Perovskite Nanowires at Room Temperature for High-Performance Visible-Light Photodetectors. *Angew. Chem. Int. Ed.* **54**, 5693-5696, doi:10.1002/anie.201411956 (2015).

16 Deng, H. *et al.* Growth, Patterning and Alignment of Organolead Iodide Perovskite Nanowires for Optoelectronic Devices. *Nanoscale* **7**, 4163-4170, doi:10.1039/C4NR06982J (2015).

17 Chin, X. Y., Cortecchia, D., Yin, J., Bruno, A. & Soci, C. Lead iodide perovskite light-emitting field-effect transistor. *Nat. Commun.* **6**, 7383, doi:10.1038/ncomms8383 (2015).

18 Stranks, S. D. & Snaith, H. J. Metal-halide perovskites for photovoltaic and light-emitting devices. *Nat Nano* **10**, 391-402, doi:10.1038/nnano.2015.90 (2015).

19 Xing, G. *et al.* Low-temperature solution-processed wavelength-tunable perovskites for lasing. *Nat Mater* **13**, 476-480, doi:10.1038/nmat3911

http://www.nature.com/nmat/journal/v13/n5/abs/nmat3911.html#supplementary-information (2014).

20 Zhu, H. *et al.* Lead halide perovskite nanowire lasers with low lasing thresholds and high quality factors. *Nat. Mater.* **14**, 636–642, doi:10.1038/nmat4271

http://www.nature.com/nmat/journal/vaop/ncurrent/abs/nmat4271.html#supplementary-information (2015).

21 Kojima, A., Teshima, K., Shirai, Y. & Miyasaka, T. Organometal halide perovskites as visible-light sensitizers for photovoltaic cells. *Journal of the American Chemical Society* **131**, 6050-6051 (2009).

22 Dualeh, A. *et al.* Effect of Annealing Temperature on Film Morphology of Organic-Inorganic Hybrid Pervoskite Solid-State Solar Cells. *Advanced Functional Materials* **24**, 3250-3258, doi:10.1002/adfm.201304022 (2014).

23 Xiao, Z. *et al.* Solvent Annealing of Perovskite-Induced Crystal Growth for Photovoltaic-Device Efficiency Enhancement. *Adv. Mater.* **26**, 6503–6509, doi:10.1002/adma.201401685 (2014).

24 Zheng, X., Chen, B., Wu, C. & Priya, S. Room temperature fabrication of CH3NH3PbBr3 by anti-solvent assisted crystallization approach for perovskite solar cells with fast response and small J–V hysteresis. *Nano Energy* **17**, 269-278, doi:http://dx.doi.org/10.1016/j.nanoen.2015.08.023 (2015).

25 Zhou, Y. *et al.* Growth Control of Compact CH3NH3PbI3 Thin Films via Enhanced Solid-State Precursor Reaction for Efficient Planar Perovskite Solar Cells. *J. Mater. Chem. A* **3**, 9249-9256, doi:10.1039/C4TA07036D (2015).

26 Poglitsch, A. & Weber, D. Dynamic disorder in methylammoniumtrihalogenoplumbates (II) observed by millimeter-wave spectroscopy. *The Journal of Chemical Physics* **87**, 6373-6378, doi:doi:http://dx.doi.org/10.1063/1.453467 (1987).

27 Baikie, T. *et al.* Synthesis and crystal chemistry of the hybrid perovskite (CH3NH3)PbI3 for solid-state sensitised solar cell applications. *Journal of Materials Chemistry A* **1**, 5628, doi:10.1039/c3ta10518k (2013).

28 Dang, Y. *et al.* Bulk crystal growth of hybrid perovskite material CH3NH3PbI3. *CrystEngComm* **17**, 665-670, doi:10.1039/c4ce02106a (2015).

29 Dong, Q. *et al.* Electron-hole diffusion lengths > 175 μm in solution-grown CH3NH3PbI3 single crystals. *Science* **347**, 967-970, doi:10.1126/science.aaa5760 (2015).

30 Shi, D. *et al.* Low trap-state density and long carrier diffusion in organolead trihalide perovskite single crystals. *Science* **347**, 519-522, doi:10.1126/science.aaa2725 (2015).

31 Saidaminov, M. I. *et al.* High-quality bulk hybrid perovskite single crystals within minutes by inverse temperature crystallization. *Nature communications* **6**, doi:10.1038/ncomms8586 (2015).

32 Liu, Y. *et al.* Two-Inch-Sized Perovskite CH3NH3PbX3 (X = Cl, Br, I) Crystals: Growth and Characterization. *Advanced Materials* **27**, 5176-5183, doi:10.1002/adma.201502597 (2015).

33 Dou, L. *et al.* Atomically thin two-dimensional organic-inorganic hybrid perovskites. *Science* **349**, 1518-1521, doi:10.1126/science.aac7660 (2015).

34 Cheng, Z. & Lin, J. Layered organic-inorganic hybrid perovskites: structure, optical properties, film preparation, patterning and templating engineering. *CrystEngComm* **12**, 2646-2662, doi:10.1039/C001929A (2010).

35 Baikie, T. *et al.* A combined single crystal neutron/X-ray diffraction and solid-state nuclear magnetic resonance study of the hybrid perovskites CH3NH3PbX3 (X = I, Br and Cl). *Journal of Materials Chemistry A* **3**, 9298-9307, doi:10.1039/C5TA01125F (2015).

Chapter 7

Synthesis of Perovskite $CH_3NH_3PbBr_3$ and $CH_3NH_3PbCl_3$ Single Crystals and Current Response Mechanisms

The photovoltaic performance of hybrid lead halide perovskite solar cells has been advancing recently by using the $MAPbX_3$ *(where MA stands for methylammonium cations, X = I, Br, Cl). Obviously, the improvement of efficiency and stability is also a major issue. One of the approaches is using single crystals instead of thin films. This paper represents a study on preparing the* $MAPbBr_3$ *and* $MAPbCl_3$ *perovskite crystals using electric oven inverse temperature reactive crystallization (ITC) process at* 70^oC*. The XRD patterns reveal their high crystalline quality. The surface topography shows the appearance of cubic holes consistent with the cubic structure of both crystals. The conductivity behaviours of* $MAPbBr_3$ *and* $MAPbCl_3$ *perovskite crystals were also investigated. The mechanism of current response demonstrated that the conductivity behaviour of* $MAPbBr_3$ *crystals follow the typical Schottky contact feature. Interestingly, the tunnelling effect in the conductivity behaviour was observed in* $MAPbCl_3$ *crystals.*

7.2 Introduction

Lead halide perovskites have recently emerged as the most promising next generation photovoltaic materials with high efficiencies which achieved up to 20% of perovskite solar cells (PSCs).[1,2] Some advances such as large absorption coefficient, high carrier mobility, and long-range balanced carrier transport length make perovskites to be used in not only photovoltaics but also in laser,[3-5] photosynthesis,[6-8] and photo-detection[9-11] applications.

The structure of lead halide perovskites is AMX_3 formula which combines two cubic geometries with 8 organic cations A located at 8 vertexes of an M-centered cube (M = Pb). Cation Pb^{2+} is also the center of an octahedron forming by six anions X which located at the centers of six faces of the Pb-centered cube.[12,13]

Most recently, large scale single crystal hybrid halide perovskite has been widely studied. The single crystals overcome the major problem known as grain boundaries in polycrystalline films. It is believed that the minimal single crystal grains can elongate the diffusion length resulted from greater carrier mobility and smaller trap density in the single crystal than polycrystalline thin films.[14]

In the work of the Shi group, $MAPbBr_3$ single crystals achieved low trap state densities on the order of 10^9 to 10^{10} per cm^3 and charge carrier diffusion length exceed of 10 µm, ten time larger than polycrystalline films.[15] For single crystal $MAPbI_3$, Dong and co-workers reported that the diffusion length obtained 175 µm under 1 sun illumination and 3 mm under 0.003% sun illumination.[14]

The electron conductivity behaviour of $MAPbX_3$ single crystals were investigated in several publications.[10,16,17] However, the mechanism behind the behaviour has not been mentioned clearly. In this work, we conduct the electron conductivity of $MAPbBr_3$ and $MAPbCl_3$ perovskite single crystals by conducting AFM. Moreover, the mechanism based on Schottky contact feature of conductivity behaviour are introduced.

7.3 Single Crystal Growth Process

Recently, anti-solvent vapor –assisted crystallization (AVC) method has been used for the growth of perovskite crystal. In AVC method, an appropriate anti-solvent is slowly diffused into a solution containing the crystal precursors, leads to the growth of crystal. [9] In addition, based on the fact that perovskites exhibit inverse temperature solubility behaviour in certain solvents.[18] The inverse temperature crystallization (ITC) has been also used. The ITC method overcomes the time-consuming conventional crystallization methods such as the typical cooling or anti-solvent vapor-assisted crystallization techniques.[14,17] So far, the temperature of the oil bath in the ITC method was 80°C for $MAPbBr_3$ and $MAPbCl_3$. Herein, we followed the ITC method but used electric oven at 70°C instead of the oil bath and the hot plate. Using electric oven ITC method can provide an evenly temperature to the solvent and can used to make large amount of crystals.

The choice of a suitable solvent is also a crucial factor that determines the crystal growth process and its quality. For lead trihalide perovskite, the most commonly used solvents are ɣ-butyrolactone (GBL), N,N-dimethylformamide (DMF), and dimethylsulphoxide (DMSO).[19] For $MAPbBr_3$ crystal, the widely used solvent was DCM. These organic compounds can minimize the interactions between the ions during the growth crystal process due to their poor solubility for both MAX and PbX_2 as well as poor hydrogen bond-forming ability. Unlike $MAPbBr_3$, GBL was considered as most suitable solvent for the $MAPBI_3$ growth. ITC method of $MAPbI_3$ was only possible in GBL solution. For $MAPbCl_3$ crystal, due to the low solubility of $PbCl_2$, DMSO was used as solvent. However, no precipitates were observed in this case. Therefore, using mixing solvent of DMSO: DMF was a good choice.

We conducted a facile solution-processed method to prepare $MAPbBr_3$ and $MAPbCl_3$ crystals using electric oven. As shown in Fig 7.1a, one molar solution containing $PbBr_2$ and MABr was prepared in DMF and two molar solution containing $PbCl_2$ and MACl was prepared in DMSO: DMF (3:1 v/v). All solutions were prepared at room temperature under stirring. After that, solutions were filtered using PTFE filter with 0.2 µm pore size and replaced in vials. The vials were kept in an electric oven at 70°C under ambient condition and humidity of around 50%. The small crystals were obtained after 30 min. In order to make bigger crystals, a small crystal was carefully taken out from the vial and put into the new vial with new solution. The crystals used for measurement were grown for 1.5 h. Fig 7.1b and c shows the $MAPbBr_3$ and $MAPbCl_3$ crystal growth at different time intervals. After 10 mins in the electric oven at 70°C, we can obtain small crystals of $MAPbBr_3$ (Fig 7.1b) and $MAPbCl_3$ (Fig 7.1c). The size of $MAPbBr_3$ crystal became 5×5 mm and 4.5×4.5 mm with $MAPbCl_3$ crystal after 1.5 h as shown in Fig 7.1d.

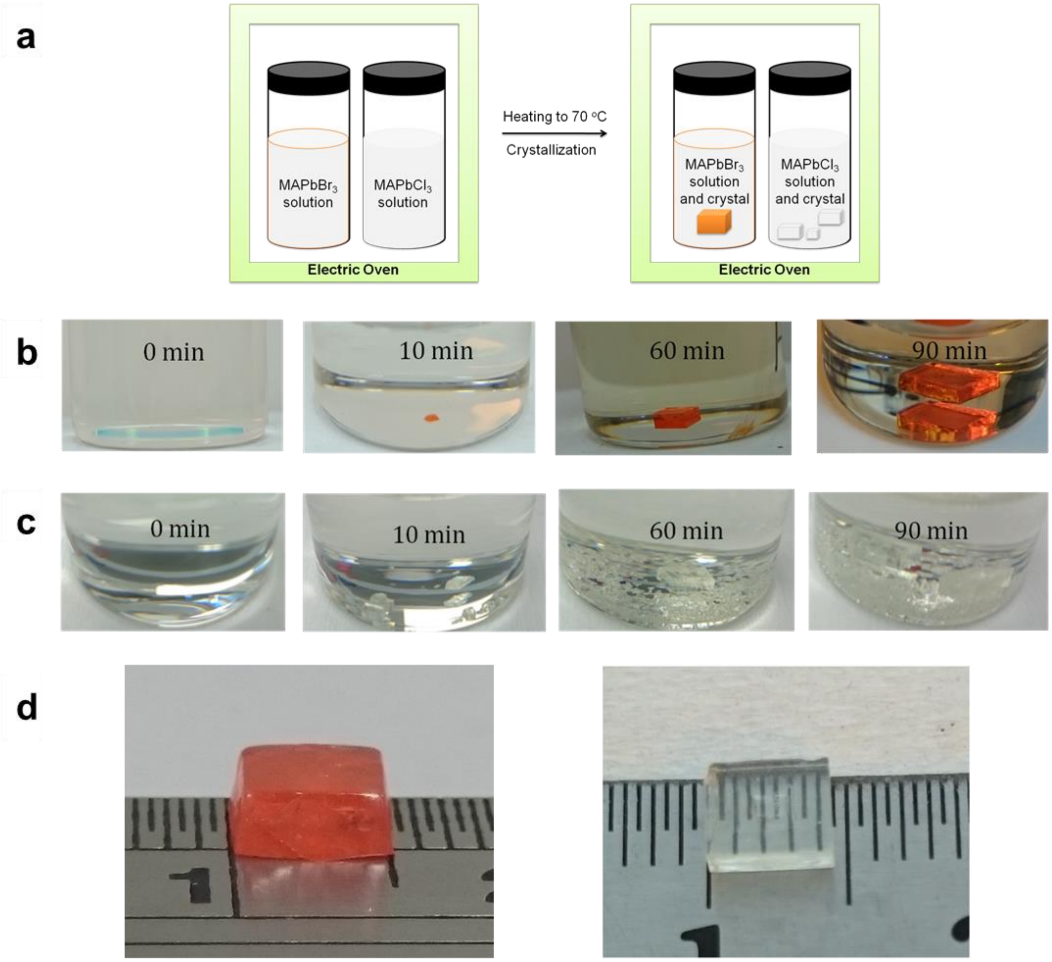

Figure 7.1 Crystal Growth process. **(a)** Schematic illustration of the crystal growth in a electric oven at temperature of 70^{o}C under ambient condition and humidity of around 50%. **(b, c)** MAPbBr$_3$ and MAPbCl$_3$ crystal growth at different time intervals. **(d)** MAPbBr$_3$ (orange) and MAPbCl$_3$ (transparent and colorless) crystals after 1.5 h.

7.4 Structure Characterizations

Fig 7.2a shows the XRD patterns of the surface of the as-prepared MAPbBr$_3$ and MAPbCl$_3$ crystals. For the MAPbBr$_3$ crystal, the specific peaks located at 2θ = 15.2 ^{o}, 30.4 ^{o}, 46.4 ^{o}, 62.8 ^{o}. For the MAPbCl3, 2θ = 15.7 ^{o}, 31.7 ^{o}, 48.1 ^{o}, 65.7 ^{o}. The XRD data demonstrate pure perovskite phase for both MAPbBr$_3$ and MAPbCl$_3$ with cubic structure and dominant (100) plane. The peaks of MAPbBr$_3$ and MAPbCl$_3$ correspond to the (100), (200), (300), and (400) of plane crystal directions which confirm that the high crystalline quality.

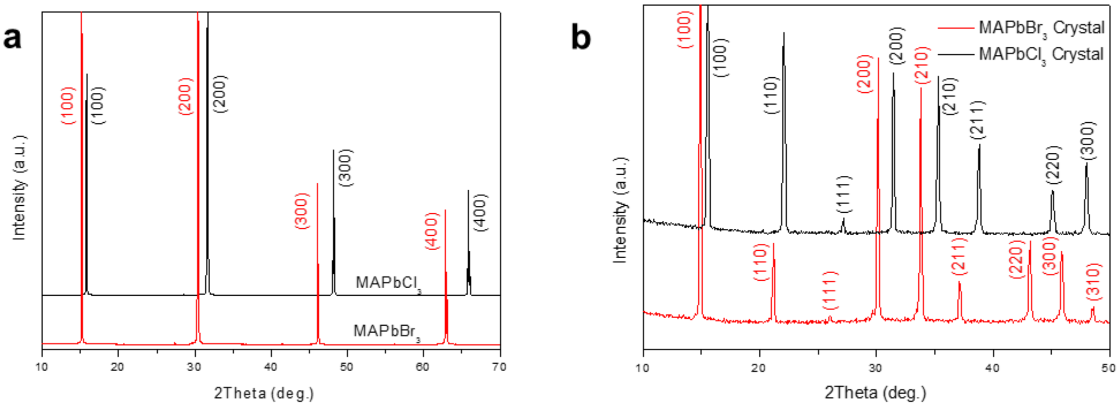

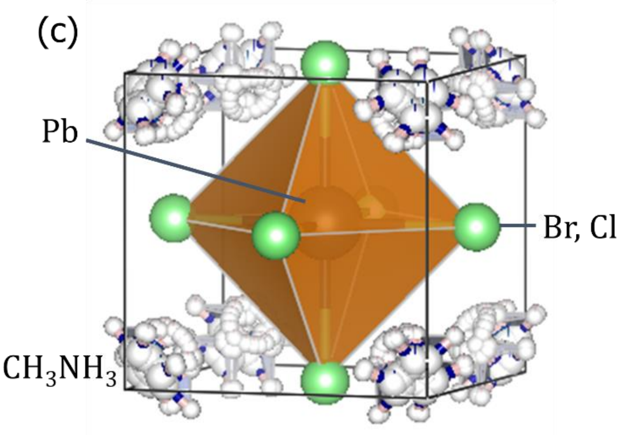

Figure 7.2: (a) XRD patterns of as-prepared $MAPbBr_3$ and $MAPbCl_3$ surface crystals, (b) Their Powder XRD patterns, and (c) their crystal structures.

The Bragg's law describes the condition on the scattering angle, θ, for the constructive interference to be at its strongest: $\lambda = 2nd\sin\theta$, where n is a positive integer and λ is the wavelength of incident wave. According to the Bragg's law, the (100), (200), (300), and (400) peaks in the XRD pattern correspond to n = 1, 2, 3 of the crystalline lattice planes (100).

Powder XRD pattern (PXRD) of the ground crystals confirmed pure single-phase of cubic $MAPbBr_3$ and $MAPbCl_3$ perovskite (Figure 7.2b), showing consistency with the previously reported PXRD data of the same single crystals obtained through the different crystallization methods.[17,18,20,21]

7.5 Optical Properties

The Fig 7.3 shows the optical properties of the large $MAPbBr_3$ and $MAPbCl_3$ crystals collected by absorbance and the photoluminescence (PL) spectroscopy. As shown in Fig 7.3a, the single-crystalline perovskite possesses optical absorption with the edge to ~570 nm with $MAPbBr_3$ and ~440 nm with $MAPbBr_3$.

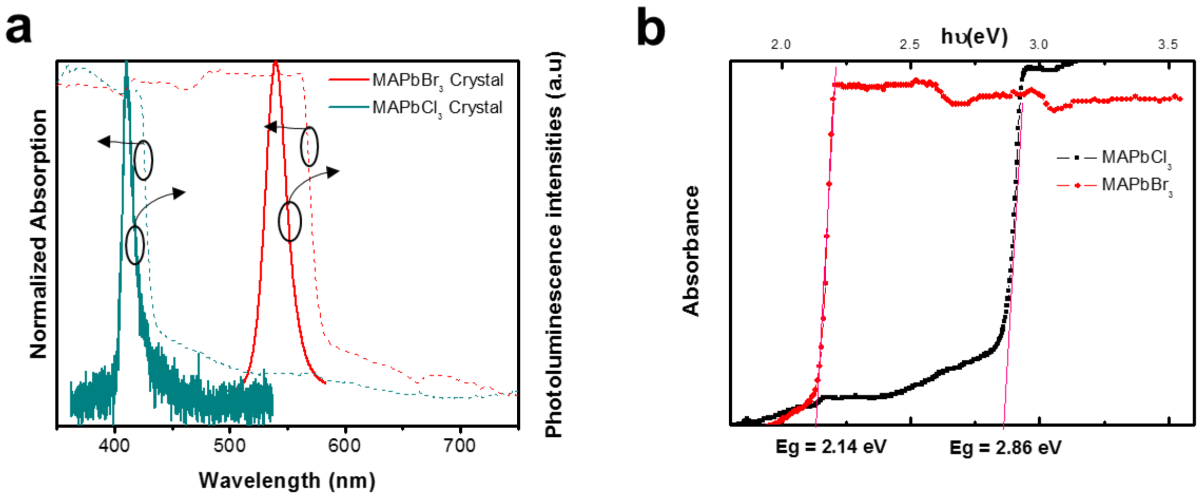

Figure 7.3 Optical spectra. (a) Steady-state absorbance and photoluminescence of $MAPbBr_3$ and $MAPbCl_3$ crystals. (b) Absorbance versus photon energy and the determined band gap Eg.

There is an obvious "cut-off" features in the two absorption spectrums, indicating that $MAPbBr_3$ and $MAPbCl_3$ are direct band gap semiconductors. From the absorbance versus photon energy, we can determine band gaps Eg = 2.14 eV for $MAPbBr_3$ and Eg = 2.86 eV for $MAPbCl_3$. As the absorption of the single crystalline $MAPbBr_3$ perovskite is across to the orange range spectrum, its colour is orange, as shown in Fig 7.1d. Similarly, the absorption of the single $MAPbCl_3$ crystal is across to the UV range spectrum, it is transparent and colourless. The photoluminescence peak of the $MAPbBr_3$ perovskite crystal is measured at 541 nm with $MAPbBr_3$ and at 410 with $MAPbCl_3$, near the band edge, indicating the appearance of trap in the crystals.

7.6 Surface Topographic Properties

The topographies of $MAPbBr_3$ and $MAPbCl_3$ crystals are also investigated. AFM images in Fig 7.4 shows the cubic holes on the both crystal surfaces corresponding to the cubic structure of these crystals. Crystals are growing layer by layer from the cubic areas corresponding to the cubic structure of the crystals in structural characterization.

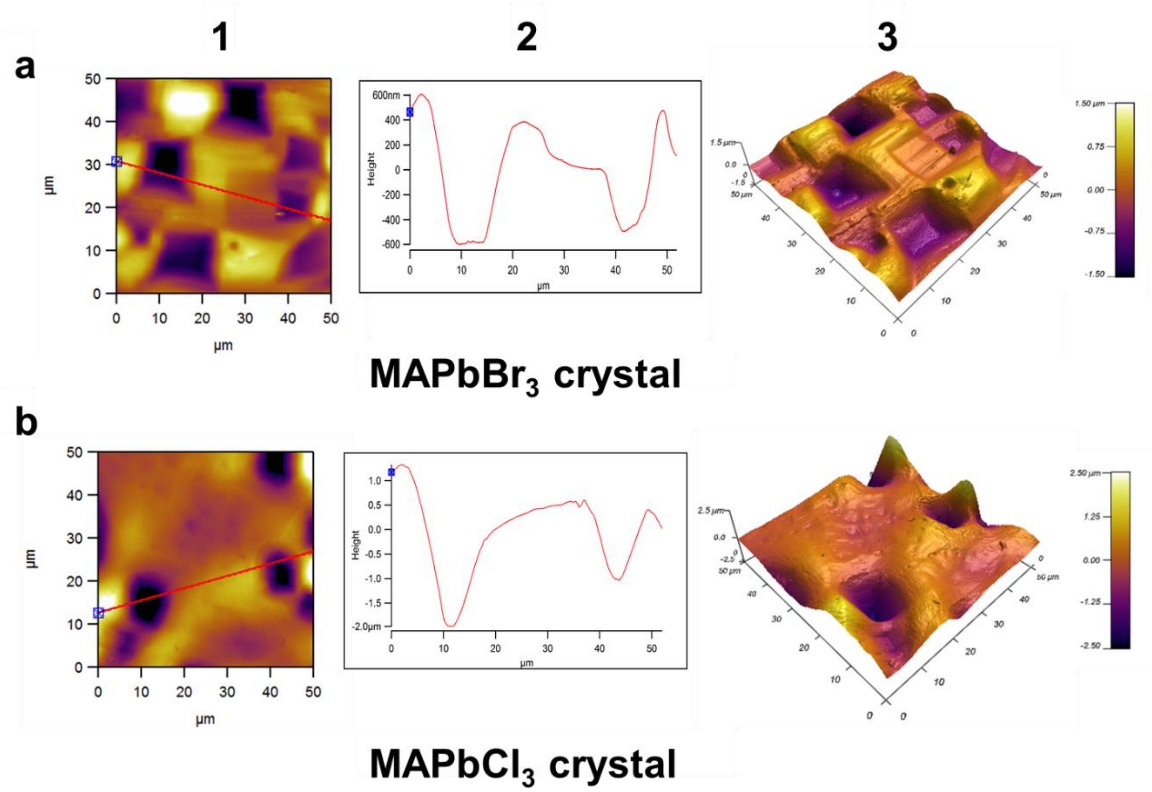

Figure 7.4 Surface topography and height profile of (a) $MAPbBr_3$ crystal, and (b) $MAPbCl_3$ crystal.

The cubic forming of crystals on surface can be explained by the growth process. The process of crystal growth includes two major steps, first step is nucleation and second step are crystal growth. In the nucleation step, the solute molecules start to gather into small cluster which acts as the initial for the next step. In the crystal growth step, the growth of the nuclei clusters is subsequent to achieve a critical cubic cluster size. Nucleation and growth continue to occur simultaneously resulting the cubic hole forming on the surface of the both $MAPbBr_3$ and $MAPbCl_3$ crystals.

7.7 Conductivity Behaviours

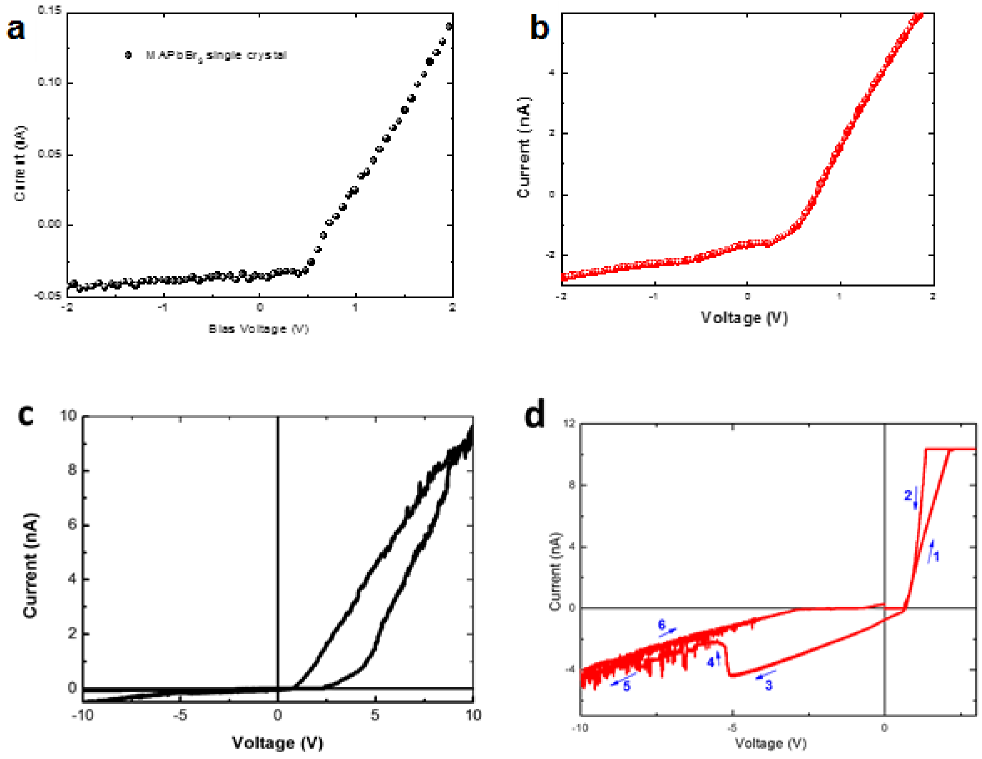

Figure 7.5 The average 10 I-V curves of (a) $MAPbBr_3$, and (b) $MAPbCl_3$ single crystals, and the average 3 I-V hysteresis response of (c) $MAPbCl_3$ single crystal, and (d) $MAPbBr_3$ single crystal. All I-V curves collected under dark condition

The current-voltage response of $MAPbBr_3$ crystal is shown in Figure 7.5a. The characteristic curves of $MAPbBr_3$ follows the typical Schottky contact feature. The current response at reverse bias tends to saturate at low values indicating its voltage-independence. The current-voltage response exhibits exponential behaviour with the positive applied voltage increase. At the positive bias of +2V, the current value was 0.14 nA. That result shows the agreement with the results of the Zhao group.[16] For the $MAPbCl_3$ crystal, the current-voltage response in Fig 7.5b also follows the Schottky behaviours at the positive bias voltage. However, the difference is observed at the negative bias voltage. The current increase with the increase of the negative bias value. At V = –2V, the current value was –2.14 nA.

7.8 Discussion

The current flowing in the reverse bias Schottky junction is given by:

$$I = SA^{**}T^2 exp\left(-\frac{q\phi_{bo}}{kT}\right)\exp\left(\frac{q\phi_{bi}}{kT}\right) \tag{7.1}$$

where A** is the effective Richardson constant, S is the area of the Schottky Barrier (SB) i.e. M–S contact area, q is the electronic charge and k is the Boltzmann constant; ϕ_{bo} is the ideal Schottky Barrier Height in the absence of an image force and ϕ_{bi} is the barrier height lowering due to the image force which indicates the decreasing Schottky Barrier Height.[22]

In our measurement, the perovskite single crystals (PSCs) were placed between the Pt-coated cantilever and contact with the holder by a layer of Silver paste (Fig 6a). The top and bottom contacts of the perovskite single crystals (PSC) are not symmetric.

We can consider the Pt/ PSC/Ag structure as a metal-semiconductor-metal (M–S–M) configuration. In this M–S–M configuration, two junctions are determined. The first junction is Ag/PSC which can act as a forward bias and the second junction Pt/PSC which can be a reverse bias depending on the applied voltage (Fig 7.6b).

At the bottom of the PSC, Ag has a work function of 4.6 eV that is larger than the electron affinity of PSC, so Schottky barrier forms (Fig 7.6c and d). At a small forward bias, only a small forward current is conducted, the current–voltage curves reveal exponential response according to the ideal diode behaviour as shown in Fig 7.5. At larger forward bias the current-voltage curve starts to be dominated by the ohmic resistance of the bulk crystals. The curve will exhibit a straight line instead of an exponential curve (see in Fig 7.7).

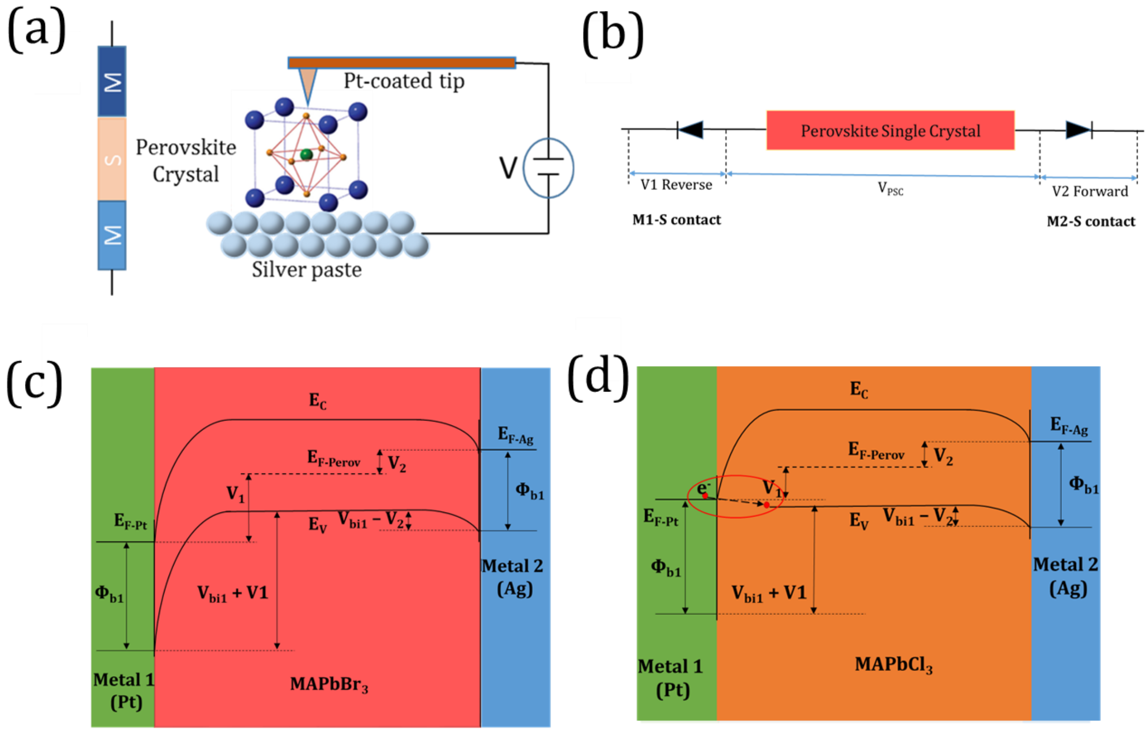

Figure 7.6 (a) Illustration of Pt/ PSC/Ag structure as M-S-M contact, the thickness of both perovskite sample is 300 μm, (b) Asymmetric diagram of the Schottky barrier height under reverse (V1) and forward (V2) biases at contacts 1 (Pt/PSC) and contacts 2 (Ag/PSC), respectively, and (c, d) Schematically energy band diagrams of the M–S–M contacts for $MAPbBr_3$ and $MAPbCl_3$ p-type semiconductors.

According to the thermionic emission theory, the thermal energy given to the carrier to overcome the work function of material resulting in the saturated current response at a reverse bias range of voltage as shown in Fig 7.6a.

For the $MAPbCl_3$ single crystals, the electron conductivity behavior at forward bias is like the $MAPbBr_3$ single crystals with the typical curve of Schottky contact feature. However, a current leakage was observed at reverse bias. It can be explained through the close position of Valence Band of $MAPbCl_3$ perovskite is about 5.8 eV, while the work function of Pt is about 5.7 eV. So that the Schottky barrier height is negative (Fig 7.6d).

Therefore, electrons can inject from Pt to valence band of $MAPbCl_3$ at the Pt/$MAPbCl_3$ contact under the reverse applied voltage. Majority carriers (holes) also pass across the Pt/$MAPbCl_3$ contact without any resistance, which results in a high leakage current. As a result, the increase of tunnel current through the energy barrier of Pt-Perovskite interface at reverse bias.

To demonstrate this tunnel effect, we measured the hysteresis of current response at room temperature of both of $MAPbBr_3$ and $MAPbCl_3$ as shown in Fig 7.6c, d. The current response of $MAPbBr_3$ crystal are following the typical Schottky theory both in the forward and reverse bias (Fig 7.6c). However, we can observe the peak-to-valley feature (arrow 3 to arrow 4 in Fig 7.6d) in $MAPbCl_3$ crystal which is similar typical heterostructure resonant tunnelling diodes.

To check the dependence between the crystal size and conductivity of the Pt/$MAPbCl_3$/Ag configuration, we prepared the micro $MAPbCl_3$ crystals for c-AFM testing. The schematic illustration of the crystal growth of micro $MAPbCl_3$ single crystals shown in Fig 7.7. Firstly, the FTO glass substrates were coated by a layer poly(3,4-ethylenedioxythiophene (PEDOT:PSS) polystyrene sulfonate) and lead acetate ($Pb(CH_3COO_2)_2$) respectively. Then, the whole chips were place into vials which contained MACl solution. After 20h at room temperature inside dry-box, we obtained the micro size $MAPbCl_3$ single crystals. Since PEDOT: PSS has a work function of about 4.7 eV which is close to the work function of Ag, the Pt/$MAPbCl_3$/PEDOT:PSS junctions are expected to behave similarly to the Pt/$MAPbCl_3$/Ag junctions in terms of conductivity.

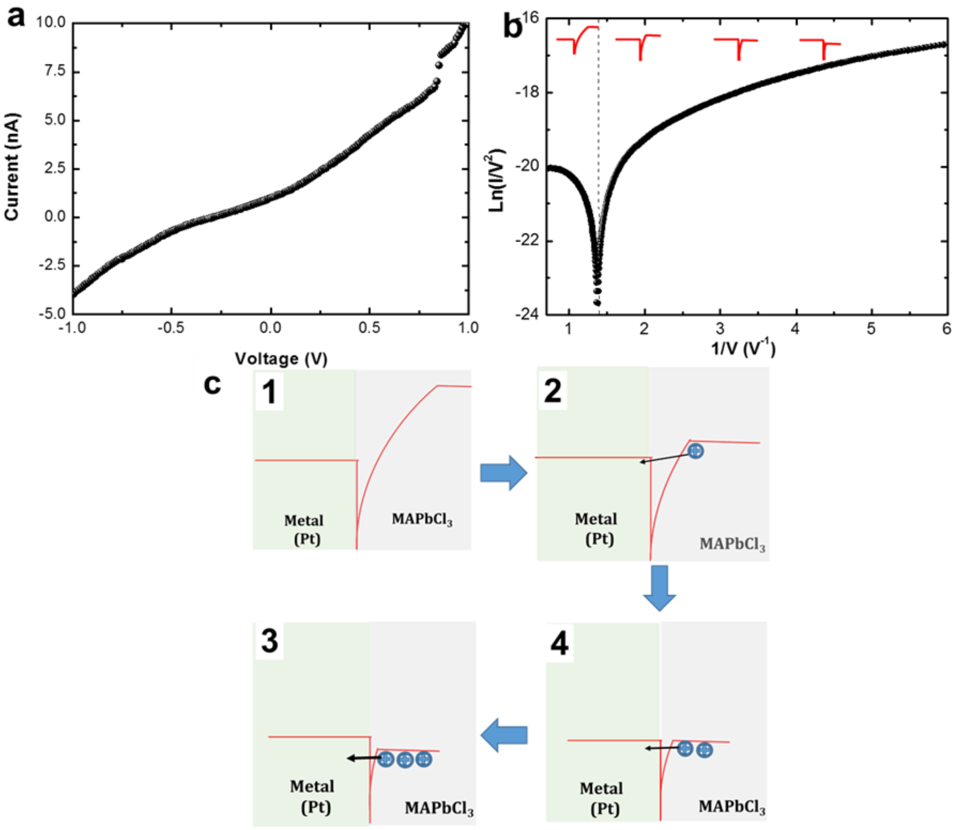

Figure 7.7 (a) The average of 10 I-V curves for $MAPbCl_3$ micro single crystals, and (b) Plots of Ln (I/V^2) against 1/V of a Pt/$MAPbCl_3$/Ag junctions, the dashed line indicates the voltage at which the tunneling barrier transitions occur. All I-V curves collected under dark condition. (c) Illustration diagram for voltage dropping effect on Vtrans.

The Fig 7.7c show the morphology of samples with micro cubic crystals on sample surface. The XRD pattern in Fig 7.7a indicated the high crystalline quality of the micro $MAPbCl_3$ crystals. The Fig 7.7b and Fig 7.7d shown the absorbance and topography of the samples, respectively. The current-voltage responses were collected at different positions corresponding to different micro single crystals.

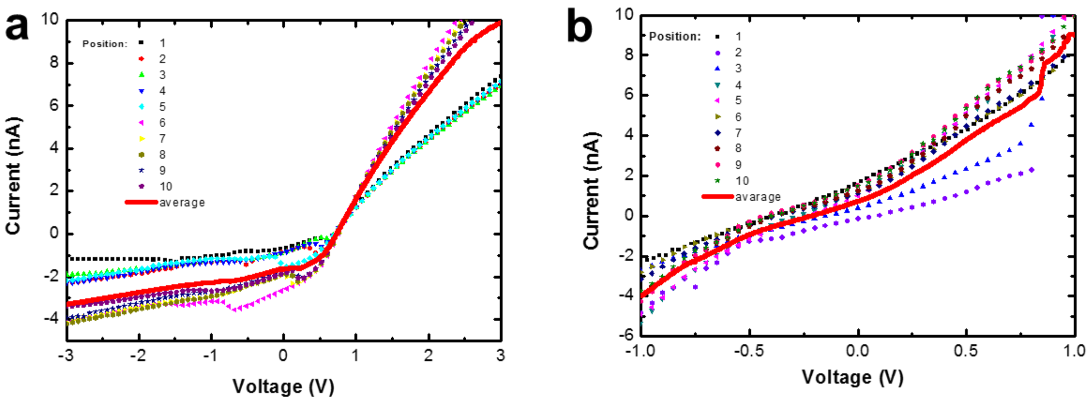

Figure 7.8 I-V curves of $MAPbCl_3$ single crystals after 10 measurement times under dark condition of (a) mm size crystals and (b) µm size crystals. The RED curve is the average value.

The Fig 8b shown the average 10 I-V curves of micro $MAPbCl_3$ single crystals with the growth process are described in Fig. 7.11. We observed the shape consistence in the I-V curve between the µm- and mm- $MAPbCl_3$ single crystals as expectation. The difference in current value is due to the different electric field applied through different crystal thickness. This result confirms that the conductivity behaviours of the $MAPbCl_3$ are independent to its crystal sizes.

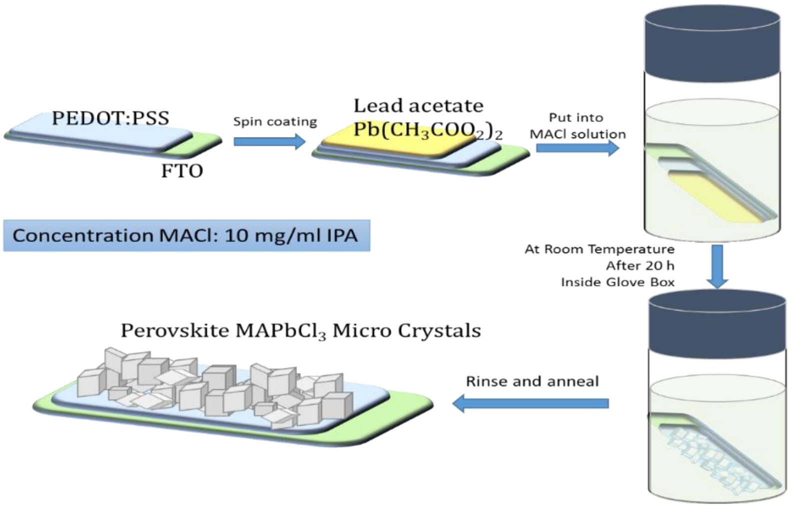

Figure 7.11 Schematic illustration of the crystal growth of Micro $MAPbCl_3$ single crystals

The structure, morphology, absorbance and topographic results of the micro $MAPbCl_3$ single crystals demonstrate that the crystals possess high-crystallite (Fig. 7.12). With the controllable size, the micro crystals should be a promising choice for micro electronic devices based on $MAPbCl_3$.

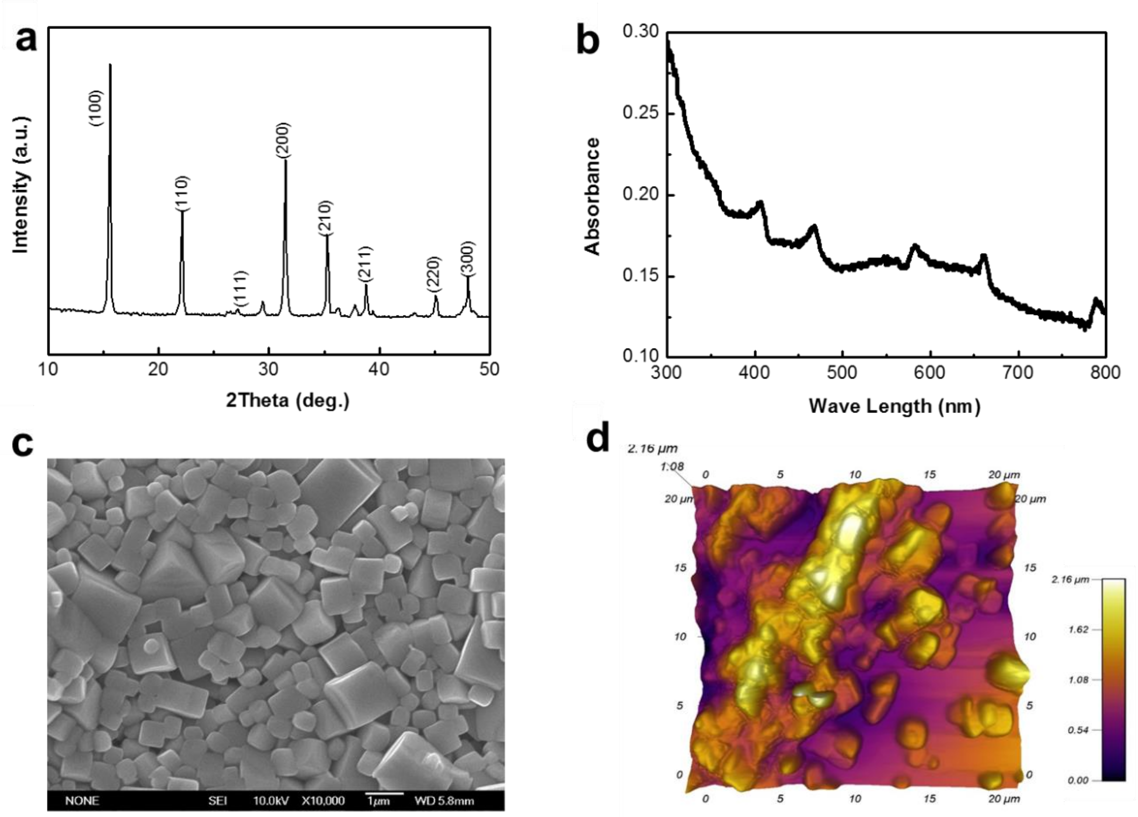

Figure 7.12 Characterizations of micro $MAPbCl_3$ single crystals: (a) XRD pattern, (b) Steady-state absorbance, (c) SEM Morphology image, and (d) Topographic AFM image.

For the Pt/$MAPbCl_3$ junctions, the tunnelling injection of electrons from the Pt tip into the MAPbCl3 single crystals is assumed to behave following the planar

(7.2)

tunneling theory. So that, the current density from the tunnelling model is expressed by:[23-25]

$$I = \left(\frac{eA}{4\pi^2 \hbar d^2}\right)\left\{\phi\left(-\frac{eV}{2}\right) exp\left[-\frac{2\sqrt{2m_e}}{\hbar}\alpha\sqrt{\phi - \frac{eV}{2}d}\right] - \left(\phi + \frac{eV}{2}\right) exp\left[-\frac{2\sqrt{2m_e}}{\hbar}\alpha\sqrt{\phi + \frac{eV}{2}d}\right]\right\},$$

where A is the junction area m_e is the electron effective mass, $\hbar$ is Planck's constant, d is the tunneling barrier width, ϕ is the tunneling barrier height, and α is a unitless parameter accounting for either a non-rectangular barrier or an effective mass, and e is the electronic charge. When the applied bias increase according to increase of Pt energy level that near to valence band of $MAPbCl_3$, the barrier transitions occur according to state shown from Fig 8c1 to Fig 8c2, and the current-voltage dependence can be described as follows:[23]

$$I \propto V^2 exp\left(-\frac{4d\sqrt{2m_e\phi^3}}{3\hbar eV}\right), \tag{7.3}$$

The Eq (3) can be rewritten by:

$$ln\left(\frac{I}{V^2}\right) \propto -\frac{4d\sqrt{2m_e\phi^3}}{3\hbar e}\left(\frac{1}{V}\right), \tag{7.4}$$

According to Eq (4), the plot of Ln (I/V^2) against 1/V will exhibit a logarithmic growth in the low bias voltage. When energy level of Pt tip is close to the valence band of $MAPbCl_3$, the mechanisms compete, resulting in a transition from logarithmic growth to linear decay.

Fig 8b shows the plots of Ln (I/V^2) against 1/V of a Pt/$MAPbCl_3$ junctions. A linear decay was observed in the plot. We can determine that the position at which the tunnelling injection occurred at 1/V=1.4 V^{-1} corresponds the transition voltage is 0.71 V.

7.9 Summary

In summary, we report a highly quality $MAPbBr_3$ and $MAPbCl_3$ single crystals using electric oven inverse temperature reactive crystallization (ITC) process at 70^oC. The topography of $MAPbBr_3$ and $MAPbCl_3$ single crystals show the cubic holes corresponding to the growth process. Moreover, the conducting AFM were used to measure the current-voltage response of the both crystals. Interestingly, by using the Schottky contact theory, we can explain the tunnelling effect in conductivity behaviour of $MAPbCl_3$ single crystals.

References

1 Yang, W. S. *et al.* High-performance photovoltaic perovskite layers fabricated through intramolecular exchange. *Science* **348**, 1234-1237, doi:10.1126/science.aaa9272 (2015).

2 Bi, D. *et al.* Efficient luminescent solar cells based on tailored mixed-cation perovskites. *Science Advances* **2**, doi:10.1126/sciadv.1501170 (2016).

3 Xing, G. *et al.* Low-temperature solution-processed wavelength-tunable perovskites for lasing. *Nature materials* **13**, 476-480, doi:10.1038/nmat3911

http://www.nature.com/nmat/journal/v13/n5/abs/nmat3911.html#supplementary-information (2014).

4 Xing, J. *et al.* Vapor Phase Synthesis of Organometal Halide Perovskite Nanowires for Tunable Room-Temperature Nanolasers. *Nano letters* **15**, 4571-4577, doi:10.1021/acs.nanolett.5b01166 (2015).

5 Fu, Y. *et al.* Nanowire Lasers of Formamidinium Lead Halide Perovskites and Their Stabilized Alloys with Improved Stability. *Nano letters* **16**, 1000-1008, doi:10.1021/acs.nanolett.5b04053 (2016).

6 Luo, J. *et al.* Water photolysis at 12.3% efficiency via perovskite photovoltaics and Earth-abundant catalysts. *Science* **345**, 1593-1596, doi:10.1126/science.1258307 (2014).

7 Gurudayal *et al.* Improving the Efficiency of Hematite Nanorods for Photoelectrochemical Water Splitting by Doping with Manganese. *ACS applied materials & interfaces* **6**, 5852-5859, doi:10.1021/am500643y (2014).

8 Chen, Y.-S., Manser, J. S. & Kamat, P. V. All Solution-Processed Lead Halide Perovskite-BiVO4 Tandem Assembly for Photolytic Solar Fuels Production. *Journal of the American Chemical Society* **137**, 974-981, doi:10.1021/ja511739y (2015).

9 Fang, Y., Dong, Q., Shao, Y., Yuan, Y. & Huang, J. Highly narrowband perovskite single-crystal photodetectors enabled by surface-charge recombination. *Nat Photon* **9**, 679-686, doi:10.1038/nphoton.2015.156

http://www.nature.com/nphoton/journal/v9/n10/abs/nphoton.2015.156.html#supplementary-information (2015).

10 Dou, L. *et al.* Solution-processed hybrid perovskite photodetectors with high detectivity. *Nature communications* **5**, doi:10.1038/ncomms6404 (2014).

11 Lu, H. *et al.* A Self-Powered and Stable All-Perovskite Photodetector–Solar Cell Nanosystem. *Adv Funct Mater* **26**, 1296-1302, doi:10.1002/adfm.201504477 (2016).

12 Tiep, N. H., Ku, Z. & Fan, H. J. Recent Advances in Improving the Stability of Perovskite Solar Cells. *Adv Energy Mater* **6**, n/a-n/a, doi:10.1002/aenm.201501420 (2016).

13 Mitzi, D. B. Solution-processed inorganic semiconductors. *Journal of Materials Chemistry* **14**, 2355-2365, doi:10.1039/B403482A (2004).

14 Dong, Q. *et al.* Electron-hole diffusion lengths> 175 µm in solution-grown CH3NH3PbI3 single crystals. *Science* **347**, 967-970 (2015).

15 Shi, D. *et al.* Low trap-state density and long carrier diffusion in organolead trihalide perovskite single crystals. *Science* **347**, 519-522, doi:10.1126/science.aaa2725 (2015).

16 Zhao, P. *et al.* Large-Size CH3NH3PbBr3 Single Crystal: Growth and In Situ Characterization of the Photophysics Properties. *The Journal of Physical Chemistry Letters* **6**, 2622-2628, doi:10.1021/acs.jpclett.5b01017 (2015).

17 Maculan, G. *et al.* CH3NH3PbCl3 Single Crystals: Inverse Temperature Crystallization and Visible-Blind UV-Photodetector. *The Journal of Physical Chemistry Letters* **6**, 3781-3786 (2015).

18 Saidaminov, M. I. *et al.* High-quality bulk hybrid perovskite single crystals within minutes by inverse temperature crystallization. *Nature communications* **6**, doi:10.1038/ncomms8586 (2015).

19 Saidaminov, M. I., Abdelhady, A. L., Maculan, G. & Bakr, O. M. Retrograde solubility of formamidinium and methylammonium lead halide perovskites enabling rapid single crystal growth. *Chemical communications*, doi:10.1039/C5CC06916E (2015).

20 Liu, Y. *et al.* Two-Inch-Sized Perovskite CH3NH3PbX3 (X = Cl, Br, I) Crystals: Growth and Characterization. *Advanced materials* **27**, 5176-5183, doi:10.1002/adma.201502597 (2015).

21 Baikie, T. *et al.* A combined single crystal neutron/X-ray diffraction and solid-state nuclear magnetic resonance study of the hybrid perovskites CH3NH3PbX3 (X = I, Br and Cl). *J Mater Chem A* **3**, 9298-9307, doi:10.1039/C5TA01125F (2015).

22 Nandy, S. *et al.* Current transport mechanism at metal-semiconductor nanoscale interfaces based on ultrahigh density arrays of p-type NiO nano-pillars. *Nanoscale* **5**, 11699-11709, doi:10.1039/C3NR03803C (2013).

23 Beebe, J. M., Kim, B., Gadzuk, J. W., Daniel Frisbie, C. & Kushmerick, J. G. Transition from Direct Tunneling to Field Emission in Metal-Molecule-Metal Junctions. *Physical review letters* **97**, 026801 (2006).

24 Simmons, J. G. Generalized Formula for the Electric Tunnel Effect between Similar Electrodes Separated by a Thin Insulating Film. *Journal of Applied Physics* **34**, 1793-1803, doi:doi:http://dx.doi.org/10.1063/1.1702682 (1963).

25 Wang, W. *et al.* Electrical Characterization of Metal—Molecule—Silicon Junctions. *Annals of the New York Academy of Sciences* **1006**, 36-47, doi:10.1196/annals.1292.002 (2003).

Chapter X

Conclusion

This chapter describes the explorative work on hybrid halide perovskite single crystal, including the novel solvent method to facile grow the high-quality crystal at low temperature, and their phase transition properties. The recommendations for further studies have been also given.

In this thesis, we have reported a facile solution method to grow the stable 2D layered $(C_6H_5C_2H_4NH_3)_2PbCl_4$ (PEPC) perovskite single crystals in Chapter 3. The ferroelectrics of the single crystal were confirmed by PFM, box-in-box local switching testing, and ferroelectric testing. The PEPC crystal can generate a remnant polarization of about 0.85 μC cm^{-2}, a coercive field of about 1.5 kV/cm and an effective piezoelectric coefficient of 90 pm V^{-1}. The crystal also exhibits the white light emission behaviour. Our results provide a new way to functionalize a new piezoelectric/ferroelectrics and photovoltaics based on 2D layered hybrid perovskite single crystals.

Continuing the success of synthesizing the PEPC crystals, the lead-free 2D layered $(C_6H_5C_2H_4NH_3)_2CuCl_4$ (PECC) single crystals using DI water as the solvent have been introduced in Chapter 5. The XRD data and SEM image demonstrate the high crystal quality of the as-prepared single crystal and their layered structure. The DSC and TGA data indicate the thermal stability of about 200°C and their phase transition behaviour of the crystals. The PFM results and box-in-box switching test show the domain structure in the crystal and thin film, and the ability to change the polarization orientation of the thin film sample. Particularly, a piezo device based on the crystal could generate a 0.05 V output. These results have promised new opportunities to employ the lead-free $(C_6H_5C_2H_4NH_3)_2CuCl_4$ single crystals in piezoelectric.

Beside the 2D perovskite crystals, the crystal growth of 3D ones has been reported. Chapter 6 are focusing on a facile, novel method in synthesize the centimetric $CH_3NH_3PbI_3$ perovskite single crystals at low temperature (70°C) using mixtures solvent of ACN/GBL. The SEM and XRD results demonstrate the high quality of the tetragonal structure $CH_3NH_3PbI_3$ crystals with a better thermal stability comparing to the thin films, resulting from the TGA data. The time-dependent PL signals reveal the slow carrier dynamic, which confirming the lifetime of carriers propagating deeper in the crystal. Our work should provide new approaches to employ the centimetric $CH_3NH_3PbI_3$ single crystals for both scientific study and technological applications in PV solar cells.

The highly quality $MAPbBr_3$ and $MAPbCl_3$ single crystals using electric oven inverse temperature reactive crystallization (ITC) process at 70°C have been investigated in Chapter 7. The topography of $MAPbBr_3$ and $MAPbCl_3$ single crystals show the cubic holes corresponding to the growth process. Moreover, the conducting AFM were used to measure the current-voltage response of the both crystals. Interestingly, by using the Schottky contact theory, we can explain the tunnelling effect in conductivity behaviour of $MAPbCl_3$ single crystals.

Overall, the obtained results, analysis and discussion are believed to fulfil the research objectives. Nevertheless, the results still open for improvements as well as potential applications, as suggestions below:

Further property of the $(C_6H_5C_2H_4NH_3)_2PbCl_4$ (PEPC) perovskite single crystals including magnetic and photonic properties. It has been shown in Chapter 3 that the PEPC is a white light emission material. However, the work just stopped in optical and photonic characterizations. It is worthy undertaking the PEPC single crystal in an application. The crystal-based devices have been promised to perform better than the thin film based one due to their outstanding perspectives in comparison with the thin film. Furthermore, the magnetic characterizations of the as-prepared single crystals are also recommended to be studied. The application of the perovskite solar cell using the centimeter scale $CH_3NH_3PbI_3$ has been a potential approach, in spite of the difficulty in technique for making the bulk solar cell devices.

APPENDIX

Table A1: The structure parameters for the $(C_6H_5C_2H_4)_2PbCl_4$ single crystal simulation.

No.	Atom	Symbol	x	y	z	Occ.	U	Site	Sym.
1	Pb	Pb1	0	0	0	1	0.048	2a	2/m
2	Cl	Cl2	0.08551	0	0.0551	1	0.062	4i	m
3	Cl	Cl3	0	1	-0.5	1	0.042	2c	2/m
4	Cl	Cl4	0.00023	-0.5	-1	1	0.053	4i	m
5	N	N1	-0.0723	-0.5	-0.3784	0.5	0.047	4i	m
6	H	H1A	-0.0479	-0.4432	-0.3885	0.25	0.07	8j	1
7	H	H1B	-0.071	-0.6482	-0.3217	0.25	0.07	8j	1
8	H	H1C	-0.0854	-0.4086	-0.2803	0.25	0.07	8j	1
9	N	N1A	-0.0714	-0.3153	-0.5261	0.25	0.047	8j	1
10	H	H1A1	-0.0457	-0.3477	-0.5003	0.25	0.071	8j	1
11	H	H1A2	-0.0805	-0.2532	-0.3936	0.25	0.071	8j	1
12	H	H1A3	-0.0748	-0.2111	-0.6461	0.25	0.071	8j	1
13	C	C1	-0.0896	-0.5	-0.5791	1	0.125	4i	m
14	H	H1AA	-0.0729	-0.5925	-0.6784	0.5	0.15	8j	1
15	H	H1BB	-0.0883	-0.3369	-0.6342	0.5	0.15	8j	1
16	C	C2	-0.1311	-0.5812	-0.6406	0.5	0.061	8j	1

17	H	H2A	-0.1341	-0.7434	-0.5846	0.5	0.074	8j	1
18	H	H2B	-0.1362	-0.5804	-0.8137	0.5	0.074	8j	1
19	C	C3	-0.1607	-0.4227	-0.5279	0.5	0.051	8j	1
20	C	C4	-0.1745	-0.2185	-0.648	0.5	0.062	8j	1
21	H	H4	-0.1622	-0.1855	-0.8028	0.5	0.074	8j	1
22	C	C5	-0.2018	-0.0712	-0.5465	0.5	0.078	8j	1
23	H	H5	-0.2113	0.0631	-0.6301	0.5	0.094	8j	1
24	C	C6	-0.2146	-0.1235	-0.3234	0.5	0.083	8j	1
25	H	H6	-0.2291	0	-0.2243	1	0.1	4i	m
26	C	C7	-0.2006	-0.324	-0.2058	0.5	0.081	8j	1
27	H	H7	-0.208	-0.3717	-0.0408	0.5	0.098	8j	1
28	C	C8	-0.1736	-0.5	-0.3046	1	0.071	4i	m
29	H	H8	-0.166	-0.6425	-0.2299	0.5	0.085	8j	1

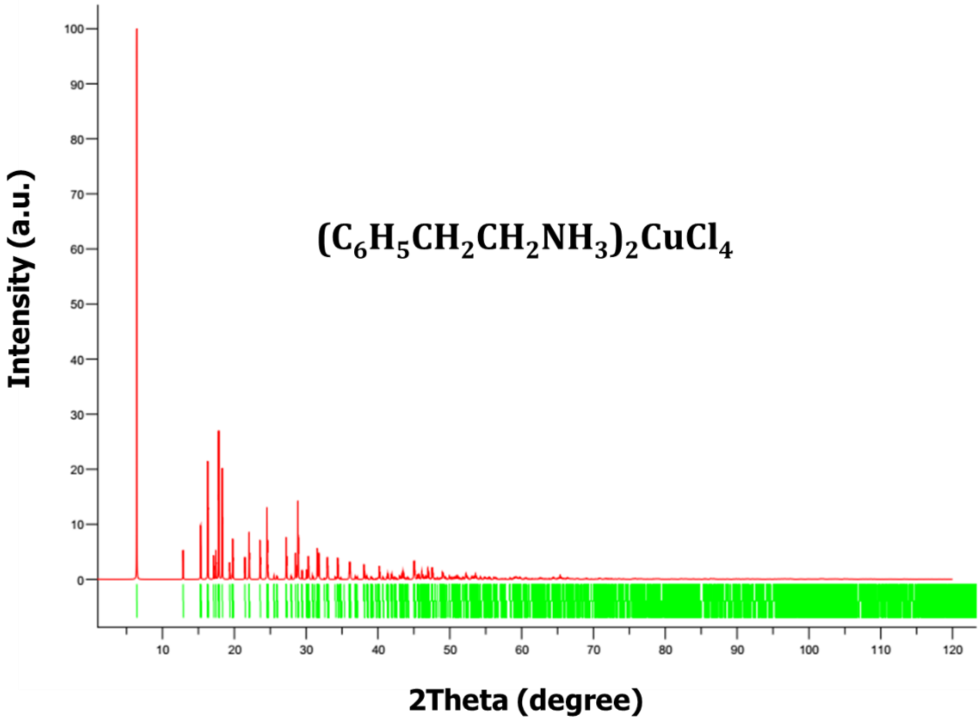

Figure A1 The Calculated Data for Powder XRD of PECC perovskite showing the agreement with the as-prepared lead-free 2D layered PECC single crystal in Chapter 5.